IN SEARCH OF CATALYSTS…

Umar Ibrahim Gaya
B.Sc. (Hons) (Unimaid), M.Sc. (BUK), Ph.D. Catalysis (UPM), MCSN, MACS
Professor of Physical Chemistry
Department of Pure and Industrial Chemistry
Faculty of Physical Sciences
Bayero University, Kano

BAYERO UNIVERSITY, KANO,
PROFESSORIAL INAUGURAL LECTURE

NO. 50

Date: 4TH NOVEMBER, 2021

BAYERO UNIVERSITY PRESS

Published 2021 by:
Bayero University Press,
Main Library Building,
Bayero University Kano,
New Site, Gwarzo Road,
P.M.B. 3011.
Kano.

Website: *www.buk.edu.ng*
E-mail: *info.bukpress@buk.edu.ng*

ISBN: 978-978-59034-0-9

PRINTED BY BAYERO UNIVERSITY PRESS KANO, NIGERIA

UMAR IBRAHIM GAYA
B.Sc. (Unimaid), M.Sc. (BUK), PhD (UPM), MCSN, MACS
Professor of Physical Chemistry
Department of Pure and Industrial Chemistry
Faculty of Physical Sciences
Bayero University, Kano

SUMMARY OF PRESENTER'S BIODATA

Umar Ibrahim Gaya was born in Gwale LGA. He attended Kofar Naisa Primary School between 1977 and 1983, and Government Secondary School Sabuwar Kofa from 1983 to 1986. He completed his secondary school education at Rumfa College, Kano in 1989, and IJMB A-Level study in 1992 and later graduated with B.Sc. (Hons) in Chemistry from University of Maiduguri in 1996. He had his national service in the Petrochemical Laboratory, Kaduna Refinery and Petroleum Company, KRPC (1997 to 1998) as the Quality Controller with Camom Engineering and Services Company for the Rehabilitation of KRPC Lubes Plant and a casual staff at the Refinery Laboratory of the KRPC/NNPC (1998 to 1999). In 2000, he joined Bayero University as Graduate Assistant. Later, between 2003 and 2004, he was appointed by the Federal Government of Nigeria to serve Pakalinding Upper Basic School in The Gambian Department of State for Education and Department of State for Foreign Affairs as Technical Aid Corps Volunteer. In 2004, he bagged his M.Sc. In Analytical Chemistry from Bayero University, Kano. He then pursued PhD in Catalysis at Universiti Putra Malaysia from 2007 to 2009. He was a post-doctoral research fellow in the Department of Chemistry, Universiti Putra Malaysia in 2011 and in the Department of Petroleum and Chemical Engineering, Sultan Qaboos University from 2011 to 2012.

Umar has the experience of teaching more than 50 chemistry courses at pre-degree, diploma, B.Sc., PGD, M.Sc. and PhD levels in Bayero University, and other tertiary institutions which include Kano University of Science and Technology, Sule Lamido University, Bauchi State University and Saadatu Rimi College of Education. He has completed the supervision of 2 PhD (Physical Chemistry), 19 M.Sc. (Physical Chemistry), 4 M.Sc. (Analytical Chemistry), 79 undergraduate, 22 diploma students. He is currently supervising 2 doctoral students in Physical Chemistry. He has also graduated many postgraduate diploma students. He has internally examined a good number of undergraduate, M.Sc. and PhD degrees. He was external examiner for coursework, M.Sc. and PhD at Ahmadu Bello University, Federal University of Technology, Minna and for M.Sc. at Kano University of Science and Technology.

Umar's research interests cover a range of topics in the field and frontiers of Physical Chemistry, with specific interest in Catalysis. He has published many articles in high impact journals one of which was the most downloaded and among

the Top 25 *ScienceDirect*. He has been the most cited author from Bayero University for over a decade as evidenced by Scopus, Journal Citation Report (JCR), Researchgate and Google Scholar. He has presented many papers locally, and at prestigious conferences in the UK, South Korea, Indonesia, Malaysia and Hong Kong. In 2017, his paper on Methanolysis was selected for presentation by the International Union of Pure and Applied Chemists (IUPAC) World Congress at the Golden Hall of the World Trade Centre, Sao Paulo, after the plenary of the 2017 Nobel Laureate Sir Fraser Stoddart. He was organiser or member of organizing committees of training, conferences and seminars. He has worked as student or collaborator under many grants including the Malaysia Fundamental Research Grant Scheme (FRGS), Malaysia University Grant Scheme, The Sultan Qaboos University TRC grant. He has presented papers at seminars organised by Universiti Putra Malaysia, Bauchi State University, and different Faculties, College of Health Sciences, Centre for Dryland Agriculture, Department of Business Administration and Entrepreneurship of Bayero University, Kano.

Umar is a member of Chemical Society of Nigeria (CSN), CSN Stakeholders' Forum, the American Chemical Society-Catalysis Division (ACS-CATL) and is a reviewer of many Scopus-indexed journals. In Bayero University, he was a key member of more than 60 departmental, community, faculty or university committees including many strategic committees/boards in Bayero University such as the Tetfund Utilisation Committee, Appointments and Promotions Committee, Sponsorship Sub-committee, Convocation Committee, Inaugural Lecture Committee, Board of the School of Postgraduate School (SPS), Direct Teaching and Labour Committee (DTLC), Board of Bayero University Academic Staff Cooperative (BUKASCO), Board of the Bayero University Press and Board of the Directorate of Research Innovation and Partnership (DRIP). He was the Departmental Postgraduate Coordinator, Head of Physical Chemistry Unit, Faculty Examination Officer and SIWES Coordinator. As the former Chairman of the University Journals Coordinating Committee, he drafted the first Journal Publishing Policy of Bayero University. As Deputy Director I (and Acting Director) of DRIP from 2016 to 2018, he participated in the drafting of the first Research Policy and Intellectual Property Policy of Bayero University.

Umar has received severally commendations in the University. In February 2014, he was mentioned at the floor of the Senate for reputable publications. In 2015 and 2016, he appeared in Webometric ranking of scientists sponsored by ACUMEN,

European Commission and Spanish Research Council for which he received a commendation letter from Bayero University. He was among the two national speakers at the 3rd Biennial Conference of the Transplant Association of Nigeria (TAN) & 1st International Conference of the College of Health Sciences. In 2010, he was honoured with an award by the Nigerian Students' Community in Malaysia (NISCOM) at the occasion commemorating the 50th Anniversary of Nigeria. He was gratified with appreciation awards from Universiti Putra Malaysia for serving different students' associations. He was also granted the Graduate Research Fellowship of that university.

Umar has been recognised by the local community and has been a member or patron of numerous local associations. He has just been promoted to the title of Ciroman Gaya of the Gaya Emirate, Kano. In 2005, he was awarded Shahadah Taqdir award (for being Hafiẓ and contributor to the Madrasah) by the Madarasatu Umar Bin Khattab Lit-tahfizul Qur'an, Gwale L.G.A, Kano. He is the coordinator of the Federal Government Special Works (FG SPW). He speaks English, Arabic, Hausa, Malay and Fulfulde.

In Search of Catalysts…

BASIC CONCEPTS

In this lecture, I wish to make the audience appreciate the role of chemistry as a central science, from the standpoint of catalysis. The branches of chemistry, physical chemistry, narrowing down to the types of catalysis and areas with which it cross-pollinates will be briefly introduced. Lastly, I will present some societal and industrial significance of catalysis based on my personal experiences.

Chemistry is a branch of science that deals with the composition, properties and structure of matter, and the changes it undergoes. Matter is primarily anything that has mass and volume such as a solid, liquid, gas, or plasma (ionised gas particles). It is composed of an element, or combination of elements. The Periodic Table carries the names of all the known elements and their symbols (e.g. H for hydrogen). The basic unit of the element exhibiting its properties is referred to as atom. It contains sub-atomic particles known as the neutrons, protons and electrons. Any particle consisting of two or more atoms of one or more elements held together by a chemical bond is called molecule. For example, a molecule of hydrogen consists of two hydrogen atoms (written as H_2). Air contains oxygen molecule, O_2 (20.9 %), nitrogen molecule, N_2 (78.1 %), carbon dioxide CO_2, (0.03 %), noble gases (1.0 %) and variable amount of water.

Traditionally, chemistry is widely said to have four major branches: analytical, inorganic, organic, physical chemistry. Biochemistry is often included as the fifth branch. Physical chemistry deals with the application of the principles of physics to chemical systems. Chemical kinetics is a physical chemistry discipline that deals with rates and mechanisms of chemical reactions while chemical thermodynamics is concerned with the inter-relations of various forms of energy. A third branch of physical chemistry called quantum chemistry, employs rules that apply to microscopic entities (such as electrons) to explain intractable, fundamental chemical problems. The sub-disciplines of physical chemistry include catalysis, photochemistry, electrochemistry and surface chemistry. Over the decades, the concentration of findings has led to the emergence of combined sub-disciplines such as biophysical chemistry and physical organic chemistry.

Catalyst

At the elementary level, the Ostwald's 1895 definition still holds true, which says "a catalyst accelerates a chemical reaction without affecting the position of the equilibrium." This definition, in quantitative sense, appears to be a kinetic phenomenon. A salient feature of a catalytic process is that chemical reaction is facilitated by switching the reaction pathway (Rothenberg, 2008). A catalyst may be heterogeneous or homogeneous depending upon whether it is in the same phase with the reactant, respectively. Certain features of homogeneous and heterogeneous catalysts are compared in Table 1. Biocatalyst, is now a third type of catalyst, in the form of one or more enzymes, or cells, capable of aiding the synthesis of chemical compounds for industrial purposes. For example, a mutated Eschericia coli can convert D-glucose to a precursor of adipic acid (a monomer for making nylon).

Catalysis is a unifying field for science disciplines. It crosses some many areas of physical chemistry such as chemical kinetics, photochemistry, materials chemistry, quantum chemistry, nanochemistry, surface chemistry and electrochemistry. It also cross-pollinates with inorganic, organic and biochemistry.

Table 1: *Comparison between homogeneous and heterogeneous catalyst* (Hagen, 2015).

S/No.	Homogeneous catalyst	Heterogeneous catalyst
1	Catalyst and reactant are in the same phase	There is phase boundary between the catalyst and reactants
2	Every atom can be catalytically active	Only the surface atoms are active
3	Relatively higher activity per unit mass of metal	Relatively lower activity per unit mass of metal
4	Mechanism is well understood	Poorly understood mechanism
5	Reactions are kinetically controlled because material transport occurs readily	Reactions may be limited by mass transfer
6	Catalyst stable below 200 °C	Catalysts stable well above 200 °C
7	Separation of catalyst often	Easy recovery of catalyst

	difficult	
8	High catalyst loss	Low loss of catalyst
9	Limited applicability	Wider applicability
10	Highly selective	Less selective

Owing to the foregoing developments, catalysis may be classified severally based on the following:

1) *Type of reaction involved e.g. heavy oil upgrading catalysts. Redox catalysts are used in hydrogenation, halogenation, and oxidation. Similarly, hydrocracking catalysts are used in Fluid Catalytic Cracking (FCC)*
2) *Chemical nature of the catalysts e.g. acid-base catalysts used in hydaration, and isomerisation reactions.*
3) *Size e.g. nanoscopic/nano-sized, mesoscopic catalysts are terms used for catalysts of different size regimes.*
4) *Number of functions performed at once e.g. bifunctional catalysts and polyfunctional catalysts.*
5) *Number of its components exhibited by the catalyst e.g. multicomponent catalyst, single component catalyst.*
6) *Preparation method e.g. doped-catalyst, bulk catalyst, supported catalyst.*

Because of their compatibility with severe reaction conditions and several other desirable attributes, heterogeneous catalysts are industrially the most common. The active catalytic part is usually a metal or metal oxide, assisted by a promoter or support. In a special case known as photocatalysis, the catalyst (such as TiO_2 semiconductor), or coexisting molecule is excited by light of sufficient energy to produce redox species which can be exploited in many technological applications. For the purpose of this lecture we are concerned with heterogeneous or semiconductor photocatalysis, in which an electron (e_{CB}^-) is excited from the occupied valence band of the semiconductor to the empty conduction band, leaving behind a hole (h^+_{VB}) in the valence band (Eq. 1). Basically, different semiconductor photocatalysts have different band gaps as well as band gap energies.

$$SC \xrightarrow{h\nu \geq E_g} SC^*(h^+_{VB} + e_{CB}^-) \qquad (1)$$

Once recombination of these pair of charged carriers is minimised, they can be harvested for either photocatalytic reduction or oxidation, and applications such as the Gratzel's solar cell (Jayaweera et al., 2008). The oxidation of organic compounds to benign minerals such as carbon dioxide (CO_2) and water (H_2O) by this technology is currently generating huge interest. We have provided an equation to account for photo-oxidative mineralisation of all substituted organic compounds (Eq. 2) (Gaya, 2015). In our previous reports, we have provided a compilation of a high number of hazardous materials mineralised using photocatalysis (Gaya and Halim, 2008; Gaya, 2015).

$$C_aH_bX_mY_n + (2m + s + \frac{b-m}{2})O_2 \rightarrow aCO_2 + (\frac{b-m}{2})H_2O + mH^+ + mX^- + mYO_s^{v-} \qquad (2)$$

Where X stands for each of the heteroatoms as Cl, Br, F, and Y represents I, –CN, P, S and N. *a*, *b*, *m* and *n* are the number of C, H, X and Y in the molecule. YO_s^{v-} represents any radical such as OCN^-, PO_4^{3-}, SO_4^{2-}, NO_3^- having charge *v* and *s* represents the number of O atoms in the radical.

Semiconductor photocatalysis was brought to limelight by Fujishima and Honda way back 1972, as they split water (H_2O) to its components, in an electrolytic cell consisting of rutile TiO_2 photoanode and platinum (Pt) cathode. The author has witnessed the presentation of features of the pioneer cell by Fujishima himself in 2007. The striking story of this cell is that it has inspired a high number of technological developments such as sensors, decontamination, photovoltaic cells, shielding or reducing communication interference and electromagnetic radiation, and disinfection (Nabiyouni et al., 2018; Bagheri et al., 2019; Ahmadian-Fard-Fini et al., 2020).

Significance of Catalysts

Chemical reaction proceeds via bonding of atoms and/or breaking of the bond between atoms. However, a high number of industrial chemical transformations are known to not produce optimum yield or proceed as fast as required on their own accord, making catalysts indispensable. Catalysis, a sub-discipline of chemical kinetics, is concerned with the acceleration of the rate of chemical reactions. It has been widely accepted that 85 to 90% of manufactured products currently involve the use of catalyst, at least in one step, with catalyst contribution to global gross

domestic product (GDP) standing at 30 to 40% (Fletcher, 2021). In actual fact, the societal and industrial significance of catalysis cannot be overstressed.

Synthesis of Fine and Specialty Chemicals

Catalysis provides an array of cleaner methods (such as hydrogenation, oxidation, isomerization etc.) for synthesis of fine organic chemicals from biomass-derived feedstocks (such as oils and fatty acids) or synthetic sources. Some products of homogeneous catalytic reactions include the following (Bhaduri and Mukesh, 2000):

a) Ibuprofen **(1)**, an analgesic, is a product of catalytic carbonylation.
b) Menthol-L **(2)**, a flavouring agent, is a product of asymmetric isomerisation.
c) Naproxen **(3)**, an anti-inflammatory agent, is a product of asymmetric hydroformylation, hydrogenation or hydrocyanation.

Way back 2008, at a short course on catalysis at Singapore, the Nobel Laureate, Prof. Emeritus Akira Suzuki described to us his works on how, in presence of homogeneous palladium catalysts, carbon (C) from organoboron and haloborane can be bound together to form new chemical compounds (consisting of C-C bonds).

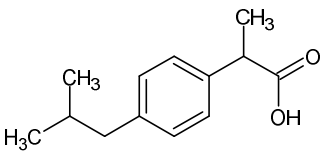

(1)

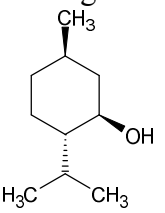

(2)

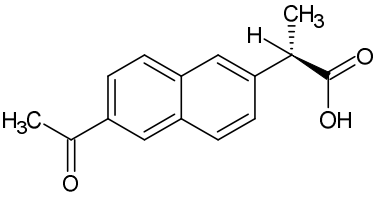

(3)

Energy Applications

At present, fuel cell catalysis is a zero-emission technology that has attracted significant attention. The hydrogen fuel cell electric vehicle (FECV) all started in 1950s with the work of an electrochemist, Professor Wolf Vielstich, the father of modern zero emission fuel cells. Practically, the fuel cell technology produces

energy from oxidation and reduction half reactions that occur in presence of platinum (Pt) catalyst to produce hydrogen ion (H^+) and water (H_2O) as shown by Eq. (3) and (4).

$$H_2 \xrightarrow{Pt} 2H^+ + 2e^- \quad \text{(Anodic reaction)} \tag{3}$$

$$2H^+ + 2e^- + \frac{1}{2}O_2 \xrightarrow{Pt} H_2O \text{ (Cathodic reaction)} \tag{4}$$

In 1998, there was intensive research with a view to replacing the traditional internal combustion engine. In 2012, despite previous commitments, the US and German governments were engulfed by feasibility fears for a H_2/O_2 fuel cell, making them to shift to all-electric, lithium-ion batteries, leaving the Asian car makers in the thirst for this fuel cell technology (The Korea Herald, 2018). In March 2018, Hyundai had a successful début of the Nexo FECV, and a year later, I had a touch of it at Hyundai, Goyang City, South Korea.

At the other end, research into alternative fuels has been taken seriously due to concerns over the rising prices, depletion and non-biodegradable nature of fossil fuels. Both heterogeneous catalysts (such as NaOH, KOH) and homogeneous catalysts (such as metal oxides) have been established as key materials in the production of biodiesel or fatty acid methyl esters (FAME) from plant or animal-based triglycerides. The biodiesel is relatively cleaner than fossil fuels and the source materials can be ordinary domestic wastes. Catalysts are also used in the upgrading of heavy oils to lighter distillates.

Catalysis for Heavy Chemical Industry

Heavy chemical industries which manufacture (or produce) plastics, petrol, pesticides, pharmaceuticals and petrochemical products rely on catalysed processes. Ammonia (NH_3), used in the manufacture of fertilizer, is produced by Haber-Bosch process (Eq. 5), by the action of heterogeneous iron-based catalysts. Due to its significance, this process consumes 1% of global total energy (Capdevila-Cortada, 2019).

$$N_2 + 3H_2 \xrightarrow{\text{Fe catalyst}} 2NH_3 \tag{5}$$

The hydrogen used in the process is generated in-situ by reforming methane in presence of heterogeneous metal (such as alumina-supported nickel, Mg,

iron-promoted, or osmium) catalyst (Eq. 6), coupled with water–gas shift (WGS) reaction (Eq. 7) in presence of heterogeneous base metal catalyst.

$$CH_4 + H_2O \xrightarrow{Ni} CO + 3H_2 \quad (6)$$

$$CO + H_2O \xrightarrow{\text{Base metal catalyst}} CO_2 + H_2 \quad (7)$$

Furthermore, in order to obtain linear fatty alcohols by the Shell higher olefin process (SHOP), the first step involves the oligomerisation of ethylene in presence of homogeneous nickel (Ni) catalyst, followed by isomerisation, methathesisation, and then hydroformylation (Bhaduri and Mukesh, 2000).

Environmental and Health Applications

The exhaust of diesel engine consists of a complex mixture of gases, liquids and solids. There have been several technologies to remove different parts of the exhaust. From 1991 the United States and European Union have adopted the use of oxidation catalysts in vehicles to convert aldehydes, carbon monoxide (CO) and hydrocarbons to CO_2 and water. This process is called mineralisation. Only the NOx are removed by reduction to N_2, driven usually by precious metal catalysts such as platinum (Pt) or plasma-enhanced catalysts (Kim *et al.*, 2006). These purification redox reactions operate simultaneously at the same temperatures (< 300 °C).

Photocatalysis which was briefly highlighted above was soon recognised to have the capacity to provide many solutions based on its ability to mineralise hazardous chemical compounds. Titanium dioxide and ZnO photocatalyst are widely believed to be non-toxic, being important ingredients in tooth fillers. The commonest semiconductor photocatalyst, that is TiO_2, has found application in self-cleaning materials (e.g. Pilkington glass, tar and even the neck tie!), water purification, solar cells, and in organic photosynthesis.

HETEROGENEOUS CATALYSIS

In this part, we present our works with heterogeneous catalysts. Significant part of these are in the areas of semiconductor photocatalysis such as titanium dioxide (TiO_2), which, over the decades, have attracted overwhelming interest as remarkable photocatalyst in solar cells and in the transformation of recalcitrant organic compounds into benign products. Nanostructured TiO_2 exhibit an array of scientific and technological applications such as photocatalysis, sensors, voltaic cells,

shielding interference in communication field, reducing electromagnetic radiation and disinfection. In photocatalysis however, despite the high conversion efficiency of TiO_2, certain limitations have necessitated the search for alternative or improved preparations.

As the world is caught up in the constant need for energy and reliance on fossil sources, the search for alternative fuel and for increased fuel production from crude sources is imperative. Therefore, the remaining aspects of our work under heterogeneous catalysis are oriented around petroleum catalysis and biodiesel production.

Improvement of TiO_2 Photocatalysis

Basically, band gap energy, which corresponds to the energy difference between the lowest conduction band and highest valence band positions of the semiconductor, is an important factor governing the utilisation of light. The band gap energies of some common semiconductor photocatalysts at pH 0 are shown in Fig. 1. Experimental band gap energies may vary from the standard band gap energies in the figure depending upon the method preparation of the semiconductor and its physical characteristics.

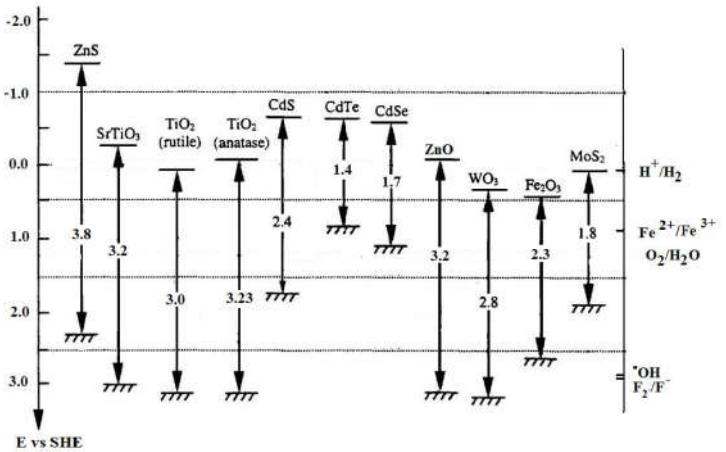

Fig. 1: *Band gap energies (eV) of representative semiconductor photocatalysts against normal hydrogen scale at pH 0*

The first process in photocatalysis, which is the semiconductor excitation and the generation of charge carriers, has been highlighted above. A schematic of the events that take place within and over the surface of semiconductor photocatalyst such as excitation, recombination and the formation of oxidising species is now depicted by Fig. 2. Basically, as photogenerated charge carriers are formed, they migrate fast within the semiconductor to the surface. Along their path, photophysical events such as trapping and recombination are encountered. Since the migration of the carriers is fast, most of their recombination (a negative process) occurs at the surface. In Fig. 2, surface reactions have been enclosed in **square brackets** and labelled separately to avoid misconception with lattice processes.

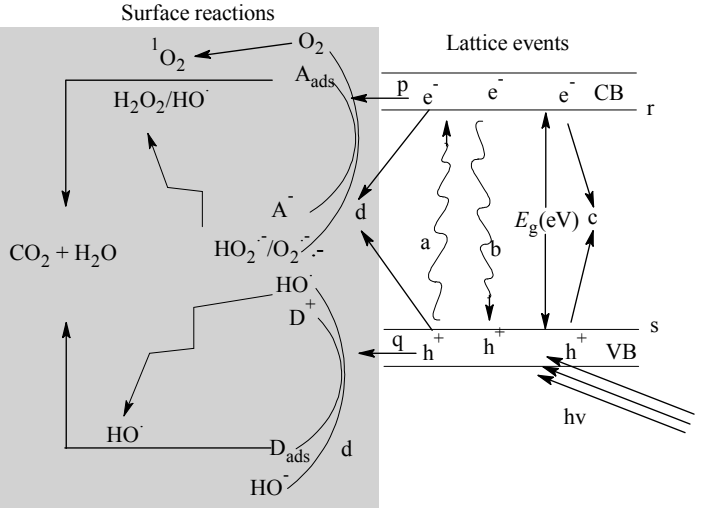

Fig. 2: *Schematic diagram showing the central events in semiconductor photocatalytic oxidation. Reproduced from Gaya (2015).*

Legend: (a) band gap excitation of electron, (b) band-band recombination, (c) recombination of electron and hole in the bulk, (d) surface recombination of electron-hole pair, (p) electron transfer, (q) positive hole oxidation, (r) lowest CB energy level, (s) highest VB energy level.

Semiconductor surfaces have the ability to conduct both oxidation and reduction reactions owing to the presence of charge carriers. The reducing adsorbate or donor (D_{ads}) undergoes hole oxidation while the oxidising adsorbate or acceptor (A_{ads}) undergoes reduction as shown by Eq. (8) and (9), which can be predicted based on standard hydrogen electrode (SHE) potential and band gap positions of the semiconductors.

$$e^-_{CB} + A_{ads} \longrightarrow A^-/A^{-\bullet}_{ads} \quad (8)$$

$$h^+_{VB} + D_{ads} \longrightarrow D^+/D^{+\bullet}_{ads} \quad (9)$$

The anatase and rutile phase of TiO_2, which are the commonest, exhibit large band gap (3.23 eV and 3.0 eV, respectively), which requires ultraviolet (UV) light for excitation. Unfortunately, only 3 to 5 % of the sunlight is in the form of UV which leads to the great quest to extend the utilisation of electromagnetic spectrum from UV region (290-400 nm) to cover visible light region (400-700 nm), or even up to near-infrared region. In addition, the titanium dioxide-based semiconductor photocatalysis is also limited by rapid electron-hole recombination (Rayalu et al., 2013). We have therefore participated in the race to improve titanium dioxide photocatalysis. Our focus as well as other workers are oriented around either reducing recombination and/or improving the utilisation of solar spectrum for effective photocatalysis.

Doping Approaches

One approach that plays a big role in reducing electron-hole recombination and improves the capacity for visible light photocatalysis is to incorporate a metal or non-metal into the semiconductor lattice. This is known as doping. We have performed both metal doping and non-metal doping of different semiconductor photocatalysts and a few of them are reported below. Due to the closeness of the ionic radius of Fe^{3+} (0.64 Å) to that of Ti^{4+} (0.68 Å), it was initially thought of as a potential good dopant to improve photocatalysis. However, previous works had reported the failure of this approach with a pyrolysis derived TiO_2 for the photocatalytic degradation of methyl orange 11 and 4-nitrophenol (Yalçın et al., 2010).

We thought the potential of iron-doping is still open for research, prepared 0.025-0.10 wt% Fe_2O_3-TiO_2 nanoparticles by sol-gel method using ethanolic solutions of iron (III) nitrate nonahydrate and titanium tert-butoxide and evaluated its efficiency by the degradation of 2,4-dichlorophenoxy acetic acid (Razani et al., 2017). The crystallinity and phase purity of the as-synthesised catalysts were characterised using Shimadzu XRD-6000 diffractometer provided with Ni-filtered CuKα radiation. The diffraction patterns are displayed by Fig. 3. The diffraction peaks of the Fe_2O_3-TiO_2 particles at 2-theta values of 25.3°, 37.0°, 37.8°, 38.6°, 48.3°, 55.1° correspond to 101, 103, 004, 112, 200, 211 reflections of anatase titanium

dioxide (JCPDS 01-073-1764) (Kao et al., 2007), with the 0.5 wt% doped catalyst showing optimum crystallinity.

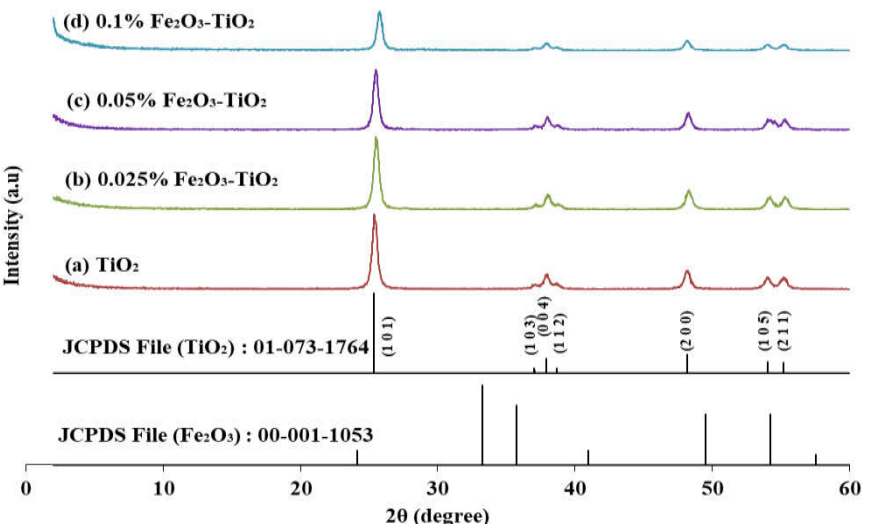

Fig. 3: *XRD pattern of Fe_2O_3-doped and undoped TiO_2 photocatalysts*

The Braunuer-Emmett-Teller (S_{BET}) surface area of the catalysts was determined at -196 °C, using Quanta chrome AS1 Win-automated gas sorptometer. The surface morphology of the catalysts was recorded on Hitachi 7100 transmission electron microscope (TEM), and the particle size data was analysed using Image J based free software. Fe^{3+} assay was obtained from x-ray fluorescence spectrometer (XRF). The mean particle size, band gap, Fe^{3+} and BET surface area the bare TiO_2 and the Fe_2O_3-doped TiO_2 of the nanopowders are presented in Table 2. The TEM, band gap profile and XRF profiles of the catalysts can be visualised from our reference paper (Razani et al., 2017).

Table 2: *Particle size, surface area, band gap energy and Fe^{3+} assay of the catalysts*

Catalysts	Average particle size (nm)	Surface area, S_{BET} (m^2g-1)	Band gap energy (eV)	Fe^{3+} assay (%)
Undoped TiO_2	21	34	3.20	0.000
0.025wt% Fe_2O_3-TiO_2	17	12	3.10	0.020
0.05wt% Fe_2O_3-TiO_2	13	15	3.07	0.046
0.10wt% Fe_2O_3-TiO_2	18	18	3.05	0.112

As seen from Table 2, the undoped TiO_2 has the highest particle size as well as surface area (34 m^2g^{-1}). The particle size (Fig. 4) increased steadily with doping from 13 nm in 0.05wt% Fe_2O_3-TiO_2 to 21 nm in 0.1wt% Fe_2O_3-TiO_2. Accordingly, the surface area of the doped catalysts diminished uniformly with doping from 18 m^2g^{-1} in 0.1wt% Fe^{2+}-doped TiO_2 to 12 m^2g^{-1}. Despite its anatase nature, which normally contributes to photocatalytic efficiency, and optimisation using face-centred central composite design (FCCD), only 49 % of aqueous 2,4-diphenoxy acetic acid was removed by the catalyst. This corroborates the findings of the previous researchers that Fe^{3+} acts as a recombination centre, leading to decreased catalyst efficiency (Asiltürk et al., 2009).

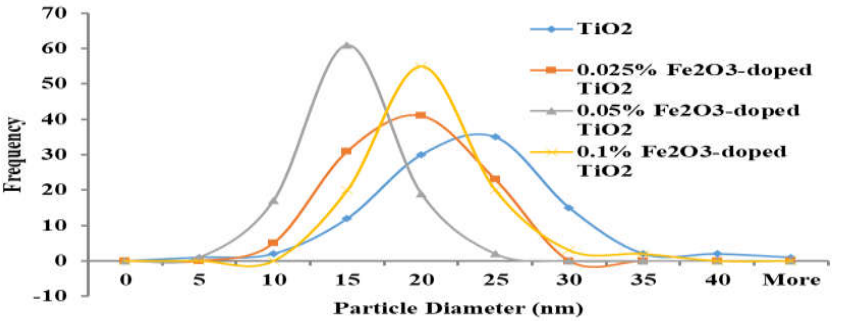

Fig. 4: *Particle size distribution of the 0 to 0.10 wt% Fe_2O_3-TiO_2*

Non-metal doping first began with the work of Asahi et al. (2001) using a nitrogen dopant, which showed remarkable photocatalytic efficiency. Subsequently, some many dopants such as N, I, C and S were utilised including by my research group. We were prompted based on the foregoing to prepare and investigate a mechanochemically nano-sized N-TiO_2 (Yusuf and Gaya, 2018). This material was

characterised with the aid of Philiphs X'pert X-ray diffractometer operated in the 2θ range of 20º to 120º.

The XRD patterns of the TiO_2 and N-doped TiO_2 are shown in Fig. 5. The N-TiO_2 showed sharp diffraction peaks of highly crystalline anatase phase (JCPDS 21-1272) at 2θ values of 25.6°, 38°, 48.32°, 54.14°, 55.83°, 62.92° and 75.28° while the bare TiO_2 showed reflections at 25.78º, 38.24º, 48.48º, 54.3º, 64.1°, and 75.48°. The bare TiO_2 had higher particle size and surface area (36 nm and 40 m^2/g) than the bare TiO_2 (43 nm and 39.6 m^2/g, respectively).

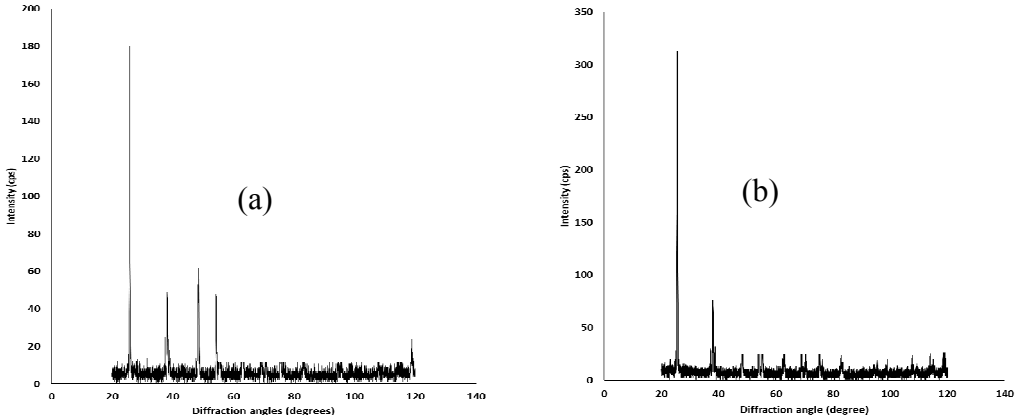

Fig. 5: *The XRD patterns of the as-synthesised materials. (a) Bare TiO_2. (b) N-TiO_2.*

The Functionalities on the titanium dioxide preparations were scanned in the range of 400 to 1000 cm^{-1} using Agilent Cary 630 spectrophotometer and the results are as displayed by Fig. 6. The figure confirms the substitution of lattice O by N species upon nitridation using urea molecule that resulted in the formation of N–Ti–O bonds. The peak at 550 cm^{-1} provides a tentative evidence for the N-Ti-O bonds. Further details on this catalyst can be obtained from Yusuf and Gaya (2018). The good news is that the doped TiO_2 can remove 97 % of aqueous caffeine (an emerging pollutant), with additional 6% removal over the bare TiO_2.

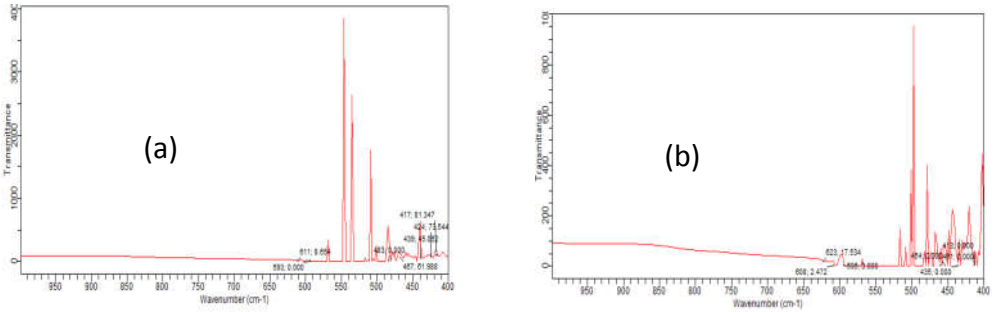

Fig. 6: *The FTIR spectra of the as-synthesised materials. (a) Bare TiO_2. (b) N-TiO_2*

Dye-Sensitised Nanoscopic Catalysts

Dye-sensitization has been effective in various applications such as selective oxidation of alcohols, photocatalytic degradation and solar cell. In this process, a dye molecule is excited to produce electron which can be easily injected to the conduction band of the semiconductor (SC) for onward formation of oxidizing species which can be utilized in organic reactions, as shown in Eq. (10) to (14).

Photoabsorption: $\text{Dye} \xrightarrow{h\nu\,(\text{vis})} \text{Dye}^*$ (10)

Dye excitation: $\text{Dye}^* \longrightarrow \text{Dye}^+(e^-)$ (11)

Electron injection: $\text{SC} + \text{Dye}(e^-) \longrightarrow \text{SC}(e^-_{CB}) + \text{Dye}^+$ (12)

Recovery of neutral dye: $\text{SC}(e^-_{CB}) + \text{Dye}^+ \longrightarrow \text{SC} + \text{Dye}$ (13)

Organic reaction: $\text{Organic} + \text{ROS} \longrightarrow \text{Photoproducts}$ (14)

Both dye-sensitisation and doping are prominent coupling and band-gap modification approaches that successfully improve the visible light utilization of TiO_2. Based on the fact that the visible light photoactivity of Ag-doped TiO_2 has been established and the dye sensitized coupled photosystems have been reported, we investigated a hybrid system of Eosin Y (EY) and Ag-doped TiO_2 for the removal of aqeous caffeine, compound **(4)** (Ibrahim and Gaya, 2019).

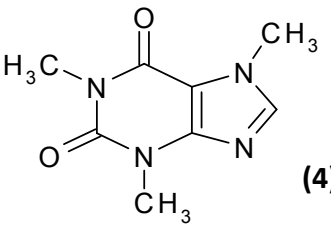

(4)

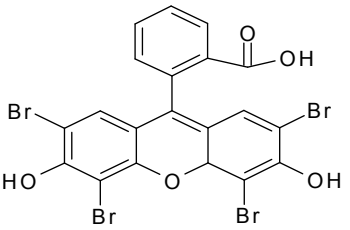

(5)

The Eosin Y (EY), compound **(5)**, was severally found to be an excellent sensitizer (Wang et al., 2017). The effect of operating variables (initial caffeine concentration, catalyst dosage, pH and temperature) in the degradation of caffeine over the EY/Ag-TiO_2 was studied using a three-levels-four-factor Taguchi orthogonal array (OA) L_9 $(3)^4$ design exploiting Minitab 17 statistical software package. Nine degradation experiments were performed at three experimental levels as displayed in Table 3.

The photocatalytic degradation of caffeine was also optimised using face-centred central composite design (FCCD) made of 20 experiments (N) based on the formula $N = 2^n + 2n + 6$, and using combinations of three independent factors (the pH-A, EY/Ag-TiO_2 concentration-B, and initial caffeine concentration-C) at three levels (Table 4).

Table 3: *Experimental factors, levels and codes as used for the Taguchi design*

Experimental factors (& codes)	**Levels**			**Units**
Codes	1	2	3	
Catalyst Dosage (A)	1	1.5	2	gL^{-1}
pH (B)	3	6	8	-
Temperature (C)	35	45	65	°C
Caffeine level (D)	10	30	50	mg/L

Table 4: *Experimental factors and levels used in the FCCD*

Experimental variables	**Notation (& unit)**	**Levels (& codes)**		
pH	A	3.0(-1)	5.5(0)	8.0(+1)
Catalyst dose	B (g/L)	1.00(-1)	1.75(0)	2.50(+1)
Caffeine concentration	C (mg/L)	10(-1)	30(0)	50(+1)

The synthesised EY/Ag-TiO_2 was characterised using X-ray diffraction (XRD), and refined by Rietveld profile method using WINPLOTR package of FullProf suite Version 3.0. The crystallite sizes of the catalysts were calculated using Williamson-Hall (Eq. 15) and the Scherer equation (Eq. 16).

$$\beta \cos\theta = \frac{K\lambda}{size} + 4\varepsilon \text{ x } \sin\theta \qquad (15)$$

$$\text{Crystallite size} = \frac{K\lambda}{\beta \cos\theta} \quad (16)$$

Where K is 0.891, λ is the wavelength of X-ray radiation, β is the full width at half maximum intensity (FWHM) in rads, θ is diffraction angle at the position of peak maximum and ε is the strain. Anatase and rutile contents of the titania photocatalysts were calculated using Spurr-Myers equation (Eq. 17) which has been widely found applicable (Zhang et al., 2013).

$$w_A = \frac{1}{1+1.26\frac{I_R}{I_A}} \quad (17)$$

Where w_A is the weight fraction of anatase, I_R is the intensity of rutile peak and I_A is the intensity of anatase peak. The lattice parameters (a, b and c) of EY/Ag-TiO_2 photocatalyst were calculated using Eq. (18) based on anatase planes (101 and 004), and rutile reflections 111 and 211. The d in the equation is the spacing between atomic lattice planes, the h, k and l are the miller indices, and a, b and c are lattice parameters.

$$\frac{1}{d^2} = \frac{h^2+k^2}{a^2} + \frac{l^2}{c^2} \quad (18)$$

The calculated values for the anatase and rutile polymorphs were compared to the unit cell parameters for standard anatase (JCPDS card no. 21-1272) and rutile (21-1276) polymorphs of TiO_2 (Table 5), respectively. It would be seen that the values displayed in Table 5 are consistent with the unit cell parameters for pure anatase (a= 0.3784 nm and c = 0.9515 nm) and pure rutile (a = 0.4536 nm and c = 0.29587 nm) (Hanaor and Sorrel, 2011). This confirms that the EY/Ag-TiO_2 contains a mixture of tetragonal anatase and rutile polymorphic structures. The mass percentages of these phases in the regular TiO_2 were 97.6 and 2.32 %, respectively.

Table 5: *Crystal structure properties of the as-synthesised EY/Ag-TiO_2*

Property	**EY/Ag-TiO_2**	
	Anatase unit	Rutile unit
Crystal structure	Tetragonal	Tetragonal
Lattice structure (nm)	a = 0.370	a = 0.453
	c = 0.947	c = 0.295
Unit cell volume (nm^3)	0.136	0.258

The XRD profile of EY/Ag-TiO_2 (Fig. 7) shows amorphousness resulting from the sensitization with 73.9 % anatase, and 26.1 % distributed among rutile and

amorphous material in a similar manner to the popular active Degussa P-25 which has 70-80 % anatase. Unless the analysis of polymorphic content is performed, it will be difficult to conclusively state if amorphous TiO_2 has not been formed. The average crystallite size of the EY/Ag-TiO_2 was calculated using the Williamson-Hall profile. The Williamson particle size of the EY/Ag-TiO_2 dropped from 138 nm to 69.32 nm.

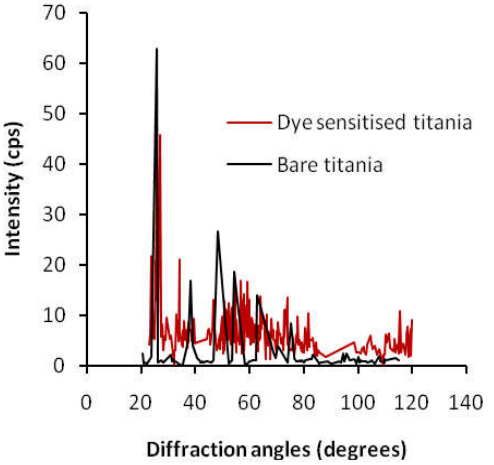

Fig. 7: *An overlay of diffraction patterns of EY/Ag-TiO_2 and bare TiO_2*

Taguchi and FCCD Optimisation of Reaction Factors

The effect of operating parameters in the degradation of caffeine over the EY/Ag-TiO_2 was investigated using the Taguchi and FCCD models. In the Taguchi approach (Table 6), the influence of experimental factors was ranked based on delta, the difference between the maximum and the minimum S/N ratios for a particular experimental factor. The order of influence is pH (B) > initial caffeine concentration (D) > EY/Ag-TiO_2 dosage (A) > temperature (C) which corroborates the fact that photocatalytic reactions are not affected by minor variations in temperature (Carp et al., 2004). Similarly, the well-known dependence of the photocatalytic process on pH (Marques et al., 2013) has been observed.

Table 6: *Signal to noise (S/N) ratios for the parameters of caffeine degradation*

Level	A (g/L)	B	C (°C)	D (mg/L)
1	37.61	37.40	36.94	37.81
2	36.49	39.27	37.49	36.29
3	37.08	34.51	36.75	37.27
Delta	1.12	4.76	0.73	1.72
Rank	3	1	4	2

From Table 6, the optimal levels for each experimental factors obtained according to Taguchi's "the larger the better" criteria are accordingly, 2 g/L catalyst, pH 6, 45 °C temperature and 50 mg/L initial caffeine concentration. The optimum pH attained roughly matches the pH at point of zero charge of TiO_2 (pH_{pzc} = 6.25) (Hoffmann et al., 1995) which implies that pH will affect the adsorption equilibrium when exceedingly low or high, resulting in poor degradation.

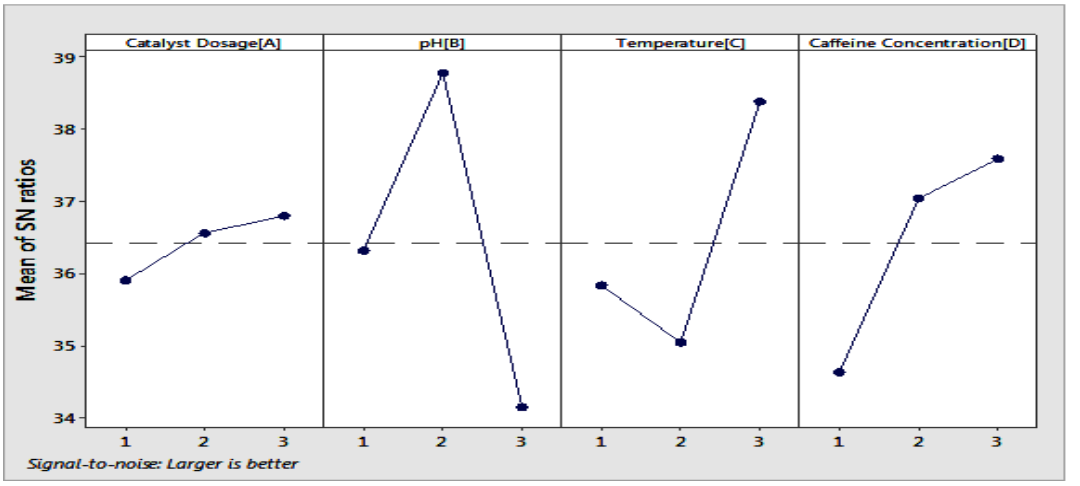

Fig. 8: *Main effect plots for the S/N ratios depicting the effect of pH, catalyst dosage, temperature and initial concentration of caffeine*

The influence of reaction variables in the degradation of caffeine can further be explained based on main effect. Main effect is said to occur when the mean response changes across the level of experimental factors. The sign of the main effect indicates the direction of the effect. Figure 8 shows that the temperature has negative

effect on the photocatalytic degradation process whereas catalyst dosage and initial caffeine concentration have positive effect. The positive effect of catalyst loading might be attributed to the corresponding increase in the number of site available for the photodegradation process.

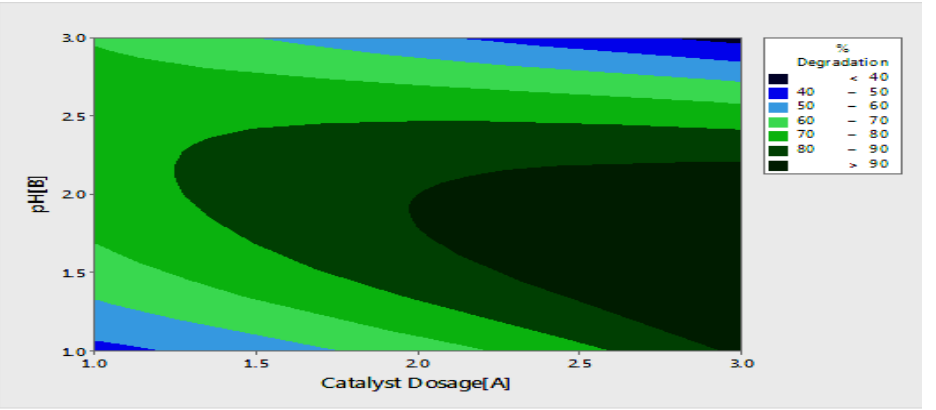

Fig. 9: *Contour plot of percentage degradation versus pH and catalyst dosage*

To predict the region where optimum degradation lies, contours (Fig. 9) were plotted using the most significant factors in the caffeine removal (pH and caffeine concentration). The isolines on the contour plot represent distinct level of design parameter while the darker portion of the plot is within the range of level of pH 1 to 3 and catalyst dose of 2 to 3 g/L represent the area where there is highest probability of finding the optimum response (> 90 %). The maximum of the contour plot where the degradation efficiency will be greater than 90 % corresponds to level 2 for both the pH catalyst dosage pointing to pH 6 and catalyst dose of 1.5 g/L^{-1}.

Table 7: *Efficiency of combinations of levels of factors for caffeine removal*

Run	Factors			Degradation efficiency, % D	
	pH (A)	***Catalyst (B; g/L)***	***Caffeine (C; mg/L)***	**(Experimental)**	**(Predicted)**
1	3.0(-1)	2.5(+1)	50(+1)	50	53.15
2	8.0(+1)	2.5(+1)	50(+1)	82	76.05
3	8.0(+1)	1.75(0)	30(0)	90	78.20
4	8.0(+1)	2.5(+1)	10(-1)	92	107.35
5	3.0(-1)	1.75(0)	30(0)	44	65.80
6	3.0(-1)	2.5(+1)	10(-1)	74	63.45
7	8.0(+1)	1.00(-1)	10(-1)	87	81.35
8	5.5(0)	1.75(0)	30(0)	90	84.00
9	5.5(0)	1.75(0)	50(+1)	60	73.10
10	5.5(0)	1.75(0)	30(0)	73	84.00
11	5.5(0)	1.75(0)	30(0)	87	84.00
12	5.5(0)	1.75(0)	30(0)	95	84.00
13	3.0(-1)	1.00(-1)	10(-1)	76	79.45
14	5.5(0)	1.00(-1)	30(0)	76	81.00
15	5.5(0)	1.75(0)	30(0)	86	84.00
16	5.5(0)	1.75(0)	10(-1)	97	84.00
17	5.5(0)	2.5(+1)	30(0)	96	87.00
18	8.0(+1)	1.00(-1)	50(+1)	40	48.05
19	5.5(0)	1.75(0)	30(0)	80	84.00
20	3.0(-1)	1.00(-1)	50(+1)	85	67.15

Table 8: *Analysis of variance for the response surface reduced quadratic model*

Source	Sum of squares	DF	Mean square	F-value	Prob > F	Remark
Model	3487.00	7	498.14	2.95	0.0479	Significant
A	384.40	1	384.40	2.28	0.1569	
B	90.00	1	90.00	0.53	0.4790	
C	1188.10	1	1188.10	7.05	0.0210	
A^2	720.00	1	720.00	4.27	0.0611	
AB	882.00	1	882.00	5.23	0.0411	
AC	220.50	1	220.50	1.31	0.2751	
BC	2.00	1	2.00	0.012	0.9151	
Residual	2023.00	12	168.58			
Lack of Fit	1724.17	7	246.31	4.12	0.0691	Not significant
Pure Error	298.83	5	59.77			
Cor Total	5510.00	19				

Similarly, the values of degradation efficiency obtained from FCCD experiments (% D) were processed using response surface methodology. The results are listed in Table 7. Obviously, there is good correlation between the experimental and predicted degradation efficiencies. The relationship between the degradation efficiency of caffeine (% D) under the interplay of the independent variables of the study A, B and C is best represented by the reduced linear quadratic model shown in Eq. (19).

$$\% D = 84 + 6.2A + 3B - 10.9C - 12A^2 + 10AB - 5.25AC + 0.5BC \qquad (19)$$

The response surface model was statistically adjudged using the analysis of variance (ANOVA) shown in Table 8, which displays a model's Prob > F less than 0.05 and a Prob > F of 6.91 % for the lack-of-fit value. These indicate very low probability of occurrence due to noise and that the predicted degradation efficiencies are not influenced at 95 % confidence level. Some measures of dispersion associated with the model of this study such as the model PRESS value (17,967), the minimum adequate precision (> 4), and the adequate precision (7.221) further confirm adequate model discrimination and negligible noise.

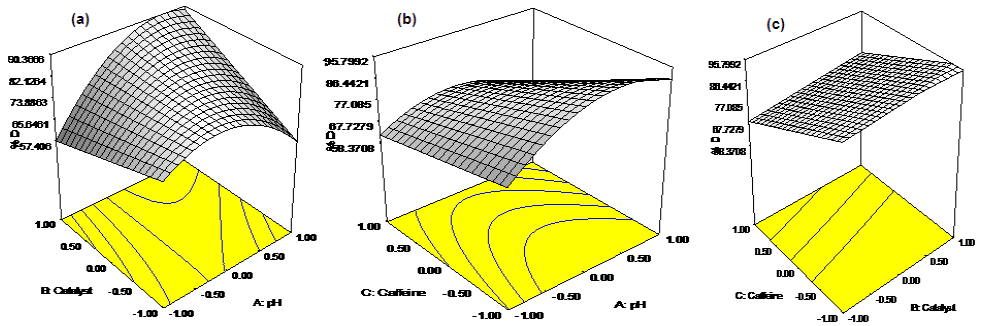

Fig. 10: *Response surfaces illustrating the effect of (a) pH versus EY/Ag-TiO_2 concentration (b) pH versus caffeine concentration (c) caffeine versus catalyst concentration.*

The overall effect of the operating factors in the FCCD are illustrated by the 3D response surfaces in Fig. 10. Figure 10a shows synergistic effect between catalyst concentration and pH values as they are increased towards the intermediate levels

(1.75 g/L and pH 5.5, repectively) and a maximum degradation efficiency up to 87 % can be reached. One the combinations of these factors is alternated low degradation efficiency is observed. The same observation applies to pH and caffeine concentration (Fig. 10b). However, in the case of catalyst and caffeine concentration (Fig. 10c), the degradation efficiency decreased as the amount of these variables is increased. This can be attributed to the screening of light by these materials as they are increasingly present.

Kinetics of Caffeine Removal

The effect of photolysis and bare TiO_2 adsorption and photocatalysis were compared in 290 min, with the photocatalytic degradation profiles over EY/Ag-TiO_2, Ag-doped TiO_2 and EY-sensitized TiO_2. The results as in Fig. 11 show the following order photocatalytic efficiency, EY/Ag-TiO_2 (95 %; Fig. 11d) > EY-sensitized TiO_2 (68%; Fig. 11c) > Ag-doped TiO_2 (52 % removal; Fig. 11b) > bare-TiO_2 photocatalysis (37 %; Fig. 11e) > irradiation alone (no removal; Fig. 11a). Kinetic profiles based on pseudo zero-order and pseudo first-order integrated rate equations (Eq. 20 and 21, respectively) were plotted for experiments at 1.75 g/L, pH 5.5 and 10 mg/L initial caffeine concentration, $[\text{Caffeine}]_o$.

$$[\text{Caffeine}]_t = [\text{Caffeine}]_o - k_o' t \quad (20)$$

$$\ln[\text{Caffeine}]_t = \ln[\text{Caffeine}]_o - k_1' t \quad (21)$$

Where $[\text{Caffeine}]_t$ is the caffeine concentration at time t. The rate constant corresponding to each equation was obtained from the slope.

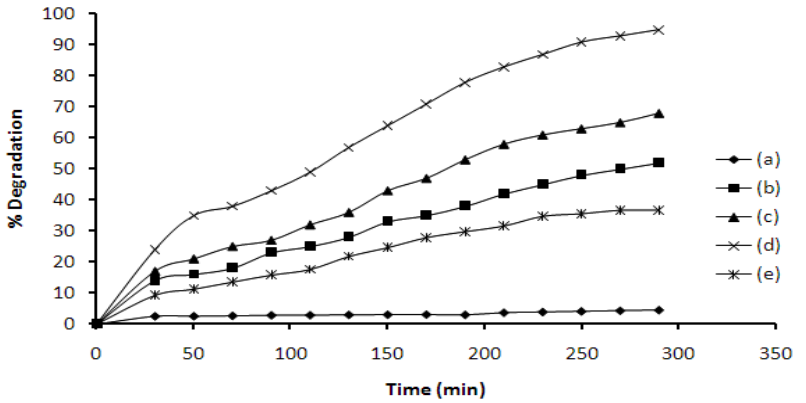

Fig. 11: *Caffeine degradation profiles under different conditions. (a) Irradiation alone. (b) Ag-TiO_2. (c) EY-TiO_2. (d) EY/Ag-TiO_2. (e) TiO_2*

Table 9: *Kinetic parameters for EY/Ag-TiO_2 and TiO_2*

Titanium dioxide	Pseudo first-order			Pseudo zero-order			Ref.
	k_1 (10^{-3}mol/dm^{3}s)	R^2	%D	k_o (10^{-3} /min)	R^2	%D	
EY/Ag-TiO_2 (69.32 nm)	3	0.956		1.7	0.988	95	Our study
Bare TiO_2 (138.64)	6	0.965		1.5	0.934	37	Our study
NF-TiO_2 (50 nm)	14.6	-	77	-	-		Barndök et al. (2013)
NF-TiO_2 (300 nm)	6.56	-	32	-	-		,,
TiO_2 nanotube (10 nm)	-	-	51	-	-		Arfanis et al., (2017)

As seen from Table 9, the degradation of caffeine over EY/Ag-TiO_2 was consistent with pseudo zero-order kinetic scheme with rate constant (k_o) of 1.7 x 10^{-2} min^{-1} (R^2 ≈ 0.99) as opposed to the bare TiO_2 whose reaction proceeds by a pseudo first-order scheme. In other words, improved degradation efficiency was observed upon downsizing from 138.64 nm to 69.32 nm which is inconsistent with the observation

of Barndök et al. (2013) with a monodisperse anatase TiO_2 but in agreement with many majority of workers. The caffeine degradation efficiency we obtained with the EY/Ag-TiO_2 (Table 9) is higher than that of titanium dioxide nanotube (Arfanis et al., 2017). More so, unlike in the removal of caffeine by ozonation (Rosal et al., 2009), the degradation efficiency continued to steadily increase until the degradation of almost all of the original caffeine.

Quantal Evidence for Electron Injection

We investigated the electron injection from dye to TiO_2 and the energies associated with EY and EY sensitized TiO_2 using density functional theory (DFT) calculations based on the hybrid B3LYP functional. The optimized geometries of the EY and EY/TiO_2 are displayed in Fig. 12a. The EY-sensitized TiO_2 framework is made up of Ti_5O_{10} cluster attached to the carboxylic acid group of the EY molecule through a bidentate bridge. The calculated average Ti-O bond distance (1.97685 Å) is within the range reported by past workers (1.949 to 1.980 Å) (Mo et al., 1995). The dipole moment of the EY/TiO_2 (8.2175 μ) is larger than that of EY (5.8244 μ) which indicates increased electronegetivity due to the Ti-O bond. The C10-C11 bonds of both the models are 1.34505-1.3942(Å), which implies a π-conjugation nature of the bonds.

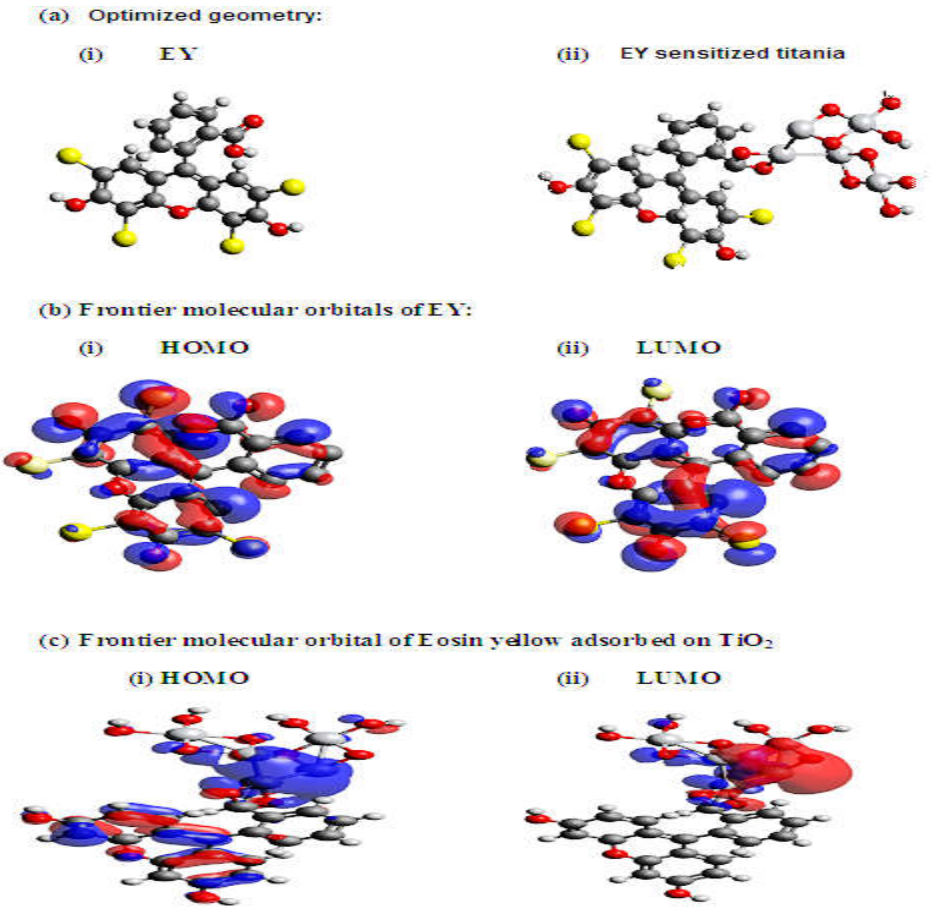

Fig. 12: *(a) Optimized geometry of Eosin Y and EY/Ag-TiO_2. (b) Frontier molecular orbitals of Eosin Y. (c) Frontier molecular orbitals of EY/Ag-TiO_2. Colour scheme: White = H, blue = N, red = oxygen, grey = carbon*

The frontier molecular orbital of the EY and EY/TiO_2 are displayed in Fig. 12b and Fig. 12c. In that of the EY, the electronic distribution of the highest occupied molecular orbitals (HOMO) and lowest unoccupied molecular orbitals (LUMO) shows delocalisation over π-conjugation system of the three benzene rings and the highest electron density is centered on the carboxylic acid functional group which indicates the ease with which electrons can be injected to conduction band of the semiconductor photocatalyst. Generally, for electrons to be effectively injected into the conduction band of the semiconductor photocatalyst, the LUMO eigenvalue of

the dye molecule most be sufficiently more negative than the conduction band edge of TiO_2 (0.5 V) (Dette et al., 2014). The eigenvalue for the HOMO and LUMO orbitals of the EY molecule were -0.24944 and -0.7246 eV while for the Eosin Y-sensitized photocatalyst model these were -0.1511eV and -0.1827, respectively. It can be readily seen that, the energy gap (ΔE) between the HOMO and LUMO is larger in the case of the EY sensitized catalyst than the bare TiO_2 which implies the ease with which electrons can be injected into conduction band of the TiO_2 from the EY dye. The energy gap in the case of the sensitized catalyst is less than 0.5 eV, thus falling within the range for molecules with unusual electronic properties such as intramolecular electron transfer in solution (Perepichka and Bryce, 2005) and perhaps effective sensitization as in the present case.

Table 10: *Transition parameters of EY and EY/Ag-TiO_2*

Model	Wavelength (nm)	Energy(eV)	Oscillator strength (*f*)
EY	507	2.445759	0.1116
	412	3.009709	0.0928
	265	4.679245	0.0252
	247	5.020243	0.0061
EY-TiO_2	844	1.469194	0.0071
	549	2.258652	0.0052
	426	2.910798	0.0375
	298	4.161074	0.0500

Absorption spectra of EY and EY-TiO_2 were calculated by the DFT/B3LYP On the basis of optimized ground state geometries displayed in Fig. 12a and the results are shown in Table 10. The table shows the first optically excited transition of Eosin Y dye and Eosin Y-sensitized TiO_2 and the oscillator strength for singlet-singlet excitations. The most probable transitions were determined based on the value of the oscillator strength (*f*). The results predict extended absorption spanning beyond the visible region of the electromagnetic spectrum (298 to 844 nm). This range brackets the experimental wavelength of maximum absorption of EY (λ_{max} 507 nm) determined in this study.

Sculpturing Low TiO_2 Dimensionalities

Many recent alterations of nanostructured TiO_2 are of a morphologic nature such as mesoporous structures, designed faceted crystallites, hybrids, or low dimensional structures (0D, 1D, 2D, 3D). We have in the recent years focussed on low dimensionalities as reported under the below headings.

One-Dimensional (1D) TiO_2 Nanowires

Various shapes of 1D TiO_2 nanomaterials such as nanowires, nanotubes, nanofibers, nanoribbons, nanobelts, and nanoneedles have been synthesised for use in different technological applications due to their faster charge carrier transfer, lower chances of recombination, higher surface area and photoactivity relative to 0D TiO_2 nanoparticles (Shao et al., 2017; Zhang et al., 2018). We thought an alkali hydrothermal method would make a simple, cost-effective, highly reactive, easily controlled and environmentally safe route to prepare 1D nanostructures such as TiO_2 nanowire (TNW). Even though, these materials have been successfully synthesised by other methods, contamination due to prior use of template or catalyst was inevitable (Yang et al., 2019).

Using Degussa P25 TiO_2, we successfully prepared TNWs (with a clear collapse of the definitive rutile 110 XRD reflection) using alkali (NaOH/KOH) hydrothermal treatment of TiO_2 nanoparticles but NH_4OH treatment did not yield nanowires (Fig. 13) (Hamisu et al., 2020a). Compositional analysis of the as-prepared titanium dioxides using energy dispersive x-ray (EDX) spectroscopy shows peaks corresponding solely to Ti and O (Fig. 14). This observation dispenses with the presence of impurities in the obtained TNWs and the TNPs.

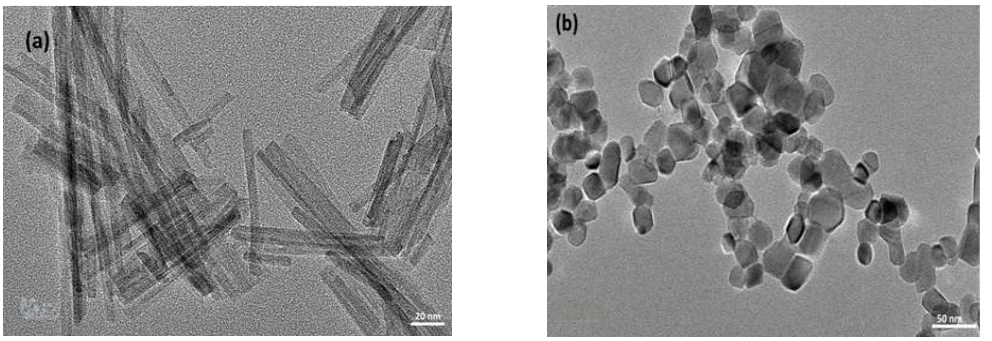

Fig. 13: *(a)The TEM image of KOH-TNW and (b)NH_4OH-based TNP*

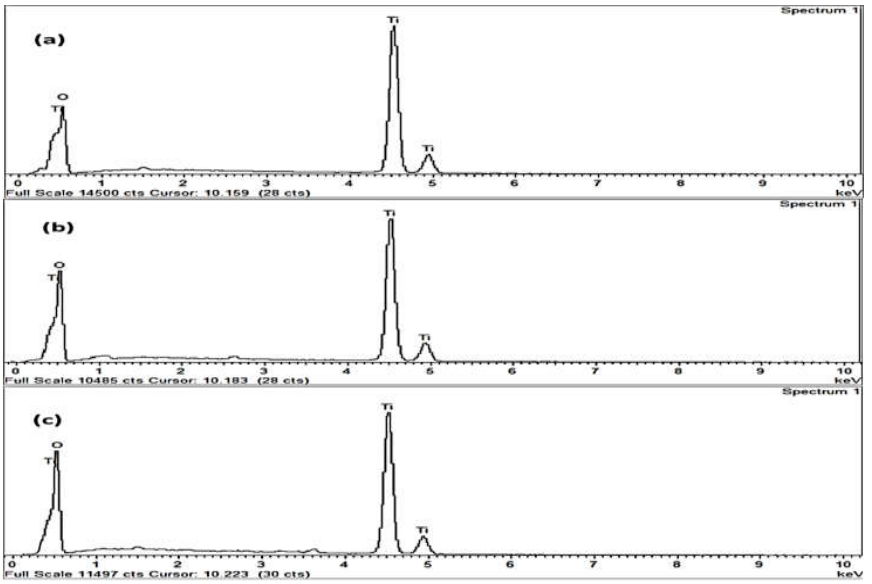

Fig. 14: *The EDX spectra of (a) NH_4OH-TNP, (b) NaOH-TNW and (c) KOH-TNW*

The surface area and pore volume of the hydrothermal titania were estimated using Brunauer-Emmett-Teller (BET) and Barrett-Joyner-Halenda (BJH) methods. Figure 15 shows the N_2 adsorption-desorption isotherm, the BET surface area plot (left inset) and the BJH adsorption cumulative pore volume curve (right inset) for Degussa P25, NH_4OH-TNP, NaOH-TNW, and KOH-TNW. The NaOH-TNW (Fig. 15c) and KOH-TNW (Fig. 15d) exhibited the highest values of these parameters (143.42 m^2/g and 0.46 cm^3/g, and 228.34 m^2/g and 0.62 cm^3/g, respectively). They show a type IV IUPAC isotherm, with obvious mesoporosity indicated by the associated hysteresis loops and condensation/evaporation steps within low partial pressure ranges (0.6 to 0.9), common with low dimensional structures (Zulfiqar et al., 2018). Thanks to their large specific surface area, the most remarkable photocatalytic efficiency (98.87 %) was obtained with KOH-TNWs, perhaps because of ease of the transfer of photogenerated carriers along the axial direction (Zhang et al., 2015).

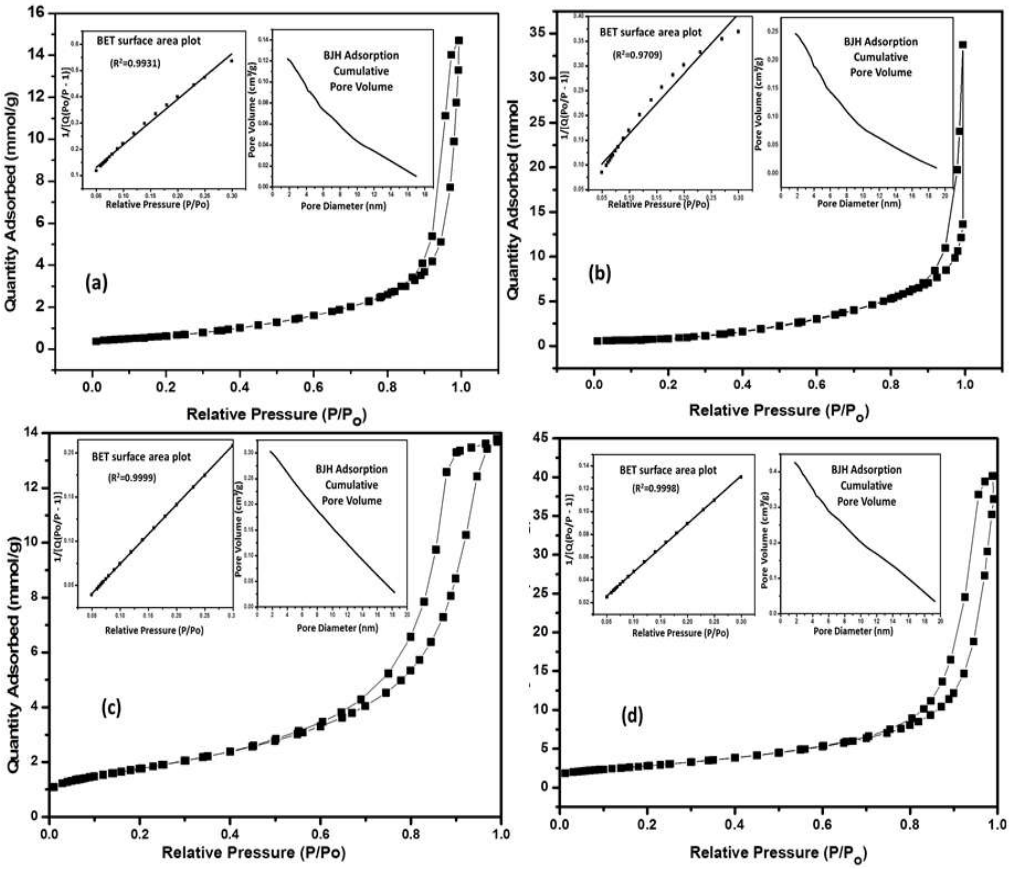

Fig. 15: *Nitrogen adsorption-desorption isotherms with BET surface area plot (left inset) and BJH adsorption cumulative pore volume curve (right inset) for (a) Basic P25 TiO_2, (b) NH_4OH-TNP, (c) NaOH-TNW and (d) KOH-TNW*

The band gap of the obtained P25 TiO_2, NH_4OH-TNP, NaOH-TNW and KOH-TNW were estimated based on reflectance measurements. The UV–Vis reflectance spectra over wavelengths of 220–800 nm are displayed in Fig. 16a while the band gap energies of the photocatalysts, estimated from the plot of reflectance function $[F(R\alpha)h\nu]^2$ against $h\nu$ are displayed in Fig. 16b. The corresponding band-gap energies of the above catalysts as calculated were 3.25, 3.15, 3.04 and 2.94 eV, respectively, which shows a red shift as alkali strength is increased.

The effect of operating variables on the degradation of aqueous methylene blue (MB) over the obtained alkali hydrothermal TiO_2 was optimised using response surface methodology, based on a bivariate central composite design (CCD) and optimized numerically and described by a quadratic model (Hamisu et al., 2020a). Kinetic profiles revealed the least in the order of degradation performance to be P25 (77.12 %) while K/TNW (98.87%) was the most effective catalyst. The results correlate well with the BET and UV-Vis results which showed better MB removal as surface area of K/TNW is increased or its band gap is decreased.

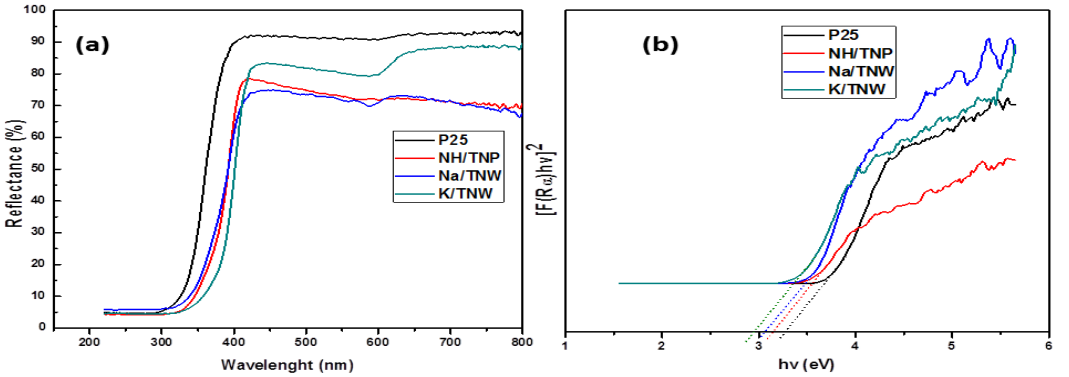

Fig. 16. (a) UV–Vis reflectance spectra of the samples (b) Plot of $(F(R\alpha)h\nu)^2$ versus $h\nu$ of the samples for band gap evaluation.

Novel Methods for Fabricating 2D and 3D Mesoporous TiO_2

The demand for nanostructured materials keeps increasing due to possible utilisation in array of applications such as catalysis, solar cells, lithium rechargeable batteries, sensors and hydrogen evolution. The synthesis of mesoporous TiO_2 has become extraordinarily important due to its controllable properties, large surface area, adsorption capacity, good permeability, and high photocatalytic activity. It all began with the synthesis by a template-assisted sol-gel approach (Antonelli et al., 1995), followed by hydrothermal, evaporation-induced self-assembly, and precipitation. However, obtaining stable, high surface area and controllable TiO_2 mesostructures remains a major challenge for the workers in this field. Until our work, after calcination, mesoporous TiO_2 exhibits low surface areas and small pore sizes due to either the uncontrollable hydrolysis/condensation reaction with H_2O (which is difficult to match with the templates), or due to the poor thermal stability of the mesostructure and subsequent collapse upon calcination (Nguyen et al., 2016).

The anatase is the most common and widely prioritised TiO_2 phase followed by rutile and brookite. To achieve high photoactivity, mesoporous anatase powders with small particle size and high crystallinity are desirable. However, the synthesis of this material with high quality is a challenge. For instance, Xiao et al. (2006) have prepared a nano-anatase but were faced with significant mesopore collapse. Similarly, Mao-Xiang et al. (2009) have prepared some mesoporous anatase titania with high surface area by a precipitation method but could not achieve small particle sizes.

Recently, we developed a new precipitation-template based synthesis for mesoporous TiO_2, in which a polyvinyl alcohol (PVA) template is applied after precursor precipitation (Hamisu et al., 2020b). In our method, $Ti(OH)_4$ was precipitated out of $TiCl_3$ solution with NH_4OH, washed until neutrality, and acidified with dilute nitric acid to form a suspension. Templated TiO_2 namely $0.25PV/TiO_2$, $0.5PV/TiO_2$ and $1PV/TiO_2$ were formed by the addition of 0.25g, 0.5g, 1.0 g of PVA solution, and heating at 75 ^oC for 4 h. The mixture was kept overnight at room temperature, dried at 110 ^oC and calcined in air at 450 ^oC for 4 h. Accordingly a template-free TiO_2 ($0PV/TiO_2$) was prepared devoid of PVA.

The precipitation-derived mesoporous anatase TiO_2 was characterised using the Brunauer-Emmett-Teller (BET) method based on N_2 adsorption-desorption isotherms obtained for $0.25PV/TiO_2$, $0.5PV/TiO_2$, and $1PV/TiO_2$ from a Micromeritics 3Flex 1.02 instrument at 77.322 K (Fig. 17 A, B and C, respectively). Comparison with IUPAC classification reveals type IV isotherms (Cano-Casanova et al., 2018), with mesoporosity represented by the presence of hysteresis loops and clear condensation/evaporation steps at low partial pressures (0.6 to 0.9).

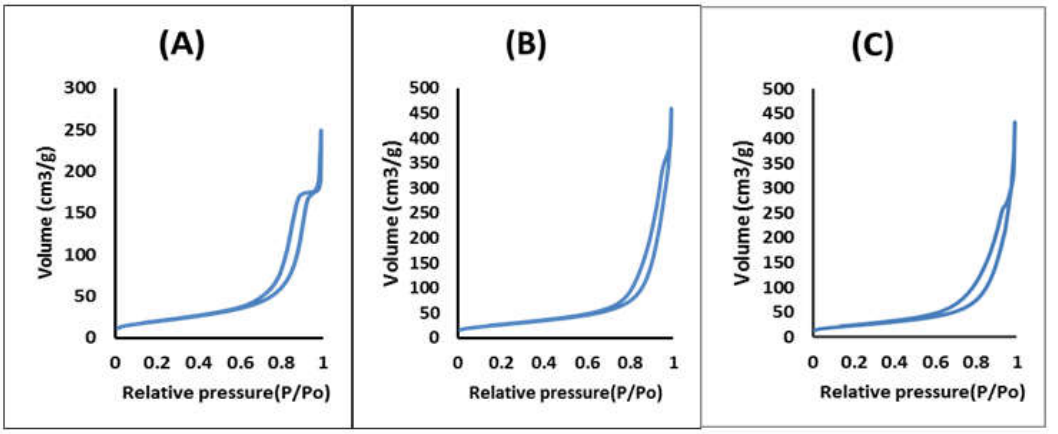

Fig. 17: *The N_2 isotherm over 0.25PV/TiO_2 (A), 0.5PV/TiO_2 (B) and 1PV/TiO_2 (C)*

Table 11: *The surface properties of TiO_2 obtained from N_2 adsorption-desorption data*

Sample	Scherer crystal size (nm)	Surface area (m^2/g)	Pore volume (cm^3/g)	Pore size (Å)	
				Adsorption	Desorption
0.25PV/TiO_2	10.22	73.2513	0.385254	203.9197	210.3735
0.5PV/TiO_2	8.68	97.4042	0.713045	281.2305	292.8189
1PV/TiO_2	9.23	82.7001	0.670765	315.8560	324.4327

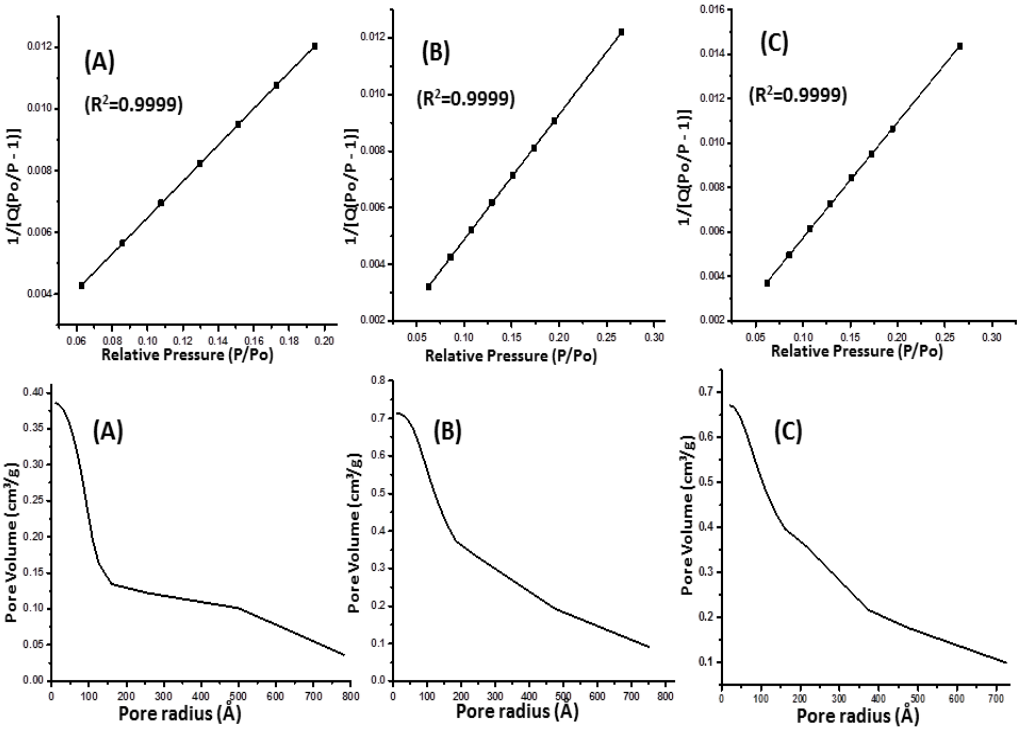

Fig. 18:. *BET surface area plot (top) and BJH Adsorption Cumulative Pore Volume (bottom) for 25PV/TiO_2 (A), 0.5PV/TiO_2 (B) and 1PV/TiO_2 (C)*

The surface area and pore volume were estimated using Brunauer-Emmett-Teller (BET) and Barrett-Joyner-Halenda (BJH) cumulative pore volume methods as displayed in Fig. 18 (top set) and (bottom set), respectively. A summary of the surface area, pore volumes and sizes of these catalysts is given by Table 11. As may be seen, the values of BET surface area and pore volume increase with corresponding increase in the PVA up to 1 g, beyond which, a decrease in these properties is generally observed due to exceedingly high PVA. Similar observations were made previously by Liu et al. (2018) and Nguyen et al. (2016) upon application of P123 and ethylene glycol as templates in the synthesis of mesoporous TiO_2, respectively. In this study, the highest BET surface area and pore volume were obtained with the 0.5PV/TiO_2, which implies that only an optimum PVA template can play a positive role in the post-precipitation templating.

The dominant polymorphic phase of the catalysts was characterized by Powder X-ray diffraction (PXRD) using a Shimadzu XRD-6000 X-Ray Diffractometer in the 2θ range of 20-80°. As seen from Fig. 19, all the catalyst specimens show anatase diffraction peaks at 2θ (and planes) at 25.44° (101), 38.07° (004), 48.12° (200), 54.02° (105), 55.21° (211), 62.76° (204), 70.01° (116), 94.92° (215). Interestingly, neither brookite nor rutile phases are seen even after templating. Rietveld profile refinement of the structures was carried out using FullProf suite version 6.30. The lattice parameters for the refined anatase structure are a = 3.81 Å, b = 3.81 Å and c = 8.64 Å. The crystallite sizes of the obtained catalysts 0PV/TiO_2, 0.25PV/TiO_2, 0.5PV/TiO_2 and 1PV/TiO_2 as calculated using the Scherer equation (Eq. 16) were 12.07, 10.22, 8.68 and 9.23 nm. An inverse relationship was observed between these sizes and the corresponding surface areas. The estimated sizes showed poor strain, having offered a correlation coefficient of 0.9439 when compared with those derived from Williamson-Hall data. Unlike in this study, TiO_2 of similar particle sizes prepared by a majority of workers previously, either were mostly biphasic, hierachichal macro-/mesoporous (Yu et al., 2007) or showed a redshift due to modification effects (Jaimy et al., 2011).

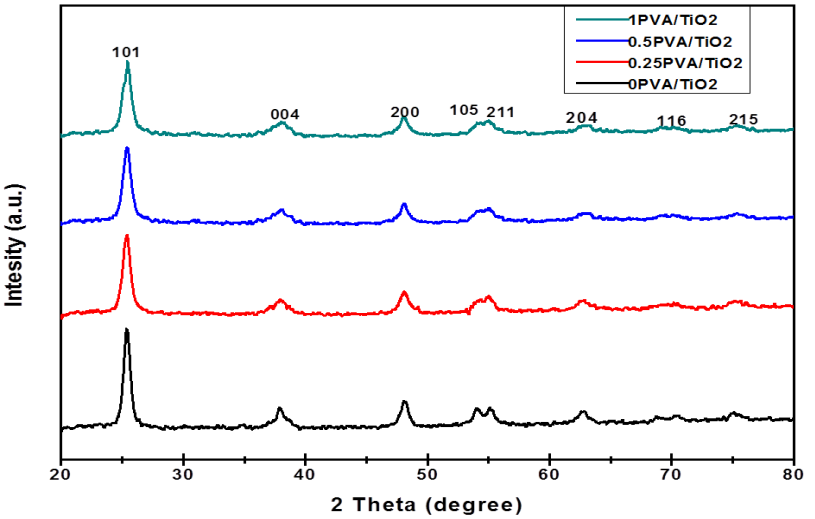

Fig. 19: *The XRD patterns of the titania prepared with and without PVA*

The morphology, structure and thickness of the catalyst particles were examined using field emission scanning electron microscope (FE-SEM) from NOVA NANOSEM 230 and a JEM-2100F transmission electron microscope (Fig. 20). The

template-free 0PV/TiO_2 (Fig. 20a) manifests as aggregate of titania crystals while 0.25PV/TiO_2 appears as a mesostructured material (Fig. 20b) with a lesser aggregation of the titania crystals. In contrast with the aforementioned, deaggregated mesostructures were obtained with the 0.5PV/TiO_2 (Fig. 20c).

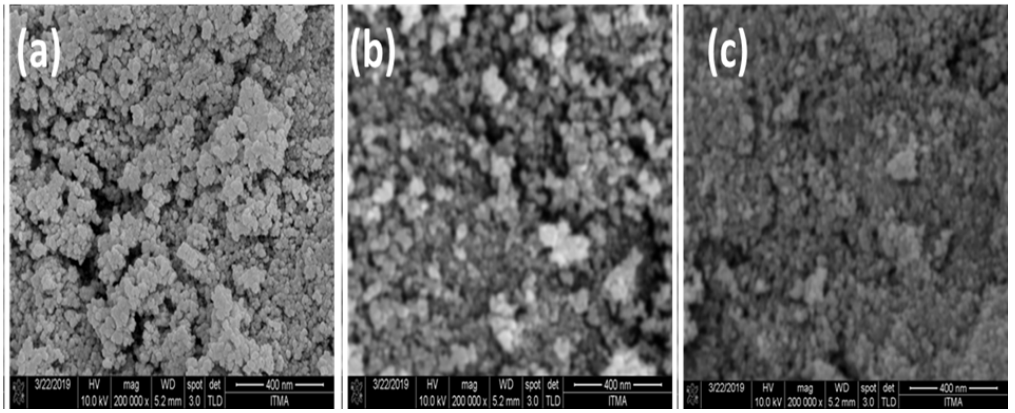

Fig. 20: *The FE-SEM of the synthesised titania. (a) 0PV/TiO_2 (b), 0.25/TiO_2 and (c) 0.5PV/TiO_2*

The TEM images and size distribution curve of the major catalyst, the 0.5PV/TiO_2, is shown in Fig. 21. The hexagonal-like shaped 2D catalyst particles are readily visualized at different magnifications. The average particle sizes of the photocatalysts were determined from the images using ImageJ software (Java 1.6.0). The 0.25PV/TiO_2 has an average size of 12.69 nm while the 0.5PV/TiO_2 is 9.49 nm. The estimated particle sizes correlate fairly well with those obtained by Scherer equation (Eq. 16). The decline in the average size of the optimal catalyst (0.5PV/TiO_2) from that of 0.25PV/TiO_2 was probably due to improved surface area and minimal deaggregation. The interplanar space of the nanodiscs is 0.323 nm (Fig. 21), which correspond to (101) crystal facets of anatase TiO_2 (Huang et al., 2013).

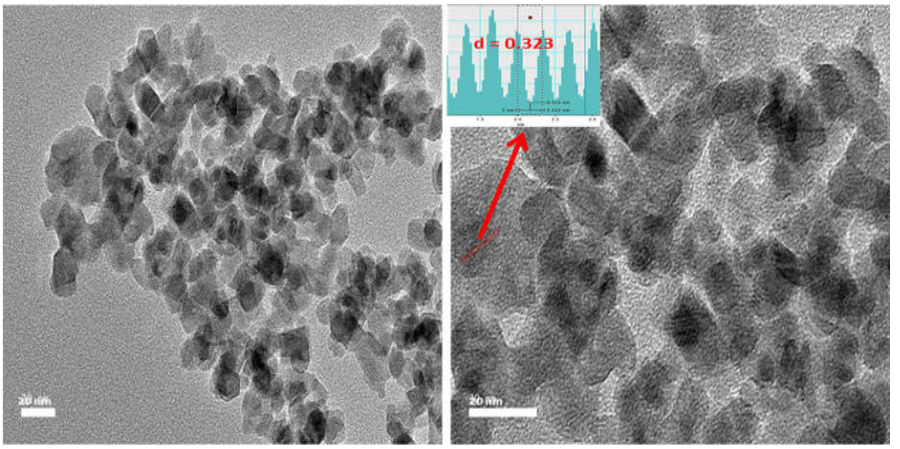

Fig. 21:*The TEM images of 0.5PV/TiO₂ at different magnifications. Scale: 20 nm*

The chemical composition of the photocatalyst was confirmed using a NOVA NANOSEM 230 FE-SEM-EDX energy dispersive x-ray (EDX) facility. Figure 22 shows the EDX spectrum of the 0.5PV/TiO_2. As may be seen from the figure, the major peaks are for Ti and O with atomic ratio 1: 0.4652 confirm the stoichiometry of TiO_2.

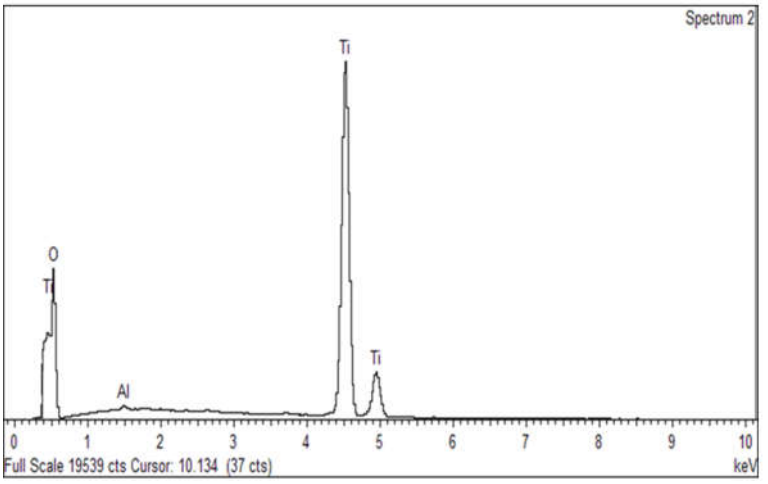

Fig. 22: *The EDX spectra of 0.5PV/TiO_2*

To determine the content of PVA template in the left in the catalyst precursor, and the stability of the prepared photocatalysts during the post-synthesis stage thermo-gravimetric analysis (TGA) was performed using a METTLER TOLEDO

TGA/DSC 1 STAR^e System, ramped at 10 ^oC/min under N_2 atmosphere. The TGA curve of 0.5PV/TiO_2 precursor is shown in Fig. 23. The first step in the thermogram is a weight loss near 100 ^oC, due to the volatile components and physically adsorbed water. This step is followed by a stepwise weight loss (*ca.* 16%) in the temperature range of 150-370 ^oC followed by another partial weight loss (*ca.* 5%) in the temperature range of 370-455 ^oC, due to the decomposition of PVA main chain into smaller parts and complete pyrolysis, respectively (Salman et al., 2019). The observation of no weight loss above 455 ^oC confirms the completion of pyrolysis, leaving behind only the stable and crystallized 0.5PV/TiO_2. Generally speaking, and in agreement with this study, PVA has been reported to decompose completely around 450 ^oC (Cui et al., 2019).

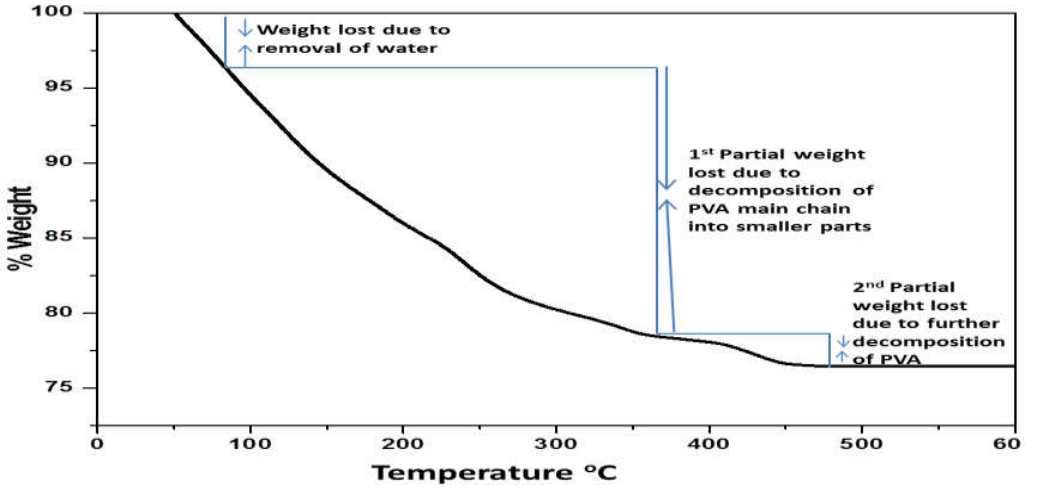

Fig. 23: *Thermogram showing the complete removal of PVA from the 0.5PV/TiO_2 precursor.*

The band gap of the catalysts was determined based on absorbance data recorded on a Shimadzu UV-3600 UV-VIS-NIR Spectrophotometer is displayed by Fig. 24. The energy edges of 0PV/TIO_2, 0.25PV/TiO_2, 0.5PV/TiO_2 and 1PV/TiO_2 were 3.04, 2.95, 2.69 and 2.87 eV, respectively indicating that increase in PVA content of the precursor (0 to 0.5g) narrows the band gap energy. These changes in absorption edge may be related to the corresponding changes in particle sizes of the synthesized materials (Bakre and Tilve, 2018; Thamapat et al., 2008). Because decreased band gap energy corresponds to more redox ability for the production of photogenerated electron-hole pairs, reduced recombination effect and higher photoresponse (Zhao et

al., 2017), the 0.5PV/TiO_2 would be expected to perform optimally.

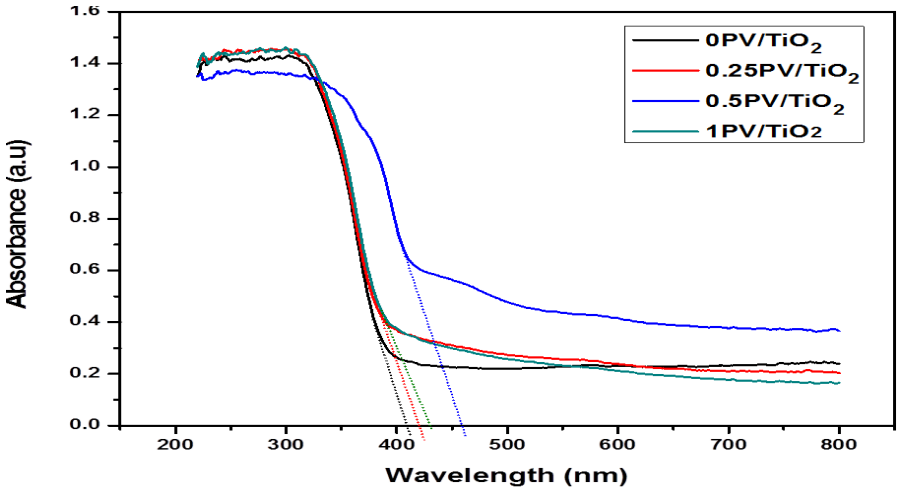

Fig. 24: *The UV–vis spectra of the precipitation-derived titanium dioxides*

The photocatalytic activity of the 0.5PV/TiO_2 was evaluated in relative terms by monitoring the percentage of degraded methyl orange in an immersion photoreactor irradiating from a 3 W China model E14 GMY UV lamp having intensity of 450 μw/cm^2 and peak wavelength of 253 nm. The optimum values of pH (2.5), nano-TiO_2 (1g/L) and initial MO concentration of (25 mg/L) were utilized in the photocatalytic experiments. A solution containing the desired amount of MO and catalyst was added to the photoreactor and pH was adjusted using NaOH and H_2SO_4. Oxygen was continuously bubbled through the mixture. Test samples were taken at intervals of time and filtered using 0.45 μm cellulose nitrate membrane. The residual concentration of MO was measured at 465.4 nm using Perkin Elmer Lambda 35 UV-Vis spectrometer. The percent degradation of the initial methyl orange concentration was calculated using Eq. (22).

$$\%Degradation = \frac{[MO]_o - [MO]_t}{[MO]} \text{ x } 100 \qquad (22)$$

Where $[MO]_o$ is the initial methyl orange concentration, $[MO]_t$ is the concentration of methyl orange at irradiation time *t*.

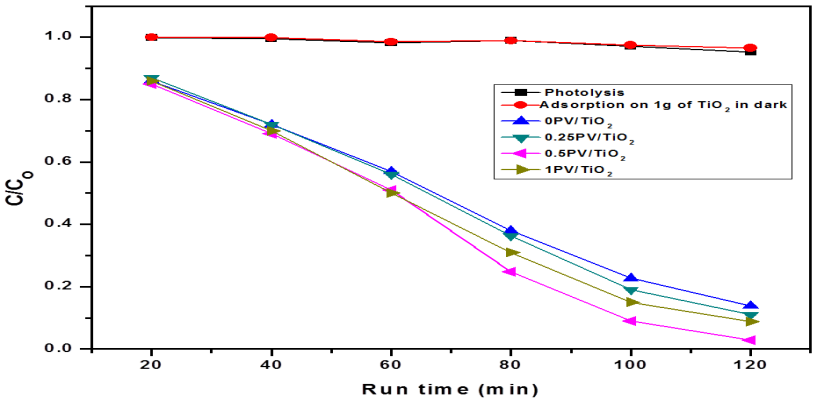

Fig. 25: *Photocatalytic degradation of MO solution (25 mg/L) in the presence of the synthesized photocatalysts (1g/L) at pH of 6.2 under 120 min UV exposure.*

In order to ascertain the superior applicability of photocatalysis for the MO degradation, photolysis, and dark adsorption experiments were performed for 2 h and compared. As shown in the Fig. 25, there is no significant disappearance of methyl orange in the event of photolysis (< 4.8 %) and adsorptive removal (3.4 %). However, there is high removal in the photocatalytic regime over 0PV/TiO_2 (86 %), and in the PVA synthesized catalysts, 0.25PV/TiO_2 (89 %) and 1PV/TiO_2 (91 %). Expectedly, the 0.5PV/TiO_2 having been derived using the optimal PVA, offered the highest catalytic performance (97.2 %). Kinetic profiles were plotted according to pseudo-zero-order and pseudo-first-order integrated rate equations. These plots were compared using the coefficient of determination (R^2) of their curves. A plot of [MO] versus *t* gave a straight line with slope = -*k* and intercept = $[MO]_o$ with R square values > 0.9, confirming the applicability of the zero-order kinetics to this study.

Lastly, as observed by some workers previously, the use of a single or binary template depends upon its efficacy to produce the required active catalyst. We have recently shown that even though 3D mesoporous titanium dioxide powders can be synthesized from chitosan and/or hexadecyltrimethylammonium bromide (HDTMA), the bi-template exhibited the relatively higher surface area (99.5 m^2/g), smaller crystal size (12.78 nm), narrower band-gap energy (2.92 eV) and highest photocatalytic rate constant (0.0112 min^{-1}) than as those from chitosan (C/TiO_2) or HDTMA (H/TiO_2) as the template (Hamisu et al., 2021).

Potentials of ZnO as Photocatalyst

The extensive use of TiO_2 may be uneconomical for large-scale water treatment. Zinc oxide has nearly the same band gap energy and follows the same photocatalytic mechanism as TiO_2. Many workers have therefore considered it as a suitable alternative to TiO_2, and even ranked it higher in photocatalytic performance. Is ZnO a reliable alternative to TiO_2?

Kinetics of Chlorophenol Removal

We started our investigations on ZnO with commercial preparations to degrade different chlorophenols: 4-chlorophenol (4CP), 2,4-dichlorophenol (24DCP) and 2,4,6-trichlorophenol (246TCP). The choice of chlorophenols was dictated by their informative photochemical reactions and severity of toxicity. They are commonly used as miticides, pesticides, herbicides, germicides, fungicides and for wood preservation. The US EPA consolidated list of chemicals contains several chlorophenols under the Emergency planning and Community Right-To-Know (EPRC) section. The 4-chlorophenol is directly relevant to environment due to its solubility and the severity of hazard to both terrestrial and aquatic life (Pohanish and Greene, 1996). Similarly, the occurrence of 2,4-dichlorophenol in open waters in China, France and Netherlands and alarming levels of 2,4,6-trichlorophenol in several rivers from different geographical regions have been reported (Chiron et al., 2007; Gao et al., 2008). Moreover, 2,4,6-trichlorophenol is likely to form as a by-product of industrial processes such as water disinfection.

The ZnO (99 % purity) was obtained from Merck. Because particle size can have a marked influence on the activity of semiconductor photocatalyst the particle size of dispersions of this material was measured on NANOPHOX at 298 K which operates within 1 nm to 10 μm range, based on the photon-cross correlation spectroscopy (PCCS). Replicate measurements were carried and average results were collected and analysed using the standard (or 2^{nd} Cumulant) method. Figure 26 shows the distribution of particle size in the ZnO powder against cumulative distribution and density distribution. From the figure, the highest cumulative distribution was obtained at 493 nm which shows that the particles are of micrometer sizes.

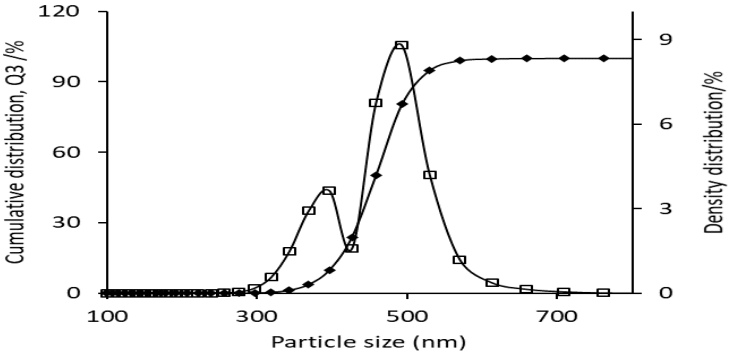

Fig. 26: *Particle size distribution of the ZnO (Merck) catalyst*

The surface area of ZnO was recorded on Sorptomatic 1990 Series analyzer following static Brunauer-Emmett-Teller (BET) nitrogen adsorption. The isotherm is (Fig. 27) reveals a non-porous material having a BET surface area of 3.28 m^2g^{-1}. We have previously shown that this low surface area is responsible for the activity of the Merck ZnO (Gaya et al., 2010). Similarly, a lower surface area (1.56 m^2 g^{-1}) was reported for Merck ZnO powder by Marto et al. (2009).

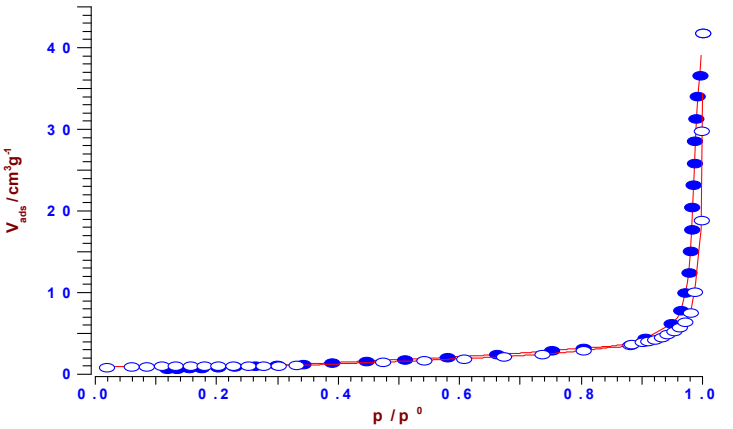

Fig. 27: *Static BET adsorption-desorption isotherm of N_2 on non-porous ZnO(Merck), recorded on Thermo Finniganm Sorptomatic 1990 Series analyser, operated at 77 K*

Band gap is very crucial to know the wavelength of light that can excite the semiconductor photocatalyst (Trikalitis et al., 2001). The reflectance of these

orderly-packed ZnO particles was measured at room temperature using a Perkin Elmer Lambda 35 UV/Vis/NIR spectrometer. The optical band gap (E_g) was estimated from the intercept of the extrapolated tangent of the plot of logarithmic remission function (lnα/S) against photon energy (hν) (Fig. 28), where α and S represent absorption and scattering coefficient, respectively. The ratio α/S was calculated from the experimentally measured reflectance (R) by the Schuster-Kubelka-Munk equation (Eq. 23) (Trikalitis et al., 2001):

$$\frac{\alpha}{S} = \frac{(1-R)^2}{2R} \qquad (23)$$

Where α/S is referred to as Kubelka-Munk or remission function and is interchangeably used with F(R). α varies with the light energy absorbed according to Tauc's equation (Eq. 10) (Kako et al., 2008).

$$\alpha h\nu \propto (h\nu - E_g)^n \quad \text{or} \quad (\alpha h\nu)^{1/n} \propto (h\nu - E_g) \qquad (24)$$

Where n is a constant for the type of optical transition. We assumed direct optical transition and remarkably effective absorption so that n = ½ and α = F(R), respectively. Ultimately, the Tauc band gap was obtained as intercept of the plot of $(\alpha h\nu)^2$ or $(F(R)h\nu)^2$ against $h\nu$. The band gap of ZnO was confirmed via the latter to be 3.36 (Fig. 28, inset) (Gaya, 2011).

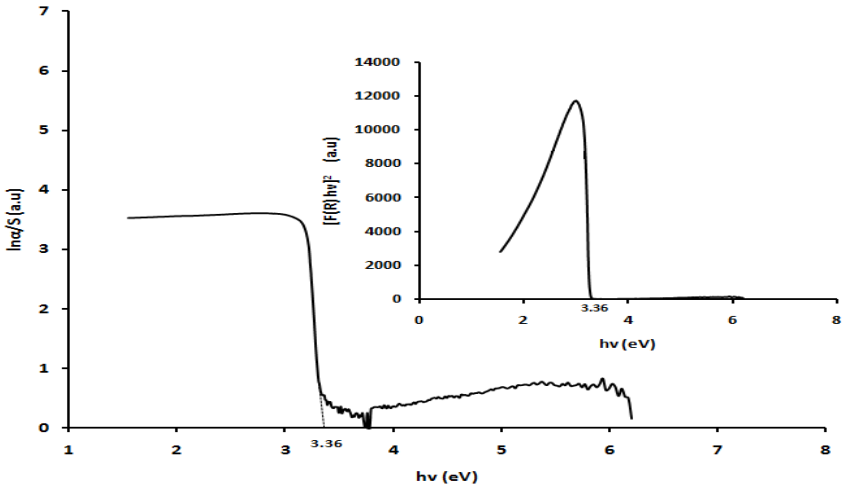

Fig. 28: *Kubelka-Munk spectral function of ZnO photocatalyst versus excitation energy. The inset is a Tauc plot depicting the variation of $(F(R)h\nu)^2$ against light photons absorbed.*

The photoreactor used in the degradation of chlorophenols over ZnO (Fig. 29) was made of 300 mm long cylindrical stainless steel, having a diameter of 80 mm and effective volume of 1.19 l. It was operated with a 6 W New York Spectronics UV lamp having maximum irradiation density at 365 nm. In a typical reactivity experiment, a solution 1litre of the chlorophenol (at a predetermined level) and ZnO photocatalyst was added to the photoreactor. Where required, pH adjustment was done using equimolar NaOH and H_2SO_4 solutions. The reactivity solution was stirred for 5 min at speed of 195 rpm to attain adsorption equilibrium before irradiation. During equilibration and photocatalytic degradation, reaction solution was constantly aerated at the rate of 2 L/min. Aliquots (20 ml) of test samples were drawn at periodic intervals of time, filtered using through 0.45 μm cellulose nitrate paper. The reaction progress was followed by measuring the concentration of chlorophenol in the samples using Shimadzu model UV-1650 PC UV-Vis spectrophotometer and by applying Eq (24).

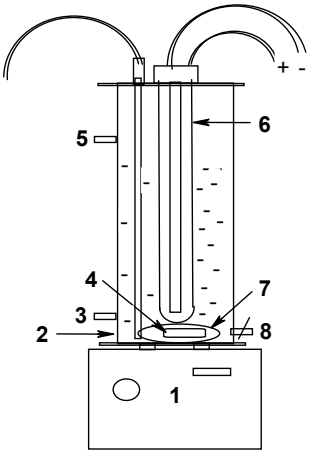

Fig. 29: *The immersion photoreactor used in the photocatalytic degradation of chlorophenols*

Legend: 1) Magnetic stirrer with speed controller, 2) Temperature controlled jacket, 3) Cooling water inlet, 4) Magnetic bar, 5) Cooling water outlet, 6) Lamp (6W UV) jacketed in quartz, (7) Air draft tube, (8) Sampling port.

Effect of Operating Parameters

The effective decontamination by photocatalysis is only achieved at optimum doses of the photocatalyst and the substrate. We therefore investigated the effect of

concentration of each of the three *p*-chlorophenols using one-factor-at-a-time (OFAT) method by varying chlorophenol concentration between 30 mg/L and 100 mg/L at a fixed ZnO load (1 g) for a period of 300 min. The results are shown in Fig. 30. A preliminary investigation with low level (10 mg/L) 4-chlorophenol and 2,4-dichlorophenol revealed high removal rate and this maintained a level performance with 30 mg/L initial concentration. At 50 mg/L the photoremoval rate began to fall probably as a result of the inadequacy of catalyst sites. This effect became more pronounced as the concentration of the phenolic substrates is increased. Similarly, the photocatalytic removal rate of 2,4,6-chlorophenol diminished between 50 mg/L and 100 mg/L initial chlorophenol concentration. As a result, 50 mg/L of each of the chlorophenols was used as initial concentration in our study.

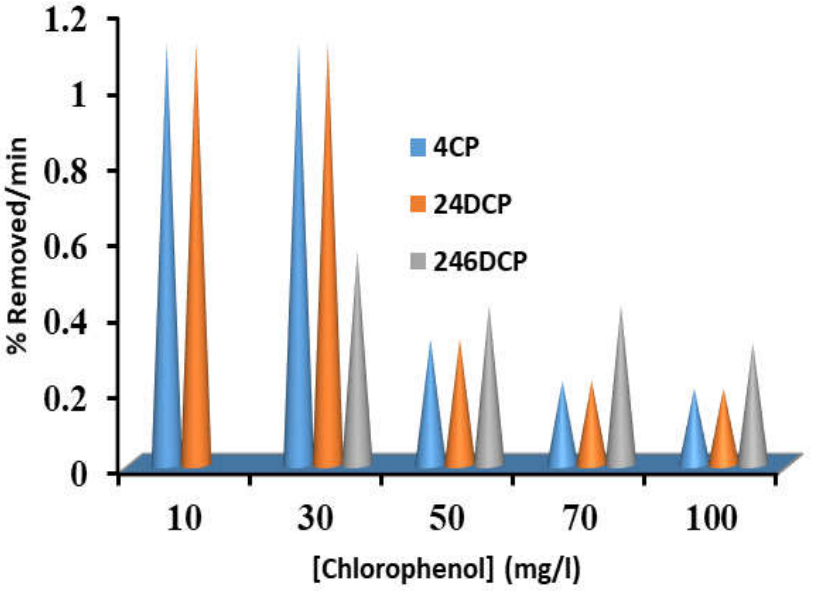

Fig. 30: *Influence of concentration on photo-oxidative removal of chlorophenols from water. Initial ZnO concentration = 1 g/L; Initial chlorophenol concentration = 30 to 100 mg/L; pH = 7.2 to 7.99*

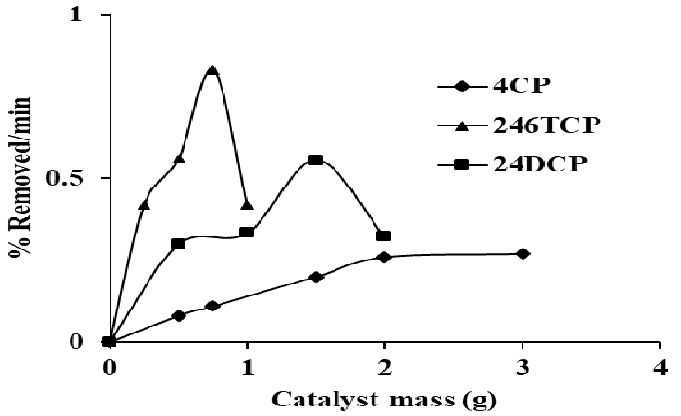

Fig. 31: *Variation of removal efficiency with catalyst dose.*

The effect of catalyst dose was investigated at the 50 mg/L chlorophenol concentration (Fig. 31). It would be observed from the figure that there is no removal of any chlorophenol in the absence of the photocatalyst. This affirms the photocatalytic nature of the process and rules out the influence of photolysis. For each of the chlorophenols there has been increase in photocatalytic removal as catalyst concentration is increased due to increasing availability of catalyst sites. It would be observed that the photocatalytic performance declined as the catalyst amount reaches 2 g/L, 1.5 g/L and 0.75/L g for 4-chlorophenol, 2,4-dichlorophenol and 2,4,6-trichlorophenol, respectively. The decrease in degradation rate would be attributed to light scattering and reduced light penetration as the catalyst is increased. Hence, these catalyst concentrations were considered optimum for our study.

In order to investigate the influence of solution acidity on photocatalytic degradation rate the effect of pH was studied. To avoid common ion effect, non Cl^- containing pH adjustment chemical was used. The degradation of all chlorophenols was favorable only in the slightly alkaline solution pH. The 4-chlorophenol showed its highest photocatalytic degradation at pH 9 whereas 2,4-dichlorophenol and 2,4,6-trichlorophenol were more degradable at pH 7. The photoprocess was inhibited further below pH 7 with all of the p-chlorophenols. For example, 4-chlorophenol did not degrade at pH 4. This is probably as a result of the stability of the molecular form of these chlorophenols as shown by Eq. (25). The reverse effect was observed at strongly alkaline solution pH.

$$PhOH(Cl)_x \underset{H^+}{\overset{OH^-}{\rightleftharpoons}} (Cl)_xPhO^- \qquad (x = 1\text{-}3) \qquad (25)$$

The photodecomposition rate of chlorophenol can be affected by the pH at point of zero charge (pH_{pzc}). The pzc is the average of the pK_a values for the first and the second dissociation in Eq. (26). A priori aqueous ZnO is largely in hydrolysed form or 'zinc-ol' as shown in Eq. (27). Since in the update by Kosmulski (2007) ZnO has been reported to possess the point of zero charge of 9, zinc-ol group would be protonated to $ZnOH_2^+$ below the pH_{pzc} or deprotonated to $Zn\text{-}O^-$ as pH_{pzc} is exceeded.

$$>ZnOH_2^+ \underset{\leftarrow}{\overset{pK_{a1}}{\rightleftharpoons}} >ZnOH \underset{\rightarrow}{\overset{pK_{a2}}{\rightleftharpoons}} >ZnO^- \qquad (26)$$

acidic pH basic pH

$$ZnO + H_2O \rightarrow \equiv Zn\text{-}OH \qquad (27)$$

For 4-chlorophenol for example, at pH 10, the negatively charged ZnO surface and the high concentration of 4-chlorophenoxide above the pK_a value of 4-chlorophenol (9.38) resulted in electrostatic repulsion which cannot be overcome by the low enthalpy possessed by ZnO active sites and this led to decreased rate. Moreover, the stability of ZnO may not be guaranteed at this high pH due to possibility of alkaline dissolution of ZnO (shown in Eq. 28). In fact, the photocatalytic rate of 4-chlorophenol degradation rate decreased above pH 9. We have authored more details of the usual four processes involved (strong repulsion, interaction, strong attraction, repulsion) in our report of Mn-doped ZnO vis-à-vis o-cresol as solution pH is varied (Abdollahi et al., 2011). For all of the *p*-chlorophenols, the photoprocess was inhibited further below pH 7. For example, 4-chlorophenol did not degrade at pH 4, probably as a result of the stability of the molecular form of these chlorophenols as shown by Eq.(25). The reverse effect was observed at strongly alkaline solution pH.

$$ZnO + H_2O + 2OH^- \rightarrow [Zn(OH)_4]^{2-} \qquad \text{(alkaline dissolution)} \qquad (28)$$

The photocatalytic oxidation of all the three *p*-chlorinated compounds on ZnO surface agreed with the pseudo zero-order rate model, expressed by Eq. (29).

$$C_t = C_o - kt \quad (29)$$

Where C_o and C_t are as the initial and final concentrations of chlorophenols, k is the pseudo zero-order rate constant and t is irradiation time. Each plot of C_t versus t gave a straight line with slope = $-k$ and intercept = C_o which confirms the applicability of the zero-order kinetics to our study. The linearity of the plots as well as the rate constants can be visualised from Table 12. The validity of the pseudo zero order model in our case could be linked to the fact that the initial concentration of substrates was high enough to occupy wholly the active sites. This information is captured in Fig. 31 which shows no availability of active sites above 50 mg/L initial ZnO concentration and was well defended in our publications (Gaya, 2011; Gaya et al., 2010b).

Table 12: *Rate constants for the pseudo zero-order disappearance of chlorophenol in ZnO suspensions.*

Chlorophenol (50 mg/L)	ZnO (g/L)	*k* (mg/L min)	R^2
4-chlorophenol	2.00	0.25	0.9978
2,4-dichlorophenol	1.50	0.38	0.9864
2,4,6-trichlorophenol	0.75	0.42	0.9637

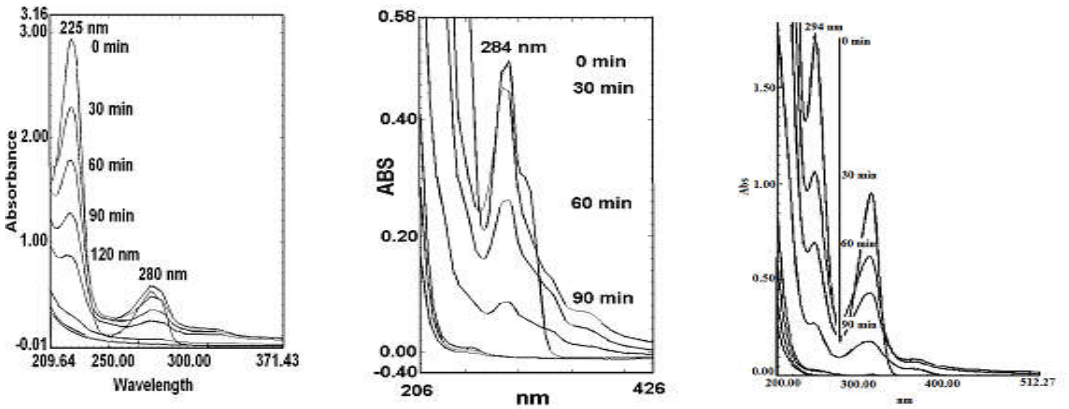

Fig. 32: *Electronic absorption spectra depicting the degradation profile of (a) 4-chlorophenol (b) 2.4-dichlorophenol. (c) 2,4,6-trichlorophenol.*

The progression of electronic spectra of chlorophenols at optimal condition is shown in Fig. 32. The UV-Vis spectra displayed two distinct bands in each case with maximum absorption at 225 nm, 284 nm and 294 nm for 4-chlorophenol (Fig. 32a), 2,4-dichlorophenol (Fig. 32b) and 2,4,6-trichlorophenol (Fig. 32c), respectively. These wavelengths were used for all UV-Vis measurements of the amounts of chlorophenols in solution. The weakening of these characteristic peak and eventual annihilation at 300 min, 180 min and 120 min, respectively, describes the extent of photocatalytic removal of these chlorophenols.

The effect of the components of the photocatalytic process namely photolysis and adsorption were evaluated at 50 mg L^{-1} chlorophenol concentration level over a period of 300 min. The results for 2,4-dichlorophenol and 2,4,6,-trichlorophenol are similar to those of 4-chlorophenol (Gaya et al., 2010a; Gaya et al., 2010b). For the 4-chlorophenol (Fig. 33) there was insignificant removal of 4-chlorophenol by photolysis and by dark adsorption, affirming that any removal over irradiated ZnO is based on photocatalysis. Even though the removal of chlorophenol by photolysis was reported by Benitez et al. (2000), these workers irradiated with a high watt (150 W) polychromatic light source.

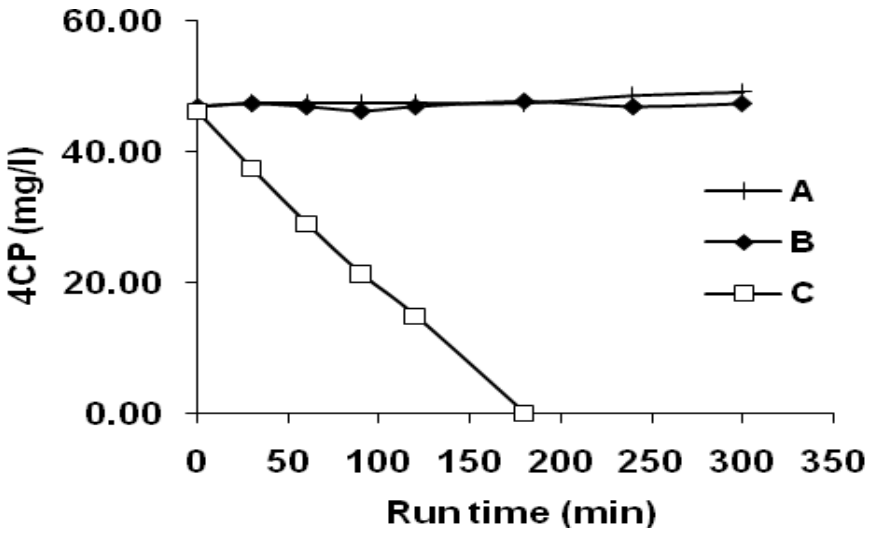

Fig. 33: *Time-course of 50 mg/L 4-chlorophenol subjected to different conditions. (A) Adsorption over 2 g of ZnO in the dark. (B) Photolysis. (C) Photocatalysis in presence of 2 g ZnO. Initial pH = 7.1-7.5*

Degradation Intermediates

The structural elucidation of degradation products during en route chlorophenols mineralisation was performed using isocratic high performance chromatography (HPLC). Waters HPLC was installed with absorbance detector and Ascentis-C_{18} column (25 cm x 4.6 mm x 5 μm). Mobile phase was continuously outgassed by using helium (He). The mobile phase delivery was optimized at 1 mL/min. Some operational parameters used for the HPLC analysis are listed in Table 13.

Table 13: *Selected parameters used in HPLC elution chromatography*

Chlorophenol	Mobile phase (v:v)	Detection wavelength	Run time
4CP	CH_3OH:H_2O (60:40)	280 nm	30 min
24DCP	CH_3CN:CH_3COOH:H_2O (69:1:30)	284 nm	20 min
246TCP	CH_3OH:CH_3COOH:H_2O (70:1:29)	280 nm	30 min

In addition, 4-chlorophenol conversion was also chromatographed on Acquity ultra performance liquid chromatograph (UPLC) fitted with Acquity BEH phenyl C_{18} column (10 cm x 2.1mm x 1.7 μm). Complementary structural elucidation of photoproducts was performed using a Shimadzu's GCMS-QP5050A Gas Chromatography-Mass Spectrometry (GC-MS). Intermediates were extracted using diethyl ether, dried over anhydrous Na_2SO_4 and concentrated to a few ml under nitrogen stream. For the GC operation, capillary column was BPX-5 (30 m x 0.25 mm x 0.25 μm) operated with helium as carrier gas. The capillary column was maintained at 70 ^oC for 2 min followed by ramping at the rate of 10 ^oC/min up to 310 ^oC. The injector and detector temperatures were fixed at 250 ^oC and 320 ^oC, respectively. The MS was operated in the full scan mode (40 to 580 m/z). The degradation data were matched with National Institute of Standards and Technology (NIST) library.

With the HPLC, several photoproducts such as hydroquinone, catechol and phenol were detected at the retention times shown in Table 14 while the GC-MS provided evidence for the occurrence of the remaining intermediates. The evolution of photoproduct in the course of 4-chlorophenol degradation is displayed by Fig. 34. We reported catechol for the first time in the photocatalytic degradation of

4-chlorophenol, while other products were also reported previously in the study of 4-chlorophenol decomposition by other advanced processes (Czaplicka, 2006; Theurich et al., 1996).

Table 14: *Photoproducts of 4-chlorophenol degradation*

***p*-Chlorophenol**	**Photoproduct**	**Retention times**		**GC-MS**
		Experiment	***Standard***	
4-chlorophenol	Hydroquinone	2.9/3.1	2.9	Detected
	Catechol	4.0	4.1	-
	Phenol	6.1	4.4	Detected
	4-chlorocatechol	9.7	-	Detected
	4-chlorophenol	15.4	15.5	128 m/z
2,4-dichlorophenol	Benzoquinone	3.2	3.2	Detected
	2-chlorohydroquinone			
	4-chlorophenol	3.9	4.1	
	hydroquinone	1.8	1.9	
	4-hydroxybenzandehyde	2.8	2.8	
	Phenol	3.4	3.5	
	3,5-dichlorocatechol	-	-	Detected
	2,4-dichlorophenol	4.7	4.2	162 m/z
2,4,6-trichlorophenol	Phenol	3.7		Detected
	3,5-dichlororocatechol	-	-	
	4-chlorophenol	5.5		
	2,4,-dichlorophenol	11.5	9.7	

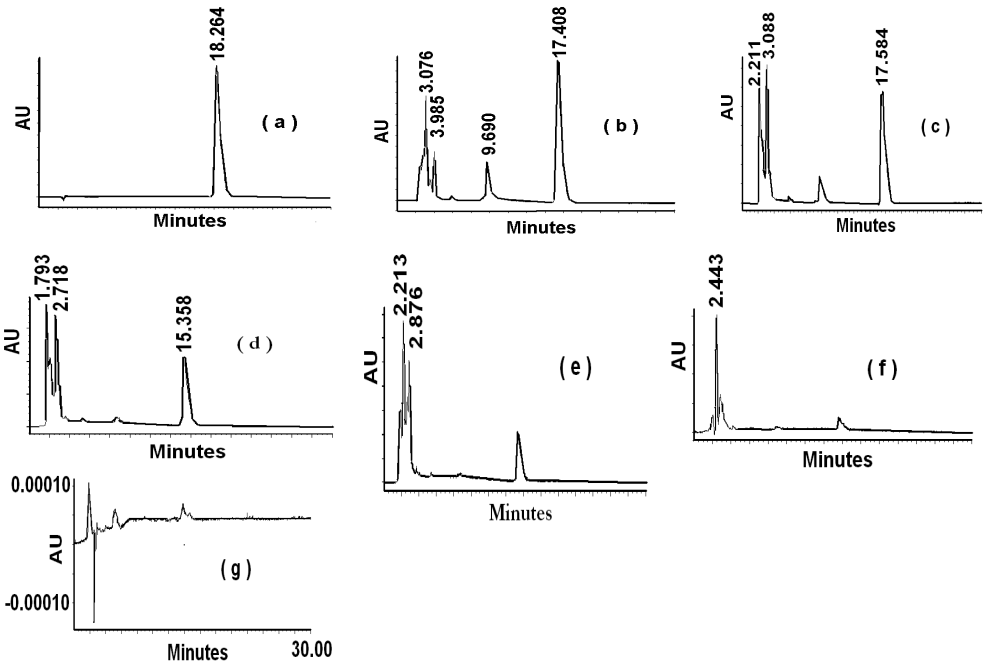

Fig. 34:; *HPLC chromatograms depicting eluted peaks at different reaction times (a) 0 min (b) 30 min (c) 60 min (d) 90 min (e) 120 min (f) 180 min (g) 240 min. Initial conditions: 50 mg/L 4CP; 2 g ZnO; pH 7.5*

The depletion of 4-chlorophenol is further revealed by the time course plot of % peak area recorded on UPLC for the mineralisation of 70 mg/L 4-chlorophenol (Fig 35a). The 4-chlorophenol mineralisation of was confirmed by inspection of HPLC peaks recorded at optimum operating conditions. The maximum levels of these compounds were attained in 30 min to 60 min. The initial growth of products and decay of 4-chlorophenol peak can be seen from sample chromatograms in Fig. 35(b). The maximum concentration of hydroquinone and 4-chlorocatechol were 32% and 15%. After 3 hours, 4-chlorophenol and intermediates have been completely eliminated.

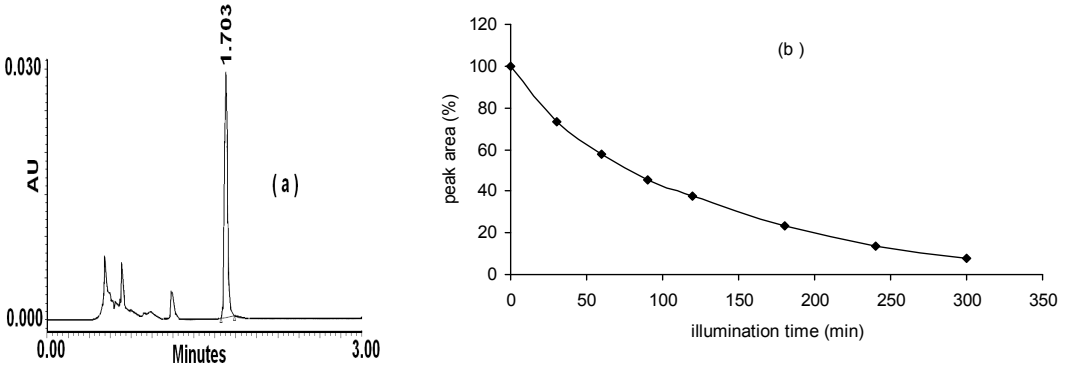

Fig. 35: *(a) Chromatograms from UPLC showing the 4-chlorophenol peak (major), and intermediate products. (b) Changes in peak area as a function of time recorded on UPLC during the photomineralisation process. Initial conditions: 70 mg/L 4-chlorophenol, 1g ZnO*

Accordingly, the emergence of stable organic intermediates in the ZnO photocatalysis of 2,4-dichlorophenol were chromatographed with time. We have selected for this discussion two of the chromatograms. Figure 36 shows the retention peaks of these phoroproducts after 60 min and 90 min. Benzoquinone, 4-hydoxybenzaldehyde and 4-chlorophenol eluted at 3.2, 2.8 and 3.9 after 60 min of irradiation, respectively. After 90 min we detected phenol and 4-chlorophenol which means the degradation proceeds through the scission of ring-Cl bond.

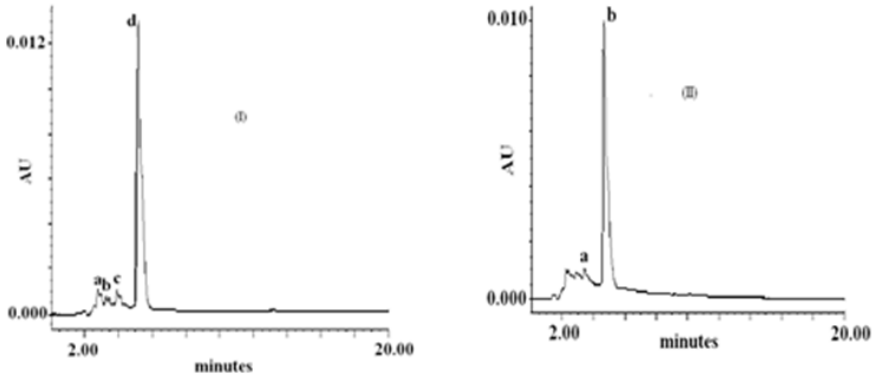

Fig. 36: *Chromatograms of 2,4-dichlorophenol.* ***(I)*** *60 min of irradiation: (a) 4-hydroxybenzaldehyde/catechol b) p-benzoquinone c) 4-chlorophenol d) 2,4-dichlorophenol;* ***(II)*** *90 min of irradiation: a) phenol b) 2,4-dichlorophenol*

The chromatographic analysis of 2,4,6-trichlorophenol was performed in a similar manner to that of 2,4-dichlorophenol and the chromatograms at 45 min, 60 min and 120 min are displayed by Fig. 37. Both the 2,4-chlorophenol and 2,4,6-trichlorophenol produced 3,5-dichlorocatechol, and 4-chlorophenol (a lower chlorophenol) while all the chlorophenols studied produced phenol en route degradation.

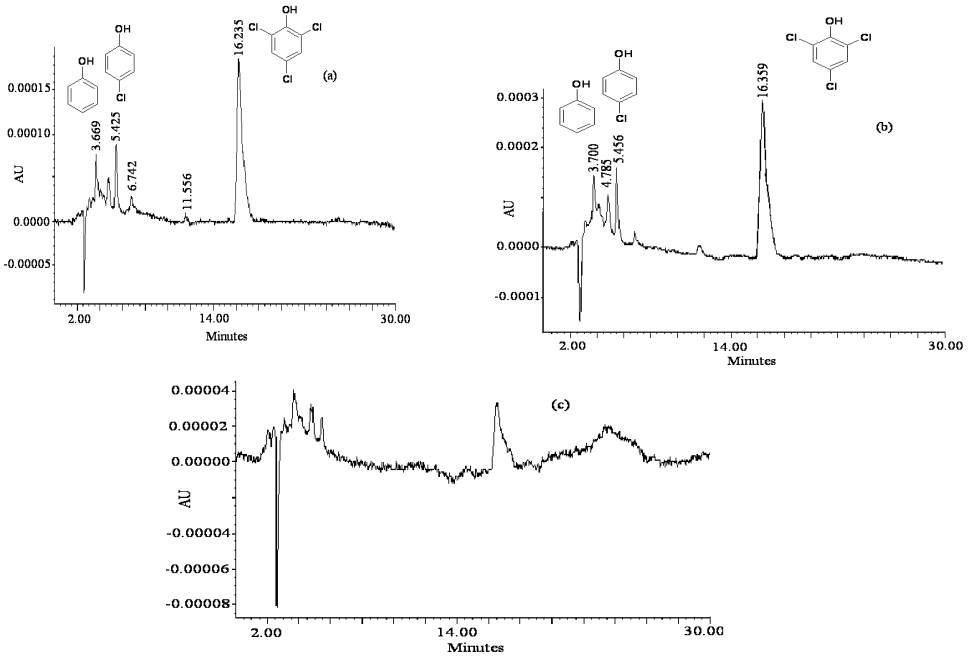

Fig. 37: *Chromatographic peaks of 246TCP and intermediates en route to mineralisation (a) 45 min (b) 60 min (c) 120 min. Initial conditions: 50 mg L^{-1} 246TCP; 0.75 g ZnO; pH 6.98*

Reaction Mechanism

The details of the reactions of the intermediates we disclosed along the photocatalytic decomposition of 4-chlorophenol, 2,4-dichlorophenol and 2,4,6-trichlorophenol are available in our reference papers (Gaya et al., 2009; Gaya et al., 2010a; Gaya et al., 2010b). On this basis, we proposed a general mechanism to account for the formation of these intermediates (Fig. 38) (Gaya, 2011). Generally, the detected intermediates are mostly hydroxylated, dehydroxylated or dechlorinated intermediate products thus falling into higher or lower molecular weight aromatics. The formation of these intermediates can be attributed to the oxidative action of hydroxyl radical (Theurich et al., 1996) which herein manifests as oxidative scission and/or hydroxylation. It would be seen from the figure that 2,4,6-trichlorophenol yielded 3,5-dichlorocatechol by dechlorination and hydroxylation. By the same process, 2-chlorohydroquinone or 4-chlorocatechol could be formed from 2,4-dichlorophenol. Similarly, the hydroxylation of 4CP will yield the same products. Perhaps phenol is the last phenolic formed in the transformation of chlorophenols.

Several literature (Theurich et al., 1996; Li et al., 1999) have shown that hydroquinones and subsequently benzoquinones are formed by tautomerism which would decompose to aliphatics and finally carbon dioxide and water. In this connection, we have also detected hydroquinone and benzoquinone during 4-chlorophenol and 2,4-dichlorophenol degradation, respectively.

One thing to ponder about is the effect of increasing ring-Cl on the conversion efficiency of the chlorophenols. We obtained the order of degradability of these phenolic congeners based on rate constant as 4-chlorophenol (k = 0.25 mg L^{-1} min^{-1}) < 2,4-dichlorophenol (k = 0.38 mg L^{-1} min^{-1}) < 2,4,6-trichlorophenol (k = 0.42 mg L^{-1} min^{-1}). The ease of transformation as the number of ring-Cl bonds is increased indicates the absence of steric hindrance to the attack of OH radical. However this opinion may not be conclusive since two other *p*-diclorophenols and *p*-trichlorophenols have not been investigated.

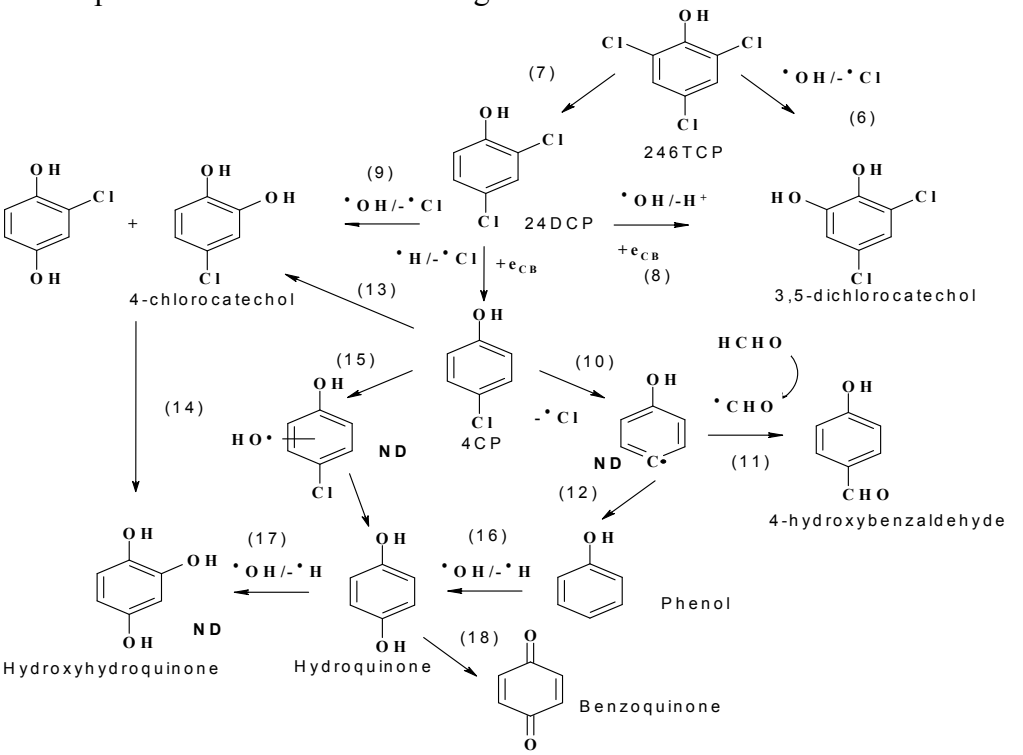

Fig. 38: *Tentative general mechanism for the degradation of 4-chlorophenol, 2,4-dichlorophenol and 2,4,6-trichlorophenol*

We attempted for the first time to study the role of directing groups on the incoming hydroxyl radical in photocatalytic oxidation products of *p*-chlorophenols. All the ring oxidation products determined in our study are lower or higher molecular weight phenolics with exception of benzoquinone, a non-aromatic organic. The higher molecular weight oxidation products of the chlorophenols are products of ortho-hydroxylation due to the resistance of ring-Cl bond at the para-positions. We can categorically state that the ortho-para directing effect of the phenolic –OH is ab initio stronger than that of the ring-Cl. The higher molecular weight 3,5-dichlorocatechol as well as 4-chlorocatechol can be said to form predominantly by the ortho-hydroxylation of 2,4-dichlorophenol and 4-chlorophenol, respectively. This observation is supported by the yields of photoproducts reported by Sehili and co-workers in the case of monochlorophenols and 2,4-dichlorophenol (Sehili et al., 1989; Sehili et al., 1991). These workers reported low yield (0.1 %) for 2,4-dichlororesorcinol in contrast to 10.9 % for 3,5-dichlorocatechol, which rules out the prevalence of the influence of –Cl directing group.

In this study, we determined both phenol and hydroquinone as intermediates of chlorophenol decomposition. Since hydroquinone is a common intermediate of phenol decomposition (Zhang et al., 2006), the presence of both compounds during the oxidation of 4-chlorophenol and 2,4-dichlorophenol in our work is an evidence for the para-directing effect of the phenolic–OH. We obtained a much lower yield of catechol (8 %) compared to that of hydroquinone (32 %) and 4-chlorocatechol (15 %) during 4-chlorophenol transformation as shown in Fig. 39, which implies that the vacant *p*-position of phenol is preferentially hydroxylated by hydroxyl radicals.

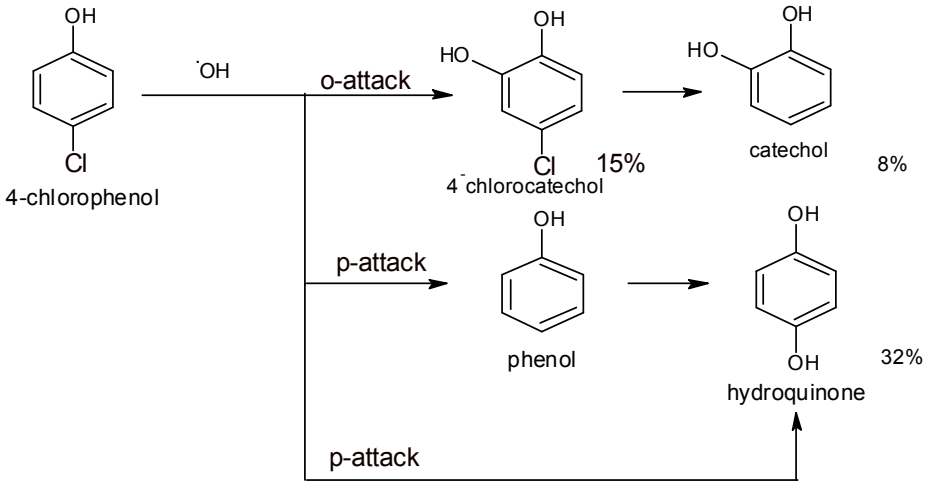

Fig. 39: *Mechanistic scheme showing preferential p-attack during 4-chlorophenol transformation*

Activity and Stability of ZnO

Aside from Merck, two other commercial ZnO powders were evaluated for activity for chlorophenol removal. The comparison was based on physical characteristics such as band gap, and initial throughput of the photoreaction. This time the band gap was determined using the energy-wavelength relationship (Eq. 30).

$$E(eV) = \frac{1240}{\lambda} \qquad (30)$$

Table 15 shows the initial rate of phenolic degradation on the ZnO powders. It can be observed that ZnO from Merck has the highest photoactivity for chlorophenol degradation. In addition, from the initial rates of photoremoval in the table it can be concluded that 4-chlorophenol is the most resistant among the *p*-chlorophenols used in the study having consumed more amount of the catalyst despite its activity.

Table 15: *Activity of different ZnO powders for chlorophenol removal*

ZnO Brand	Physical Property			Initial rate x10^{-2} (mg/L min)		
	E_g (eV)	S_{BET} (m^2 g^{-1})	Particle size* (μm)	4CP	24DCP	246TCP
Alfa Aesar	3.04	1.46	0.04-0.25 (±0.0)*	15	23	23
Merck	3.02	3.28	0.39-0.51 (±0.0)*	25	38	40
PC lab	3.07	2.33	0.12-0.56 (±0.0)*	15	24	22

Note: * Error limits are standard deviation.

The photoactivity of Merck ZnO could perhaps be explained as follows. Surface area and photoactivity in these ZnO powders decreased in the order Merck < PC lab < Alfa Aesar. Since the band gap of these oxides is nearly the same, it can be concluded that surface area plays a very important role on the activity of these ZnO powders for chlorophenol removal. Unexpectedly, there is no obvious correlation between the activity of ZnO and particle size. Thus though the particles of Alfa Aesar ZnO (Table 15) were in smaller sizes, they showed lower efficiency than the Merck powder. This may be linked to the agglomeration of particles evident from its morphology as shown by Fig 37. Conversely, the Merck ZnO shown orderly arranged hexagonal particles with no agglomeration.

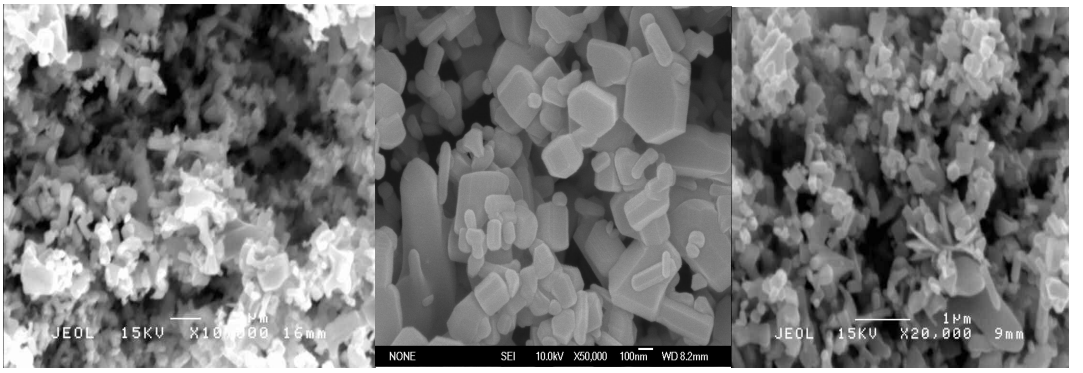

(a) **(b)** **(c)**

Fig. 37: *Scanning electron images of ZnO. (a) Alfa Aesar, (b) Merck, (c) PC lab*

In recognition of the propensity of ZnO for dissolution or photocorrosion in illuminated solutions we studied the amount of zinc ion left in the decontaminated water using inductively coupled plasma optical emission spectroscopy (ICP-OES) with a Perkin Elmer Optima 200 DV optical emission spectrometer. Standard solutions bracketing the Zn^{2+} content of samples were prepared and run at the same time as the catalyst-free samples. Zinc oxide was mostly stable (dissolved $Zn^{2+}<$ 0.02) and does not increase appreciably with irradiation time. Specifically, the % Zn^{2+} dissolved from 24 samples was within the range of 0.001 to 0.016 with 0.0075 ± 0.005 at pH 7.54 ± 0.17 natural pH. Only about 0.01 $\pm$ 0.005% of Zn^{2+} was lost at optimal 4-chlorophenol degradation conditions. This dissolution increased with chlorophenol concentration (or acidity) which may be attributed to further ZnO dissolution, since more light can pass through and solubility is quatitatively favoured as represented by Eq. (31).

$$ZnO + 2H^+ \rightarrow Zn^{2+} + H_2O \text{ (acidic dissolution)} \qquad (31)$$

Effect of Inorganic Anions

As real waters usually contain inorganic ions coexisting with organic pollutants, the effect of inorganic anions (HPO_4^{2-}, SO_4^{2-}, Cl^- and $S_2O_8^{2-}$) on reaction rate was investigated at levels of 0.4 mg L^{-1} and pH 7. The photoremoval rate was enhanced by the presence of inorganic anions in the order Cl^- (74%) < SO_4^{2-} (96%), $S_2O_8^{2-}$ (96%) as opposed to 71% in anion-free 4-chlorophenol medium. The photocatalytic reaction was totally inhibited by HPO_4^{2-} due to strong binding of the anion to the active sites thereby preventing any other adsorption. The effect of presence of the above inorganic anions on 2,4-dichlorophenol and 2,4,6-trichlorophenol removal rate was accordingly studied. The results are displayed in Fig 38. In both cases HPO_4^{2-} showed the highest inhibition, which corroborates the findings of Doong et al, (2001) and Ravichandran et al. (2007) in the photodegradation of monochlorophenol over TiO_2 and photodefluoridation of pentafluorobenzoic acid in ZnO suspensions, respectively.

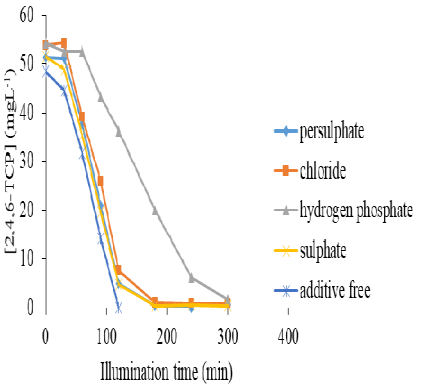

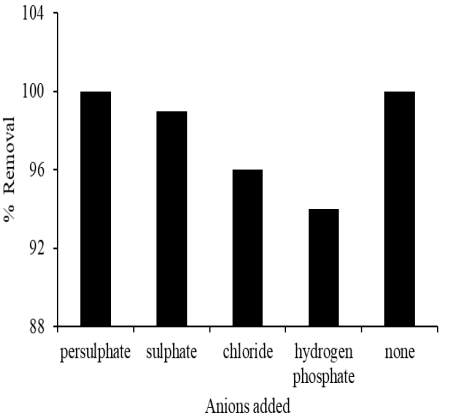

(a) **(b)**

Fig. 38: *The influence of anions on photocatalytic removal rate. (a) 2,4-dichlorophenol (50 mg/L) in 1.5 g/L at pH = 7. (b) 2,4,6-trichlorophenol (50 mg/L) in 0.75 g/L ZnO*

Basically, the enhancement of decomposition rate by sulphate and peroxodisulphate ions may be linked to the direct or indirect formation of $SO_4^{\bullet-}$ chemically shown by Eq.(32) to (34). Previous literature has shown that this in-situ generated radical can sufficiently act as strong oxidising agent or initiate the formation of hydroxyl radical (Ravichandran, 2007).

$$S_2O_8^{2-} + e^-_{CB} \rightarrow SO_4^{2-} + SO_4^{\bullet-} \quad (32)$$

$$SO_4^{2-} + h^+ \rightarrow SO_4^{\bullet-} \quad (33)$$

$$SO_4^{\bullet-} + H_2O \rightarrow SO_4^{2-} + {}^{\bullet}OH + H^+ \quad (34)$$

Chloride ion can show inhibitive effect in acidic pH, as it adsorbs strongly onto the surface of the semiconductor particles (Wang et al., 1999). This effect was not observed because our initial working environment was neutral. In any case, the enhancement of decomposition rate by Cl^- and SO_4^{2-} will be most welcome as they are among the commonest anions in open waters. In line with our results, Lair et al. (2008) reported increase in photocatalytic oxidation rate of naphthalene degradation by Cl^- ions.

Rates of Mineralisation of Benzoquinone

Even though benzoquinone has been reported as an intermediate of the photocatalytic degradation of aromatic compounds, the case of 1,4-benzoquinone individually as potential pollutant has not yet been paid much attention. Prior to our work (Abdollahi et al., 2012), only 14 % of the starting benzoquinone was slowly mineralized over TiO_2 in 240 min while the rest was converted to intermediates, mainly hydroquinone (Sobczyński et al., 1999).

We investigated the ZnO destruction of 1,4-benzoquinone (1,4-BQ) under UV irradiation in a batch reactor, and evaluated the extent of mineralisation using ANATOC Series II Total Organic Carbon Analyzer. Figure 39 shows the total organic carbon (TOC) and the total inorganic carbon (TIC) concentrations during 1,4-BQ degradation. It would be seen that the amount of TOC steadily decreased with increasing irradiation time, which indicates the disappearance of 1,4-BQ intermediates. On the other hand, the TIC curve shows that the amount of total inorganic carbon was relatively constant.

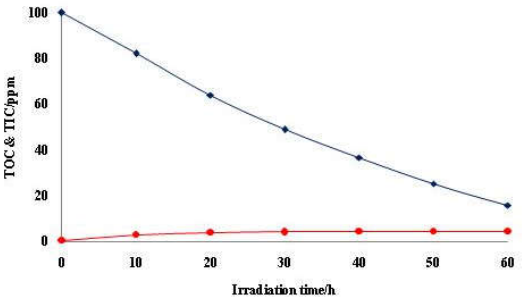

Fig. 39: *Time course of TOC and TIC during photodegradation of 1,4-BQ, (♦) TOC, (●) TIC. Initial conditions: 1,4-BQ concentration = 100 mg L^{-1}, ZnO = 1.0 g L^{-1} and pH = 7.55*

The presence of inorganic carbon is most likely due to the conversion of some organic carbon into inorganic carbon, such as carbonate ions. From the figure, 84 % organic carbon is removed from 1,4-BQ solution as CO_2 which includes the hydroquinone we detected by GC-MS at earlier irradiation times. The residual TOC value (16 %) would perhaps indicate the presence of unidentified photoproducts such as aliphatic carboxylic acids, at the end of the reaction.

Box-Behnken Optimised Degradation of Crystal Violet

It was estimated that about 15% of the total dyes produced were estimated to be lost during the dyeing processes and released into the environment as textile effluent (Bessekhouard et al. 2004). Synthetic dyes (triphenylmethane, azo or anthraquinone) are generally recalcitrant in the environment. Basic triphenylmethane dyes, have $(C_6H_5)_3CH$ aromatic framework, and synthetic origins, and are highly resistant to biodegradation (Godlewska et al., 2014). They are brilliant, intense coloured, highly colourfast which makes them useful in textile industry to provide vibrant bright colours to wool, silk, polyamide, food, cosmetics, waxes, paper, leather and plastics.

The photocatalytic removal of reactive orange 5, an azo dye, in presence of MgO nanopowder recorded 90% efficiency after much of irradiation (24 h) (Kamel et al., 2013). A few years back, a composite of CeO_2-ZnO showed remarkable photocatalytic performance in the degradation of crystal violet with rate constant of 0.0125 min^{-1} under UV irradiation (Zahoor et al. 2018). We therefore performed the photocatalysis of crystal violet (CV), a member of toxic, environmentally-ubiquitous, using an impregnation-based 1 wt % MgO-ZnO nanocomposite, to see the effect of little MgO instead of CeO_2 (Umar and Gaya, 2019). The band gap energy of this catalyst (3.22 eV) was estimated using Perkin Elmer Lambda 35 UV–Vis spectrometer using the Tauc's relation. The average size of the crystallites and the structure of the as-synthesized catalyst were analyzed using an X'Pert Pro (Philips) diffractometer in the 2θ range of 20-120°.

The XRD patterns of as-synthesized 1 wt% MgO doped ZnO nano-particles are shown in Fig. 40. The XRD patterns shows peaks at the diffraction angles (and reflections) of = 32.8 (100), 34.64 (002), 36.5 (101), 47.47 (102), 56.76 (110), 63.08 (103), 68.01 (200) and 68.29 (112) corresponding to hexagonal wurtzite ZnO (JCPD card 36-1451) (Zheng et al., 2007; Yu & Yu, 2008). The diffraction angle 42.88° is characteristic of MgO ((JCPDS file 01-072-0447). By using Debye-Scherer equation (Eq. 16), the average particle size of the composite was calculated to be 34 nm. The extreme sharpness of the diffraction peaks in Fig. 40 are evidences of the high crystallinity of the nanocomposite particles.

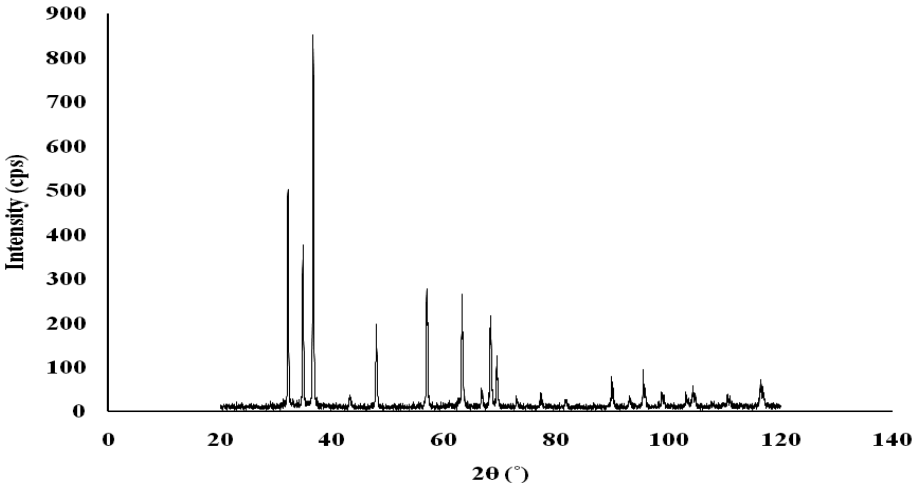

Fig. 40: *The XRD patterns of the synthesized 1wt%MgO doped ZnO catalyst*

The batch experiments for the removal of crystal violet were carried out in a reactor previously described (Yusuf & Gaya, 2018), according to Box-Behnken design. The operating factors were the initial CV concentration (A), catalyst dose (B) and pH (C) varied through three levels as shown in Table 16. Fifteen experiments were performed based on these input variables under irradiation with a 100 W UV lamp over a period 180 min. Absorbance of samples was measured at 380 nm using Perkin Elmer version lambda 35 UV Vis spectrophotometer. The percent dye degradation ($\%D_{exp}$) was calculated in a similar manner to Eq. 22 and these processed using Design Expert version 10 to obtain statistically valid predicted percent degradation values ($\%D_{pred}$).

Table 16: *Input factors and levels used in the study*

Factors	**Levels (and codes)**		
A-CV concentration (mg/L)	10 (-1)	20(0)	30(+1)
B- 1wt% of MgO-ZnO (g/L)	0.1(-1)	0.3(0)	0.5(+1)
C-pH	3(-1)	8(0)	11(+1)

The % D_{exp} and the statistically predicted % D_{pred} are shown in Table 17. As seen from the table, there is great consistence between the experimental and the predicted degradation efficiencies. The optimum conditions of the study were 10 mg/L initial

crystal violet concentration, 0.1 g/L catalyst concentration and pH 8, in which 94.6% degradation was achieved.

The predicted relationship between the degradation efficiency of crystal violet (% D) under the influence of initial crystal violet concentration (A), catalyst concentration (B) and pH (C) was quadratically-described by Eq. 35.

$$\%D_{pred} = 92.56 - 3.84A - 0.70B + 1.14C - 2.58A^2 - 2.98C^2 \quad (35)$$

The adequacy of this model has been justified by the analysis of variance (ANOVA) in Table 3 which shows $p<0.0001$, an insignificant lack of fit (LOF = 0.61), and F-value of 329.71 (a 0.01% chance of the value being due to noise). All the model terms (A, B, C, A^2, C^2) are significant. The analysis also showed a reasonable agreement of the Pred R-Squared value (0.9849) with the Adj R-Squared value (0.9904).

Table 17: The Box-Behnken efficiencies of crystal violet removal.

S/No.	A: [CV] (mg/L)	B: 1wt% of MgO-ZnO (g/L)	C: pH	D_{exp}(%)	D_{pred}(%)
1	20(0.00)	0.5(1.00)	3(-1.00)	88.0	87.74
2	20(0.00)	0.3(0.00)	8(0.00)	92.8	92.56
3	30(1.00)	0.3(0.00)	3(-1.00)	81.9	82.02
4	30(1.00)	0.5(1.00)	8(0.00)	85.0	85.44
5	20(0.00)	0.1(-1.00)	3(-1.00)	89.0	89.14
6	20(0.00)	0.5(1.00)	11(1.00)	90.0	90.02
7	30(1.00)	0.3(0.00)	11(1.00)	84.7	84.30
8	20(0.00)	0.3(0.00)	8(0.00)	91.9	92.56
9	30(1.00)	0.1(-1.00)	8(0.00)	87.0	86.82
10	10(-1.00)	0.3(0.00)	3(-1.00)	89.7	89.70
11	20(0.00)	0.3(0.00)	8(0.00)	92.8	92.56
12	20(0.00)	0.1(-1.00)	11(1.00)	91.0	91.42
13	10(-1.00)	0.5(1.00)	8(0.00)	93.0	93.12
14	20(0.00)	0.3(0.00)	8(0.00)	92.8	92.56
15	10(-1.00)	0.3(0.00)	11(1.00)	92.0	91.97
16	20(0.00)	0.00	8(0.00)	92.8	92.56
17	10(-1.00)	-1.00	8(0.00)	94.6	94.52

Table 18: *ANOVA for Response Surface Quadratic Model*

Source	Sum of Squares	Degree of freedom	Mean square	F-value	Prob > F	Remark
Model	201.52	5	40.30	329.71	< 0.0001	Significant
A	117.81	1	117.81	963.71	< 0.0001	
B	3.92	1	3.92	32.07	0.0001	
C	10.35	1	10.35	84.68	< 0.0001	
A^2	28.11	1	28011	229.97	< 0.0001	
C^2	37.50	1	37.50	306.79	< 0.0001	
Residual	1.34	11	0.12			
Lack of Fit	0.70	7	0.100	0.61	0.7311	Not significant
Pure Error	0.65	4	0.16			
Cor Total	202.86	16				

The response surface plots showing effect of parameters are shown in Fig. 41. Figure 41a shows low degradation efficiencies at high initial crystal violet concentration and pH. Accordingly, the 3D plot (Fig. 41b) of catalyst doses vis-à-vis crystal violet concentration shows high degradation efficiencies only as these parameters are lowered.

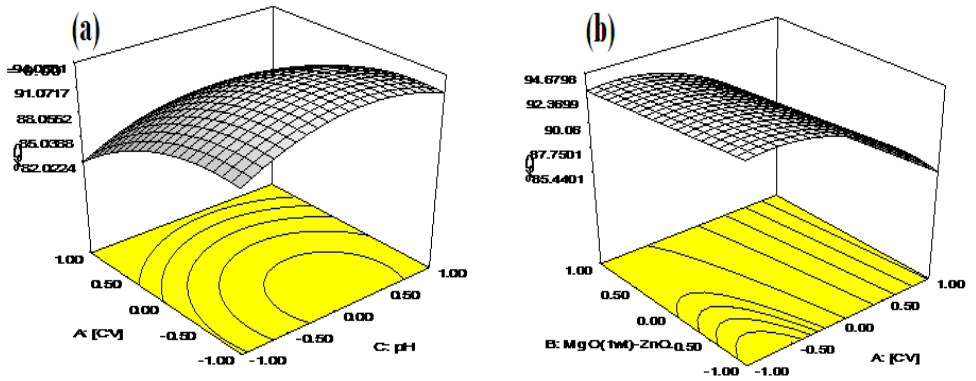

Fig. 41: *Response plots showing the interaction of crystal violet concentration with (a) pH, (b) catalyst*

Langmuir-Hinshelwood Kinetics

The Langmuir-Hinshelwood rate expression usually holds for heterogeneous photocatalytic degradation rate and the initial pollutant concentration. Basically, the rate of removal of CV may be given by equation (Eq. 36).

$$r = -\frac{d[\mathrm{CV}]}{dt} = \frac{k_r k_e[\mathrm{CV}]}{1 + k_e[\mathrm{CV}]} \tag{36}$$

Where k_r is the reaction rate constant (mg/L.min) and k_e is the adsorption coefficient of the CV onto the photocatalyst particle (L/mg). At low CV concentration, the rate of photo-reaction can be simplified to an apparent first-order equation (Eq. 37).

$$-\frac{d[\mathrm{CV}]}{dt} = k_r k_e[\mathrm{CV}] \tag{37}$$

Let $k_{app}=k_r k_e$, so that Eq. 37 yields the differential rate of CV degradation (Eq. 38).

$$-\frac{d[\mathrm{CV}]}{dt} = k_{app}[\mathrm{CV}] \tag{38}$$

Where the k_{app} is the apparent pseudo-first-order constant equation 39 is the integrated version of Eq. 38.

$$\ln\frac{\mathrm{C_o}}{\mathrm{C_t}} = k_{app}\mathrm{t} \tag{39}$$

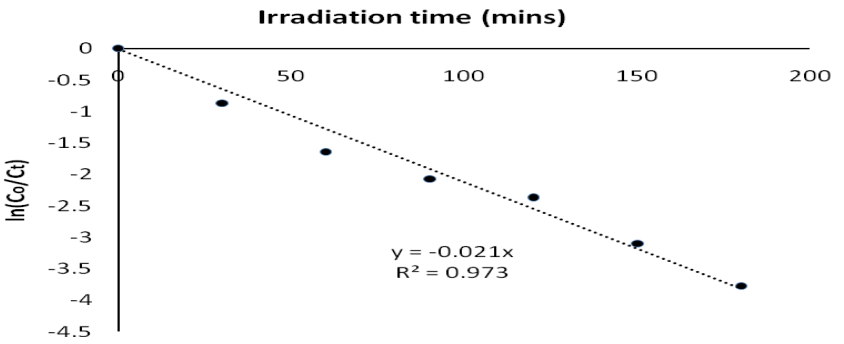

Fig. 42: *Langmuir-Hinshelwood plot of CV degradation in 1wt%MgO-ZnO*

In this study, experimental results at optimum conditions (Fig. 42) indicated a reasonable agreement of the photodegradation rate of CV in presence of 1%MgO-ZnO ($R^2 = 0.973$) with the linear form of the Langmuir-Hinshelwood (L-H) kinetics. The k_{app} realized (0.021 min^{-1}) is much higher than that of the photocatalytic degradation of reactive red 4 over TiO_2 immobilized on glass (0.002 min^{-1}) but less than the performance of TiO_2/chitosan layer immobilized on glass (0.064 min^{-1}) (Nawi & Sheilatina, 2012) due to the remarkable synergistic effect of the hybrid photocatalysis-adsorption process delivered by this layer.

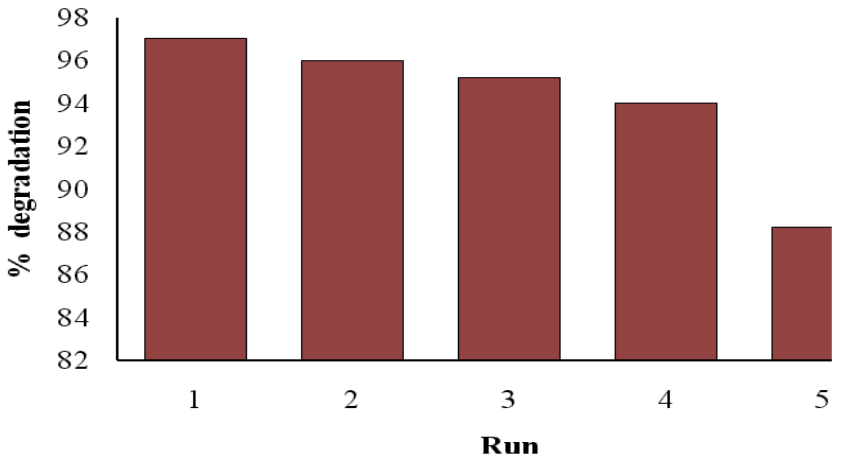

Fig. 43: *Plot showing reusability of 1% MgO doped ZnO in crystal violet degradation*

To make the synthesised catalyst attractive to full-scale application, reusability was assessed for five cycles, at optimized conditions obtained from the Box-behnken design (10 mg/L crystal violet, 0.1 g/L catalyst and pH 8). After each run, the photocatalyst was recovered, washed with deionized water to remove the adsorbed crystal violet dye molecules. The photocatalyst was then reactivated by calcination at 300 ^oC in a furnace for 2 h, for the next cycle. The results in Fig. 43 showed that the fresh catalyst (with 97 % removal efficiency) can be reused for four consecutive runs with at least 94 % removal. At the fifth cycle, the % CV removal was only 88 % possibly due to fouling (Chakrabarti & Dutta, 2004) or photocorrosion with long time irradiation (Zhang et al., 2009). The least performance obtained in this stability study is similar and in some cycles better than that of TiO_2 in presence of methyl orange dye solutions (Carcel et al., 2012).

Alkanolysis of Lipids to Biodiesel

Concerns over the hike, non-renewability, unfriendliness, and non-biodegradable nature of crude oil products have now necessitated an intensive search for alternative fuels such as the long-chain fatty acid methyl esters (known popularly as biodiesel). Transesterification can conveniently yield this material from the reaction of lipids with short-chain alcohols such as methanol (in a process called methanolysis) or ethanol (by ethanolysis), along with glycerol as co-product. Even though alkaline methanolysis is known to achieve high biodiesel yield in shorter process time, drawbacks such as catalyst recovery and severe corrosion necessitate the need to search for alternative materials such as heterogeneous catalysts and biocatalysts (Lam et al., 2010; Mehra, 2018).

Methanolysis over KNO_3 activated MgO-ZnO

The high activity of co-precipitation-derived CaO-ZnO mixed oxides with or without doses of K_2CO_3 for the methanolysis of sunflower oil has been established (Kesić et al., 2015). We therefore investigated the efficiency of KNO_3 activated, co-precipitation derived MgO-ZnO for the synthesis of biodiesel from gmelina oil. The conditions for biodiesel production such as temperature, reaction time, NaOH (or KNO_3 dose) and methanol-gmelina oil ratio were optimised (Sani and Gaya, 2019). The reaction in either case can be represented by Eq. 40.

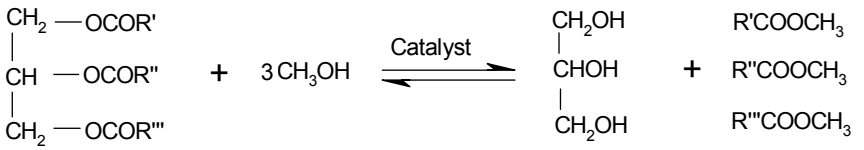

(40)

The Gmelina oil was extracted with hexane in a Soxhlet apparatus at 70 °C for 2h. The oil was pre-treated with methanolic NH_4OH to remove fatty acids. The catalyst was a KNO_3 (1-6 %w/w) impregnated MgO-ZnO nanocomposite, synthesised from equimolar solutions of $Zn(NO_3)_2.4H_2O$ and $Mg(NO_3)_2.4H_2O$ in presence of NH_4OH. The production of biodiesel was performed in a two-necked 500 mL glass reactor fitted with a condenser and thermometer. Prior to methanolysis, 0.8 g of the catalyst was first activated by agitation in methanol at 40 ^oC. Exactly 40 g of oil (previously heated at 100 ^oC for 30 min) was added to the batch reactor. The system was agitated using a magnetic stirrer. The catalyst was separated from the resulting mixture by filtration. The filtrate was allowed to stand for 24 h in separating funnel.

Subsequently, the glycerol resident at the bottom was separated from the biodiesel. The percentage of biodiesel yield was calculated using the following equation (Eq. 41):

$$\text{Biodiesel} = \frac{\text{Weight of biodiesel produced}}{\text{Weight of oil used}} \text{ x } 100 \qquad (41)$$

The optimisation of transesterification parameters and some catalyst characterisations can be visualised from our reference paper (Sani and Gaya, 2019). The crystalline structure of 4 % w/w KNO_3 activated MgO-ZnO, the best performing composite, was characterised using XRD plot which coincides with ZnO JCPDS card 36-1451 and MgO JCPDS file 01-072-0447. It also shows reflection peaks consistent with that of K—O JCPDS file 77-2176. The average crystallite size of the catalyst was calculated using Debye-Scherer equation (Eq. 16) to be 66.45 nm.

Table 19: *Energy dispersive X-ray data of the composite*

Element	Weight percentage (%)	Relative ratios
K	48.1	4.08
O	25.1	2.38
Zn	11.8	1.00
Mg	6.4	0.54
N	8.6	0.73

The elemental composition of the 4 % w/w KNO_3 activated MgO-ZnO catalyst is presented in Table 19. The ratios of the EDX peak concentrations in the table revealed atomic ratios which confirm the formula of the 4% w/w KNO_3 activated MgO-ZnO catalyst to be the non-stoichiometric oxide $K_{4.08}N_{0.73}Mg_{0.54}$-$ZnO_{2.38}$. The ATR-FTIR spectrum of the prepared catalyst revealed the sharp peak between at 527 cm^{-1} characteristics of stretching mode of Zn-O bond (Das and Khushalani, 2010). The incorporation of Mg^{2+} into the ZnO crystal structure is corroborated by the intense Mg-O peak at 474 cm^{-1} (Etacheri et al., 2012). The formation of K-O bond was confirmed by the peak at 491 cm^{-1}.

The fuel properties exhibited by gmelina oil, biodiesel (B100), the blends B20 and B50 and those of petrodiesel were determined (Table 20). A comparison with petrodiesel shows the unsuitability of the gmelina oil for use as fuel. Upon methanolysis however, the biodiesel product and its blends exhibit properties

consistent with those of ASTM standard. Particularly, the specific gravity (0.86) is more or less that of typical biodiesel (0.88) (Hoekman et al., 2012).The viscosity of the gmelina oil was reduced to 3.66 mm^2/s, a value that is lower than that of Moringa oleifera methyl esters (4.83 mm^2/s) (Rashid et al., 2008). Similarly, the specific gravity of gmelina oil is reduced down to acceptable values, by conversion to biodiesel blends B100, B50 and B20. The cloud point of the oil and B100 (-5 ^oC) nears that of typical cottonseed oil (-4 ^oC) (Knothe, 2008). The B100 Furthermore, the biodiesel and its blends (Table 20) are inherently "sweet" (with S content << 0.5%) which is usual with biomass oils and consistent with green emissions. The sulphur content of B100 and gmelina oil is even lower than that of petrodiesel. The cetane number for B100 was determined to be 51.7 which complies with ASTM (2002). This value is slightly higher than that reported for castor biodiesel (48.9) (Berman et al., 2011).

Table 20: *Fuel properties of gmelina oil, biodiesel and its blends with petrodiesel*

Fuel properties	Unit	Petrodiesel	Gmelina oil	B100	B50	B20	ASTM (2002)
Kinematic viscosity @40^{o}C	cSt	2.60	11.91	3.66	3.10	2.91	1.9-6.0
Sp. Gravity @27^{o}C	kg/L	0.846	0.90	0.863	0.860	0.846	0.860-0.900
Flash point	^{o}C	49	126	106	80	56	100-170
Combustion point	^{o}C	59	125	96	91	65	-
Cloud point	^{o}C	-5	6	2	-2	-5	-6 to 12
Sulphur content	%	0.167	0.012	0.0220	0.0929	0.100	-
Cetane number	^{o}C	-	ND[a]	51.7	49.5	48.6	48-65

[a]Not determined

The products of methanolysis were detected by Shimadzu-QC2010 Plus model, Gas Chromatography Mass Spectroscopy (GC-MS). Chromatograms were obtained (Fig. 44) and interpreted using NIST107.LIB GC library. There are fourteen peaks on the chromatogram, corresponding to different fatty acid methyl esters.

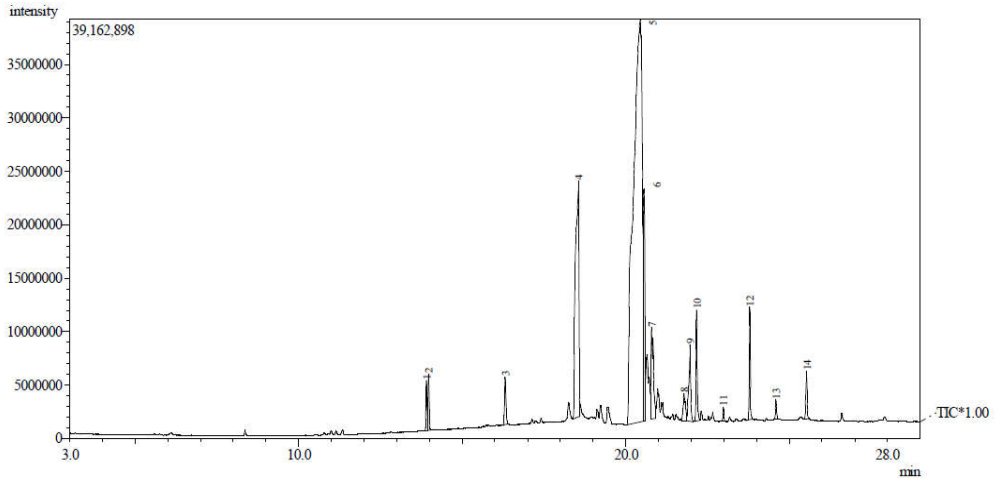

Fig. 44: *Elution peaks of fatty acid methyl esters with petroselinic acid methyl ester dominating the chromatogram*

The obtained fatty acid methyl esters and their retention property are displayed in Table 21. Majority of the compounds have a base peak at m/z = 74 indicating a common fragment $[CH_2{=}CHCH_2CH_2]^+$. The compound petroselinic acid methyl ester (or 6-octadecanoic acid methyl ester) eluted at 20 min retention time, has the broadest and most intense peak and accounts for about 62 % of the fatty acid methyl esters yield of the methanolysis process.

Table 21: *Chemical and common names of the fatty acid methyl ester (FAME) of the as-prepared biodiesel*

Peak No.	Retention time (min)	Peak area (%)	Assignment of peaks	C atoms
1	13.908	0.94	Dodecanoic (capric) acid methyl ester	C_{13}
2	13.975	0.98	Tridecanoic acid methyl ester	C_{14}
3	16.317	1.21	Tetradecanoic (myristic) acid methyl ester	C_{15}
4	18.550	14.22	Hexadecanoic (or palmitic) acid methyl ester	C_{18}
5	20.442	62.22	6-octadecanoic (or petroselinic) acid methyl ester	C_{19}

Peak No.	Retention time (min)	Peak area (%)	Assignment of peaks	C atoms
6	20.567	6.37	Octadecanoic (or stearic) acid methyl ester	C_{19}
7	20.792	3.97	Linolelaidic (or 9,12-Octadecadienoic) acid methyl ester	C_{19}
8	21.783	1.18	5,8-octadecadienoic acid methyl ester	C_{19}
9	21.958	2.41	9-octadecanoic (or elaidic) acid methyl ester	C_{19}
10	22.167	2.39	Eicosanoic (arachidic) acid methyl ester	C_{21}
11	22.983	0.26	Heptacosanoic acid methyl ester	C_{22}
12	23.792	2.30	Docosanoic (or behenic) acid methyl ester	C_{23}
13	24.592	0.39	Tricosanoic acid methyl ester	C_{24}
14	25.525	1.17	Tetracosanoic (or lignoceric) acid methyl ester	C_{25}

Transesterification Kinetics

The triglyceride conversion is traditionally first-order and can be used to evaluate the reaction rate constant (Nautiyal et al., 2014). Basically, the logarithmic function of FAME is related to time by Eq. (42)

$$\ln[FAME]_t - \ln[FAME]_o = k_1 t \qquad (42)$$

Where $[FAME]_0$= initial concentration of fatty acid methyl ester at time t = 0 and $[FAME]_t$ is the concentration at time t. The plot of $\ln[FAME]_t$ against t (Fig. 45) for the heterogeneous system gives a straight line with a correlation coefficient (R^2) of 0.986 indicating consistency with pseudo-first-order. The slope of the plot which equals to the rate constant (k_1) of the heterogeneous process is 4.8×10^{-3} min^{-1}.

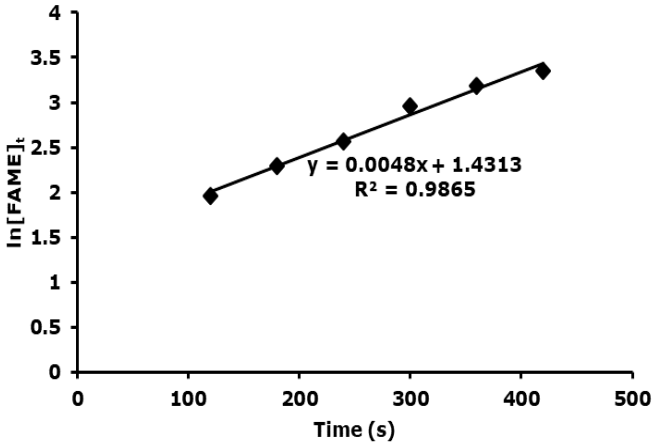

Fig. 45: *First-order kinetic plot of gmelina oil conversion over KNO_3 activated MgO-ZnO composite*

Activation Parameters

Temperature dependence results permitted the estimation of energies of activation. The logarithmic function of the rate constant for the biodiesel production is related to activation energy by the Arrhenius equation (Eq. 43).

$$\ln k = \ln A - \frac{E_a}{RT} \tag{43}$$

Where A is the Arrhenius factor (hr^{-1}), E_a is the activation energy (J/mol K), R is the molar gas constant (8.314 J /mol K) and T is the absolute temperature (K). Activation functions were obtained from the plot of lnk against *1/T* (Fig. 46). The activation energy and the pre-exponential factor for the $K_{4.08}N_{0.73}Mg_{0.54}$-$ZnO_{2.38}$ mediated biodiesel synthesis are 68.92 kJ/mol and 9.698×10^{7} min^{-1}, respectively, while the corresponding values for the NaOH-assisted process are 38.55 kJ/mol, 2.75×10^{4} min^{-1}.

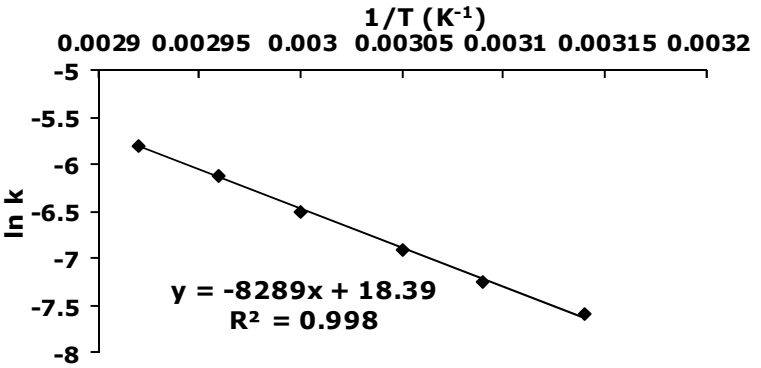

Fig. 46: *Arrhenius plot for the conversion of gmelina oil over KNO_3 activated MgO-ZnO composite*

The Eyring equation (expressed as Eq. 44) permits the estimation of other energies of activation (ΔG^*, ΔH^*, ΔS^*).

$$\ln\left(\frac{k}{T}\right) = -\left(\frac{\Delta H}{RT}\right) - \left[\ln\left(\frac{k_b}{h}\right) + \frac{\Delta S}{R}\right] \qquad (44)$$

Where k_b is the Boltzmann constant (1.38×10^{-23} J/K) and h is the Plank's constant (6.63×10^{-34} Js) while other quantities have their usual meaning. A plot of $\ln\left(\frac{k}{T}\right)$ against the inverse of temperature ($1/T$) at 338 K as in Figure 47 gives a slope equal to $-\frac{\Delta H}{R}$ while the intercept provides $\frac{\Delta S}{R}$.

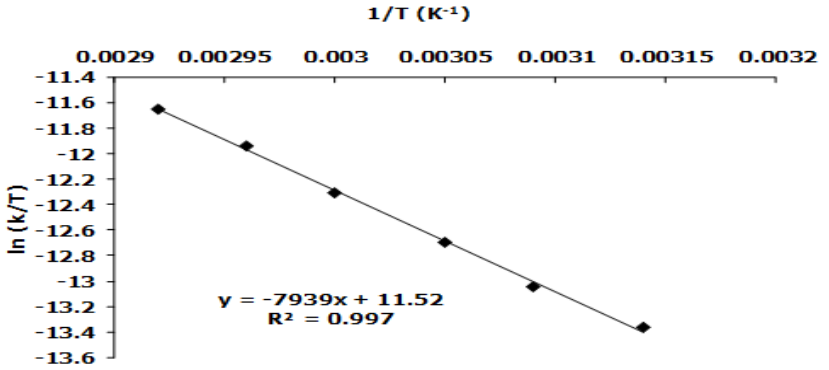

Figure 47: *Eyring plot showing the variation of ln(k/T) with 1/T for gmelina oil conversion over KNO_3 activated MgO-ZnO composite*

Table 22: *Activation parameters of gmelina biodiesel against reference values*

Methyl esters*	ΔG (kJ/mol)	ΔH (kJ/mol)	ΔS (kJ/mol K)	Reference
GME	100.50	66.004	-0.102	This work
RME	105.6	139.5	-98.0	(Astria et al., 2011)
CME	96.128	36.124	-180.19	(Ahmad et al., 2014)
SPME	92.71	16.35	-232.83	(Nautiyal et al., 2014)

*Gmelina methyl esters (GME), rapeseed methyl esters (RME), Chlorella methyl esters (CME), *Spirulina platensis* methyl esters (SPME).

The activation properties for gmelina biodiesel are presented in Table 22. Also in the same table for the sake of comparison are thermodynamic properties of the methyl esters of rapeseed, *Chlorella* and *Spirulina platensis*. The Gibbs free energy, enthalpy and entropy of the gmelina methyl esters produced by the heterogeneous catalyst are 100.50 kJ/mol, 66.00 kJ/mol and -0.102 kJ/mol K. The corresponding activation properties of the NaOH base system are 92.14 kJ/mol, 34.23 kJ/mol and -0.174 kJ/mol K. The enthalpies of activation are within the range reported in various literature. As seen from the Table, the gmelina transesterification process is characterized by negative entropies of smaller magnitude which implies the formation or more ordered transient structures en route the formation of methyl esters (Engel and Reid, 2006).

In-Situ Petroleum Upgrade Catalysts

Crude oil forms as light or heavy form all over the world. Even the conventional crude reserves are now trending heavier with continuous use. Therefore, the interest to maximise oil recovery increases. Ordinarily, the traditional heavy oil recovery stages leave behind a large amount of oil trapped in porous reservoir structure, necessitating additional or enhanced oil recovery (EOR). The integration of downhole in-situ upgrading along with oil recovery techniques has the potential to not only improve the production efficiency but also the quality of the produced oil, avoiding several surface handling costs and processing challenges. We have recently written a good background on the catalysts and formulations used in oil upgrading (Gaya, 2021).

We investigated the applicability of different zeolite-supported Ni-Co-Mo for hydrocracking using decalin (shown in Fig. 49), as model light oil, towards possible use of these catalysts in heavy crude upgrade. The metals (Ni-Co-Mo) were loaded in atomic mass fractions (0.300 : 0.175 : 0.525, respectively) by impregnation onto the supports to produce 5 wt%, 10 wt %, 15 wt % and 20 wt% contents. Support materials were varied based on SiO_2/Al_2O_3 ratio (1:50; 1:5; 1:1; 1:20; 1:280) using as received commercial zeolites (NH_4-ZSM-5, NH_4-zeolite-Y, H-Zeolite-Y, NH_4-Mordenite, NH_4-ZSM-5), respectively. The SiO_2 and Al_2O_3 -supported metals were also prepared to check backgrounds. For catalyst characterisations see Gaya et al. (2012).

Hydrocracking experiments were performed in the batch mode of a Milestone microwave Start D reactor using decahydronaphthalene or decalin (15.5 mL), and 5 mL ethanol (previously diluted by water as enhancer in a 1:1 ratio) as H-donor. The reactor was operated at 250 ^oC under autogenous pressure for 90 min. The resulting sample from the hydroprocess dried with Na_2SO_4 and centrifuged at 1000 rpm for 5 min. The top layer was a dark orange coloured oil. The bottom layer consisted of a plain orange wax, presumably containing residues.

The waxy top translucent layer was characterised by GC-MS with a Varian GC 3800 coupled to a Varian Saturn 2200 ion trap fitted with a Varian Factor Four VF-5ms column (30 m × 0.25 mm i.d., 0.25-μm film thickness). The GC-MS results were supplemented by FTIR analysis using a Perkin Elmer Spectrum facility operated at spectral range of 4000-400 cm^{-1}. The liquid product was dropped as film between two NaCl discs using glass capillary tube.

Cyclohexene derivatives were detected by GC-MS at different retention times (RT min): 3-ethylcyclohexene (RT = 6.898 min), 3-propylcyclohexene (RT = 6.404 min), 1-propyl or 1-butyl cyclohexene (RT = 6.410). Tetralin (1,2,3,4-tetrahydomapthalene) was observed near 7.474 min. The starting compound decalin was detected at 5.37 min. The analysis of the FTIR absorption spectra of decalin before and after hydrocracking corroborates the presence of these cyclohexene products. Decalin shows absorption at 2919 cm^{-1} for sp^3 C-H anti-symmetric stretching while absorption at 2851 cm^{-1} is due to C-H symmetric stretching. Absorptions at 1449 cm^{-1}, 666 $cm^{-1}$and 452 cm^{-1} are for C-H bending

vibrations. After the hydrocracking reaction, several compounds were formed. The FTIR absorption frequencies of the functional groups of these compounds are displayed in Fig. 48. The absorption frequency of acyclic C=C was at 1648 cm^{-1} (medium, broad band). The emergence of absorption band at 839 cm^{-1} which was absent in decalin spectrum, shows the presence of alkene.

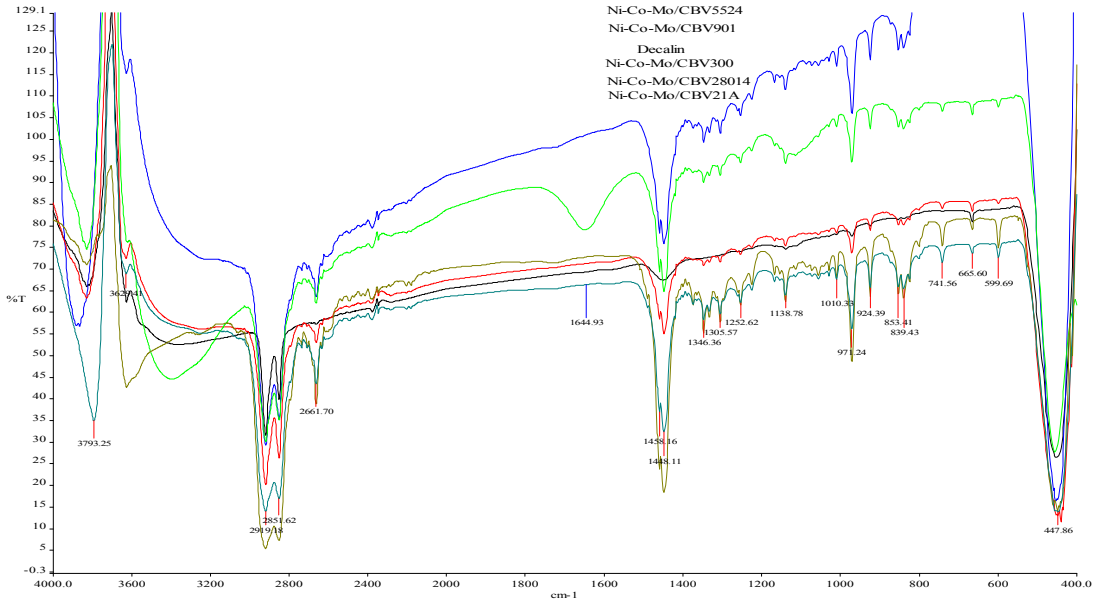

Fig. 48: *Overlay of the FTIR spectra of the products of decalin before and after hydrocracking over 5wt% Ni-Co-Mo/zeolites*

The absorption frequency at 971 cm^{-1} shows the presence of trans-double bond which in turn indicates the presence of R-CH=CH-R (E). The absorption frequency at 741 cm^{-1} shows the presence of cis-disubstituted alkene with structure R-CH=CH-R (Z). The lone peak 1138 cm^{-1} shows the presence of symmetrical ether (R-O-R). This is confirmed by C-O-C absorption band at 853 cm^{-1}. The pair of absorption bands near 1333 cm^{-1} and 1224 cm^{-1} shows the presence of phenolic C-OH (Ph-OH). This is confirmed by the weak absorption at 3300 cm^{-1} (Pavia et al., 2009) and by electronic absorption spectrum at 274 nm. This appears to be selective transformation as this functional group was not detected except on hydrocracking over 5 wt% Ni-Co-Mo/H-Zeolite-Y. Similarly, the other zeolite-Y based supported Ni-Co-Mo (5 wt % Ni-Co-Mo/NH_4-zeolite-Y) yielded spiro[4.5] decane which

could only be detected on using DB-5 column (installed on Clarus 600 Perkin Elmer GC-MS) at 6.02 min. Spiro [4.5] decane has been reported also by Haas et al. (2012) in the hydrogeneolysis of decalin over Ir/ and Pt/silica catalysts.

Mechanism of Ring Opening of Decalin

The following reaction mechanism may be speculated for the hydrodecomposition of decalin in presence of ethanol as H-donor. One of the decalin rings can open at C atom α- or β- to one of the fused carbon atoms. In the former case 1-butylcyclohexane is formed while the latter results in the formation of 3-(or 1-)-cyclohexene. Hydrogen is supplied by ethanol and steam used in the process but this results also in the formation of ethers and organic alcohols. Tetralin is probably directly formed from decalin as ealier proposed by Wang et al. (2012) in the ring opening of naphthalene.

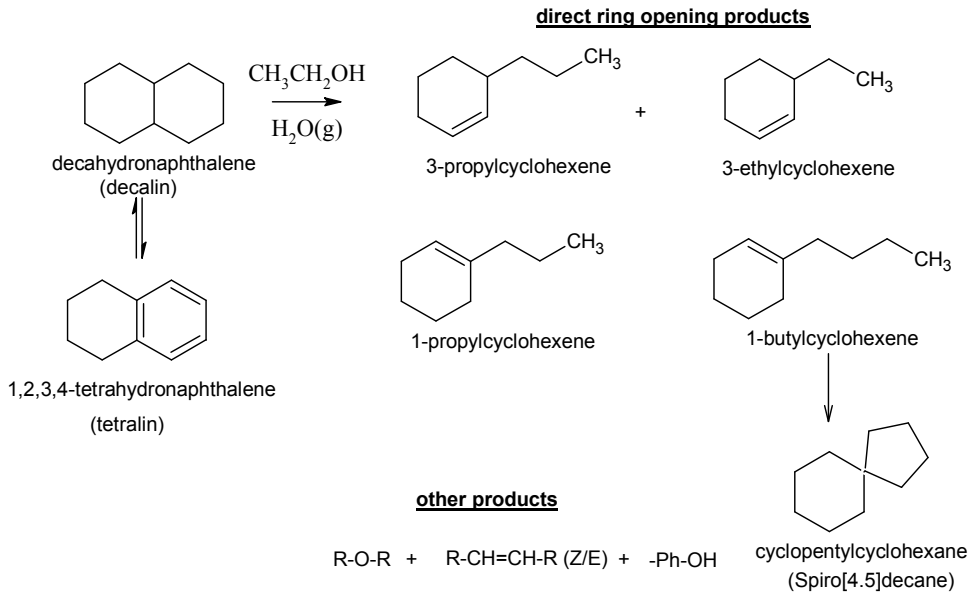

Fig. 49: *Tentative mechanism for the ring cracking of decalin*

HOMOGENEOUS CATALYSIS

We have performed some work in the areas of homogeneous catalysis which include comparative studies with NaOH transesterification catalyst (Sani and Gaya, 2019), photo-Fenton (Ibrahim and Gaya, 2020) and photo-Fenton like catalysts (Abubakar

and Gaya, 2019). We are going to selectively present the photo-Fenton-like study, because we have seen the sample of transesterification using the heterogeneous catalyst and the photo-Fenton-like work is an extension of photo-Fenton study.

Photo-Fenton-Like Degradation of Basic Violet 3

Photo-Fenton is a member of the advanced oxidation processes, which rely on powerful in situ-generated hydroxyl radicals to degrade organic pollutants. The Fenton reagent is a chemical system consisting usually of iron (II) salts or oxide, and hydrogen peroxide (H_2O_2), whereas the Fenton-like replaces iron with another metal. Various Fenton or Fenton-like systems have been utilized for the removal of basic dyes. Previously, Basic Violet 10 has been decontaminated by coupling Fenton with sonication (Hassani et al., 2018) or electric bias (Palma-Goyes et al., 2010).

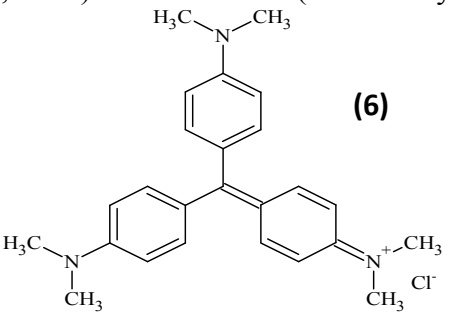

(6)

The degradation of basic violet 3 (BV3), compound **(6)**, by the photo-Fenton process has recently been described (Rehman et al., 2018). One of the disadvantages of Fenton and photo-Fenton processes is the need for iron salts (Serra-Clusellas et al., 2018). Consequently, there is intensive interest in Fenton-like systems. Attention has been geared towards the utilization of Cu(II)/Cu(I) Fenton-like systems for their impeccable efficiency (Lyu et al., 2015). Basic Violet dye has been removed by a different photo-Fenton-like reactivity system based on Fe(III) and H_2O_2 (Fan et al., 2009). So, we were prompted to study for the first time, the degradation of Basic Violet in an irradiated Fenton-like system of Cu(I) + H_2O_2.

Box-Behnken Experimental Design

Theoretically, Box-Behnken design consists of a rotatable, quadratic frame having no embedded factorial or fractional factorial points where the factor combinations are at the midpoints of the edges of the factor space and at the centre.

Table 23: *Input levels and Box-Behnken codes of variables.*

Variables	Levels (and codes)		
A-pH	1 (-1)	5.5(0)	11(+1)
B-H_2O_2 (mg/L)	20(-1)	60(0)	120(+1)
C-Cu^+ (mg/L)	5(-1)	15(0)	30(+1)
D-Dye (mg/L)	10(-1)	30(0)	60(+1)

In this study, 29 experiments were performed in a 500 ml borosilicate batch reactor installed with 2000 Wm^{-2} halogen lamp. The experiments were based on four independent variables (pH, Cu^+ as $CuNO_3$ dosage, H_2O_2 and initial BV3 concentration) combined at three levels. The input levels of these variables with their codes are shown in Table 23. These were processed using Design Expert v6. Samples were taken at the pre-determined intervals of time. The progress of the degradation process was monitored by performing UV-Visible spectrometry at 580 nm using a Perkin Elmer Lambda 25 UV-visible spectrophotometer. The percent degradation ($\% D_{exp}$) of the dyes was calculated using Eq. 45.

$$\% \, D_{exp} = \left(1 - \frac{C_t}{C_o}\right) \text{ x } 100 \qquad (45)$$

Where C_o is the initial concentration of the dye, C_t is the concentration of BV3 at a given time t. The progress of the mineralization process was monitored by the measurements of total organic carbon (TOC) using Shimadzu 00077 TOC analyser. The extent of mineralization of each dye was calculated using Eq. 46.

$$\% \text{ mineralisation} = \left(1 - \frac{TOC_t}{TOC_o}\right) \text{ x } 100 \qquad (46)$$

Where TOC_o is the total organic carbon before mineralization and TOC_t is the total organic carbon at a given time t.

Table 24: *Actual values of BV3 degradation efficiencies along with the predicted values*

Run	A:pH	B:H_2O_2	C:Cu(I)	D: BV3	% D_{exp}	% D_{pred}
1	1.00	0.00	-1.00	0.00	80	78.74
2	1.00	0.00	0.00	-1.00	85	96.56
3	0.00	0.00	0.00	0.00	68	71.68
4	0.00	0.00	0.00	0.00	80	71.68
5	-1.00	0.00	-1.00	0.00	32	41.44
6	0.00	1.00	-1.00	0.00	45	38.91
7	0.00	0.00	0.00	0.00	80	71.68
8	0.00	1.00	0.00	-1.00	50	56.73
9	-1.00	0.00	0.00	-1.00	50	59.23
10	1.00	-1.00	0.00	0.00	95	90.95
11	0.00	0.00	1.00	1.00	60	63.69
12	0.00	-1.00	0.00	-1.00	70	66.06
13	1.00	0.00	0.00	1.00	99	96.56
14	0.00	-1.00	-1.00	0.00	48	48.24
15	0.00	1.00	0.00	1.00	50	56.73
16	0.00	0.00	1.00	-1.00	55	63.69
17	0.00	0.00	0.00	0.00	82	71.68
18	0.00	0.00	-1.00	1.00	60	53.85
19	0.00	1.00	1.00	0.00	50	48.74
20	0.00	0.00	-1.00	-1.00	50	53.85
21	0.00	-1.00	1.00	0.00	55	58.07
22	-1.00	1.00	0.00	0.00	52	56.73
23	0.00	0.00	0.00	0.00	65	71.68
24	1.00	0.00	1.00	0.00	94	88.57
25	1.00	1.00	0.00	0.00	80	81.61
26	-1.00	-1.00	0.00	0.00	50	53.61
27	0.00	-1.00	0.00	1.00	65	66.06
28	-1.00	0.00	0.00	1.00	65	59.23
29	-1.00	0.00	1.00	0.00	60	51.24

The values of BV3 degradation efficiency obtained from photo-Fenton-like experiment (% D) were processed using Box-Behnken design to obtain statistically valid predicted values (% D_{pred}) as listed in Table 24. Both the experimental and predicted efficiencies showed a good correlation as corroborated by the outstanding linear correlation of normal probabilities with studentised residuals. However, because the BV3 concentration term D, the cross terms AB, AC, *AD*, *BC*, *BD*, *CD* and the square term D^2 do not support the model hierarchy, the degradation model is a reduced quadratic type shown in Eq. (47). Consequently, the operating variables

can be said to influence the efficiency of the Fenton-like photodegradation process within the ranges of this study except for the initial BV3 concentration.

$$\%\ D_{pred} = 71.68 + 18.67A - 4.67B + 4.92C + 6.22A^2 - 10.28B^2 - 12.91C^2 \quad (47)$$

From Table 24, the optimum photo-Fenton-like degradation efficiency (99 %) corresponds to pH 11, 60 mg/L H_2O_2, 15 mg/L Cu(I) which is a bit higher than the efficiency (97.5 %) reported for a Box-Behnken designed photo-Fenton removal of Direct Red 28 (Ay et al., 2009). Unlike in the case of photo-Fenton where the pH must be acidic to avoid precipitation of iron(III) hydroxide (Evonic, 2018), the photo-Fenton-like process in this study performed best at pH 11.

The analysis of variance of the reduced quadratic model applicable to this study is displayed in Table 25. Other statistical justifications can be seen in our reference report (Abubakar and Gaya, 2019). From the Table, the F-values of the model and model terms A, B, C, A^2, B^2 and C^2 are > 4 which indicates low chances of noise and confirms the significance of the quadratic model. This is further corroborated by the values of Prob > F which are all < 0.05 less. The lack of fit of 0.6715 is not significant relative to the pure error which promises good model fit.

Table 25: *Analysis of variance for of the reduced quadratic model*

Source	Sum of squares	DF	Mean square	F-value	Prob > F	Remark
Model	6942.18	6	1157.03	22.20	< 0.0001	Significant
A	*4181.33*	*1*	*4181.33*	*80.24*	*< 0.0001*	
B	*261.33*	*1*	*261.33*	*5.02*	*0.0356*	
C	*290.08*	*1*	*290.08*	*5.57*	*0.0276*	
A^2	*260.23*	*1*	*260.23*	*4.99*	*0.0359*	
B^2	*710.98*	*1*	*710.98*	*13.64*	*0.0013*	
C^2	*1120.42*	*1*	*1120.42*	*21.50*	*0.0001*	
Residual	1146.37	22	52.11			
Lack of Fit	*898.37*	*18*	*49.91*	*0.80*	*0.6715*	Not significant
Pure Error	*248.00*	*4*	*62.00*			
Cor Total	8088.55	28				

Effect of Operating Variables

The response surface plots showing the effect of operating parameters are displayed in Fig. 50. The effect of H_2O_2 addition vis-à-vis pH (Fig. 50a) shows increase in the photo-Fenton-like degradation with either of pH or H_2O_2. However, even with little hydrogen peroxide, pH can bring significant photo-Fenton-like degradation up to 94 %. The response surface (Fig. 50b) shows that only a moderate combination of H_2O_2 concentration and Cu(I) is required to provide the best synergism. At the other end, the response surface showing the interplay between BV3 and H_2O_2 concentration (Fig. 50c) shows no influence of the dye on the photo-Fenton-like efficiency.

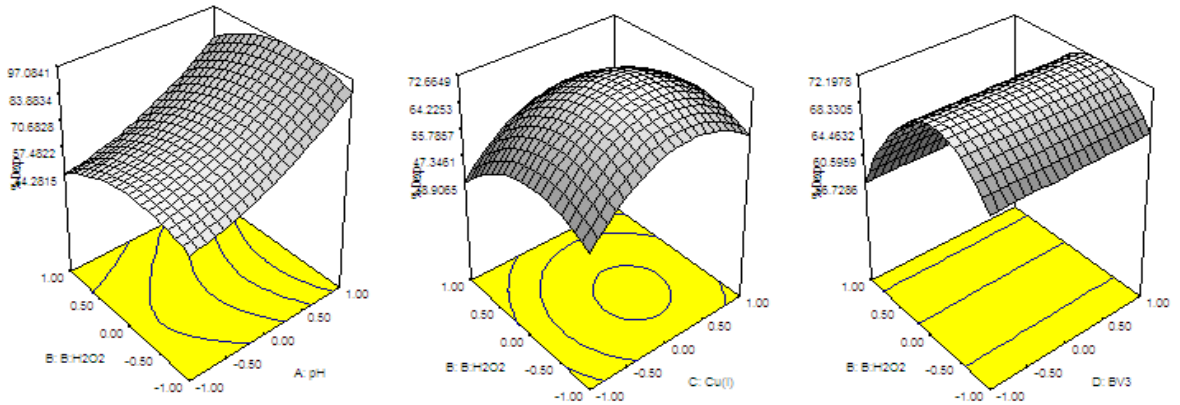

Fig. 50: *Response surface plots showing the interaction of H_2O_2 with (a) pH (b) Cu(I) doses (c) BV3 initial concentration*

Mineralization and Kinetics

Even though 99% of BV3 has been degraded, mineralization, which is the most desirable, may not be as effective. In this study, mineralization has was monitored based on TOC measurement and the results of this study are shown in Fig. 51. As seen from the figure, the mineralization of BV3 increases steadily with irradiation time up to a maximum of 70 %. This level of mineralization is lower than that of the photo-Fenton-like mineralization of phenol in presence of Cu-iminodisuccinic acid in which 95 % mineralization was realized in 60 min (Fiorentino et al., 2018).

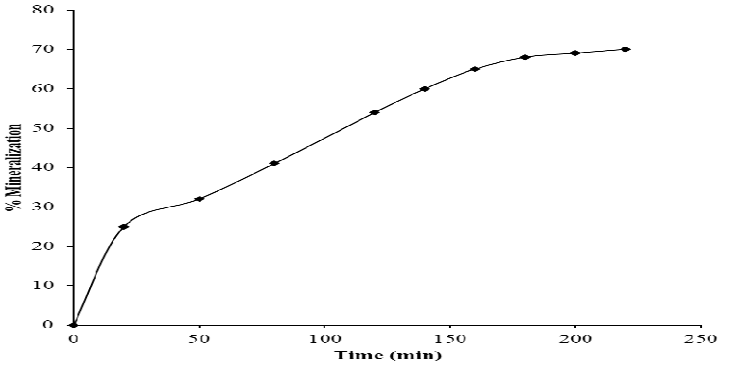

Fig. 51: *Variation of BV3 mineralization with time at optimized conditions*

The chemical reactions involved in the generation of oxidizing radicals in the Cu(I) photo-Fenton-like degradation of BV3 are represented by Eq. (48) to (52) (Nichela et al., 2013). Reaction (52) shows how the BV3 is converted to mineralization products such as CO_2, water and mineral ions.

$$Cu^{+} + H_2O_2 \rightarrow Cu^{2+} + \bullet OH + OH^{-} \quad (48)$$

$$Cu^{2+} + H_2O_2 \rightarrow Cu^{+} + \bullet OOH + H^{+} \quad (49)$$

$$Cu^{2+} + \bullet OOH \rightarrow Cu^{+} + H^{+} + O_2 \quad (50)$$

$$O_2^{\bullet-} + Cu^{2+} \rightarrow Cu^{+} + O_2 \quad (51)$$

$$BV3 + (\bullet OH, \bullet OOH, O_2^{\bullet-}) \rightarrow \text{Mineralization products} \quad (52)$$

Reaction (49) is accelerated by increasing pH. This is perhaps why a high pH in this study resulted in the best performance of the photo-Fenton-like system. The degradation of BV3 was evaluated using pseudo-first-order (Eq. 53), and pseudo-second-order kinetic schemes.

$$\ln C_o = \ln C_t - kt \quad (53)$$

Where, C_o and C_t are concentration of the dyes at time 0 and at time t. The k is the Pseudo order first order rate constant and t is the time in minutes. The process agreed with psudo first-order model (R = 0.997) with rate constant of 0.143 min^{-1}.

The IR spectral study was employed to monitor the disappearance of BV3 functional groups upon copper (I) photocatalytic degradation. The strong bands at 1577 and

1480 in Fig. 52 indicate the presence of benzene C=C stretch. Annihilation of these peaks (Fig. 52) is evidence for the opening or BV3 rings en route degradation. The peak at 1160 cm^{-1} represents C-N stretch (Coates, 2000). The two peaks at 760 and 720 cm^{-1} in Fig. 52 represent C-H bend of benzene. The appearance of the strong absorption bands at 3321 and 1639 (Fig. 52) confirm the formation of smaller molecules consisting of a secondary amide N-H and/or alkene-based C=C bonds as degradation products.

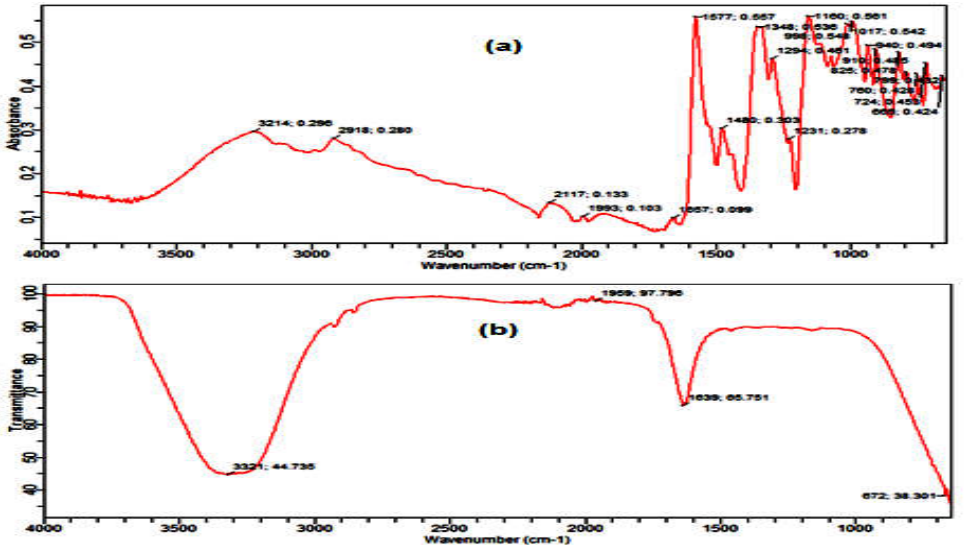

Fig. 52: *Fourier transform infrared spectra of BV3. (a) Before degradation. (b) After degradation*

ADSORPTION

Kinetic investigations span both catalytic and non-catalytic processes. We have so far shown part of our works with the catalysed processes such as photocatalysis and catalysis, some of which require surface solute retention/adsorption stage to proceed. Adsorption can also be applied in corrosion inhibition and in the removal of toxic substances. We have shown that plants, including submerged water plants, are good adsorbents of aqueous pollutants (Gaya et al., 2013). We are going to discuss some aspects of our investigation of adsorption-type corrosion inhibitors and activated carbon nanopores.

Determinants of Efficiency in Activated Carbon Nanopores

Lead, cadmium and mercury make the top of the "big three" heavy metal pollutants associated with poisoning (Liu et al., 2011). In fact, because they are pervasive in the environment, we have detected some of these metals even in spices (Gaya and Ikechukwu, 2016). In the search for efficient, low-cost or ready available activated carbon (AC), we synthesised some non-uniformly sized nanopores from doum palm shell, by carbonization in air at 500 °C and activation using KOH, NaOH and $ZnCl_2$.

Property-Activity Relationship

The influence of agitation time on the adsorption of Cd^{2+} or Pb^{2+} (50 ml of 50 mg/l) was studied in a batch system containing 2.5 g activated carbon (KOH-AC, NaOH-AC, $ZnCl_2$-AC or regular AC), agitated at 350 rpm and equilibrium adsorption time of 60 min for all the activated carbon powders. The performance of the activated carbons $ZnCl_2$-AC, KOH-AC, NaOH-AC and regular AC, at the optimum adsorbent doses (1.5 g, 1.0 g, 1.0 g, and 1.0 g) were 99.92%, 99.60%, 99.96% and 82.52%), respectively. The metal concentration (mg/g) retained on the adsorbent phase (q_e) and the removal efficiency (%) of the adsorbent preparations were calculated using Eq. 54 and 55, respectively:

$$q_e = \frac{C_o - C_e}{m} \text{ x } V \tag{54}$$

$$\text{Removal efficiency (\%)} = \frac{C_o - C_e}{C_o} \text{ x } 100 \tag{55}$$

Where C_o and C_e are the concentrations (mg/l) of Cd^{2+} and Pb^{2+} analysed using atomic absorption spectrometer (AAS) before and after adsorption respectively, V (ml) is the volume of the Cd^{2+} or Pb^{2+} and m (g) is the mass of the adsorbent.

In order to find the factor responsible for high efficiency of adsorption with KOH-AC and NaOH-AC, adsorption-desorption isotherms were examined using Belsorp Mini II, Japan. The N_2 adsorption-desorption isotherm of NaOH-AC (Fig. 53) was of type IV, which based on the Bauneuer-Deming-Deming-Teller (BDDT) interpretation is characteristic of mesoporous material. The characteristic hysteresis loop of this type of porous material can be easily seen from the figure.

Obviously, the high adsorption capacity of the NaOH-AC (S_{BET} = 226.02 m^2/g) compared to the other modified activated carbon adsorbents ($S_{BET\ (KOH\text{-}AC)}$ = 5.41 m^2/g and $S_{BET\ (ZnCl_2\text{-}AC)}$ = 0.84 m^2/g) is surface area-driven. In addition, this material had the lowest ash content (8.2%) which further speaks for its high performance compared. To corroborate this view the pore size distribution was assessed by the Barrett–Joyner–Halenda (BJH) method (Fig. 54). The results were positive as NaOH-AC showed relatively higher porosity (average pore volume V_p= 0.096 cm^3/g; estimated at p/p_o = 0.990) compared to the KOH-AC and $ZnCl_2$-AC (V_p = 0.068 cm^3/g and 0.008 cm^3/g). From Fig. 54(a) it can be concluded that the NaOH-AC predominantly consists of mesopores. The average mesopore diameter of this activated carbon was determined to be 3.99 nm. Interestingly, the $ZnCl_2$-AC is also mesoporous with a larger average pore diameter (40.2 nm). However, the KOH-AC isotherm displays a type III macropore with a larger average pore diameter (50.12 nm) which means the remarkable performance of this activated carbon is not surface area-driven.

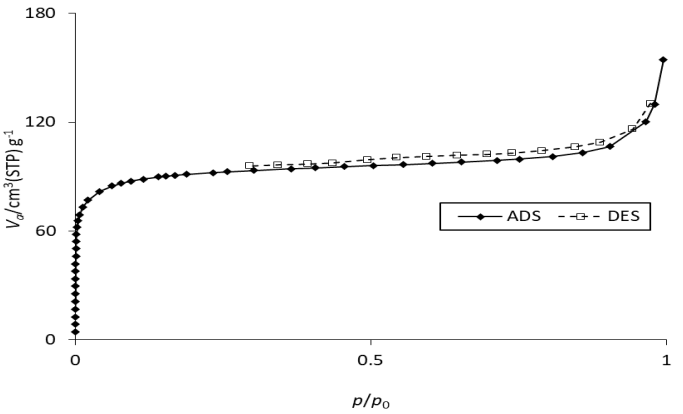

Fig. 53: *Adsorption-desorption isotherm of NaOH-AC at 77K*

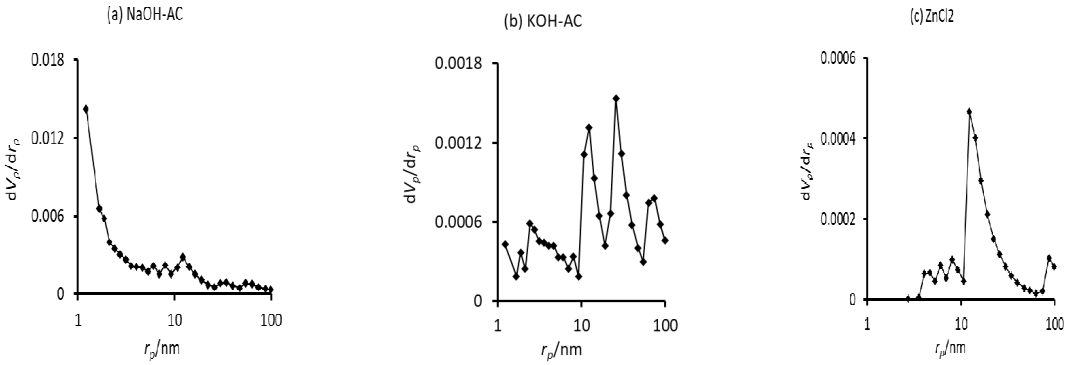

Fig. 54: *The BJH pore size distribution of NaOH-AC (a), KOH-AC (b) and the regular AC*

In order to provide plausible explanation for the efficiency of KOH-AC, X-ray diffraction analysis (XRD) was conducted using Ital Structure APD2000 x-ray diffractometer. An overlay of the diffractograms for the activated carbons is shown in Fig. 55. Obviously, heat treatment has graphitized the activated carbons as indicated by the characteristic faces of the graphite lattice. The prominent diffraction peaks, common to all the activated carbons were observed at $2\theta = 24.1^o$, 38.3^o, 44.5^o. The 24.1^o is for the structural 002 reflection of the carbon layer of an activated carbon (Iijima, 1991, Acharya et al., 2009). The peak at $2\theta = 42.3^o$ is for the 10 reflection, an orientation resulting from a merger of 101 and 100 (Dandekar et al., 1998). The peak at 44.5^o corresponds to the sp^3 lattice reflections. The diffraction peaks of the KOH-AC are the sharpest and most intense due to the increased crystallinity, particle size and purity (KOH-AC > $ZnCl_2$-AC = regular AC > NaOH-AC) and perhaps the reason for its performance.

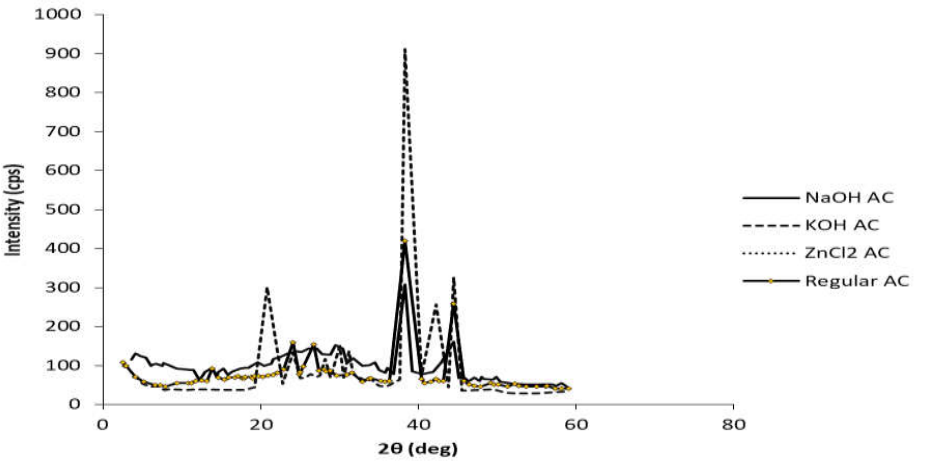

Fig. 55: *The XRD patterns of NaOH-AC, KOH-AC, $ZnCl_2$-AC and regular AC*

Particle size analysis was performed in triplicates on Nano S Malvern nanosizer. The size distribution of the particles is depicted by Fig. 56. From the insets (a) and (b) both KOH-AC and NaOH-AC showed unimodal particle size distribution with average particle size (nm) peaking at 190.10±0.00 and 43.82±0.00, respectively. The pore size range of the KOH-AC was 0.4-458.7 nm while the NaOH-AC was in the rage of 31-51 nm. Differently, bimodal pore size distribution was obtained for the $ZnCl_2$-AC and regular AC, falling amazingly within the same ranges (0.4-825 nm and 4145-6439 nm).

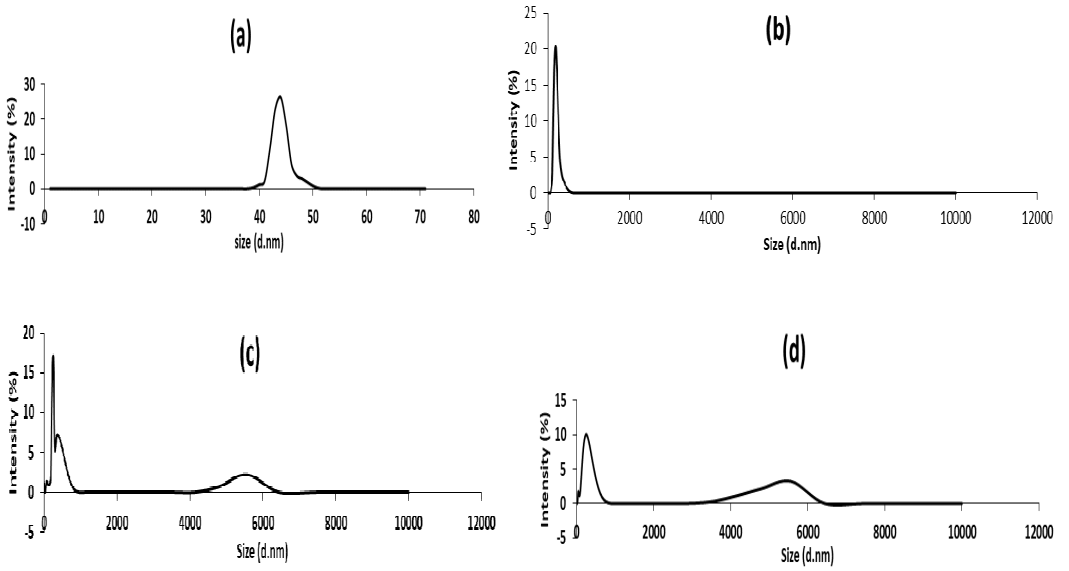

Fig. 56: *Particle size distribution of NaOH-AC (a), KOH-AC (b), $ZnCl_2$-AC (c) and regular AC (d)*

The high crystallinity of the KOH-AC particles prompted us to image surface morphologies of the activated carbons and visualise the variations. Fig. 57 displays the scanning electron micrographs of NaOH-AC, KOH-AC and the regular AC taken under the same operating conditions using Phenom electron microscope, ProX, MVE 1329F.. The variation in the surface morphology can be seen as we move from the regular AC (Fig. 57 (a)), to NaOH-AC (Fig. 57(b)), then to KOH-AC (Fig. 57(c)). The mesoporous NaOH-AC has a uniform fibrous sheets whereas the macroporous KOH-AC is pitted all over the surface. High crystallinity can be easily proved from the coarse texture displayed by the KOH-AC as opposed to the image of the NaOH-AC.

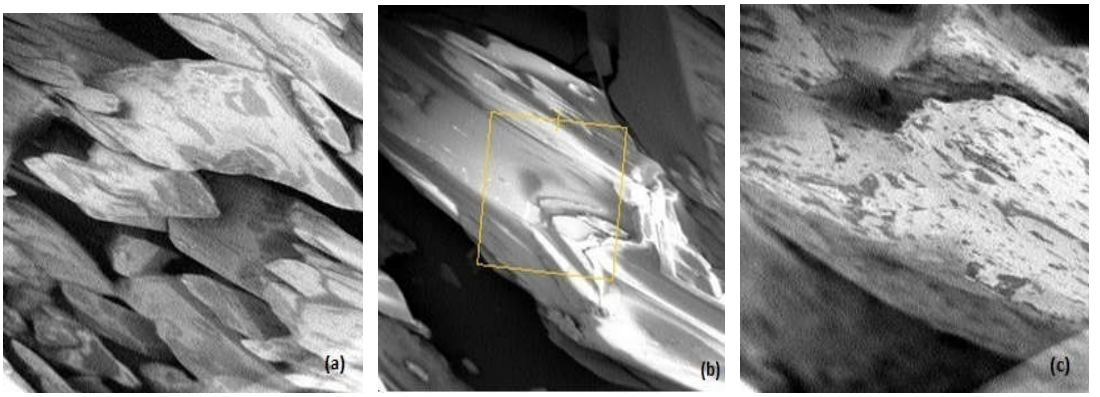

Fig. 57: *Scanning electron micrographs of the surface of regular AC (a), NaOH-AC (b) and KOA-AC (c), magnified up to 40,000X and taken at 15kV accelerating voltage*

Details of adsorption parameters, isotherms, kinetics and adsorption mechanism can be obtained from Gaya et al. (2015).

Side Chain Effect on Corrosion Inhibition by α-Amino Acids

Functional groups have mostly been regarded as zones via which certain inhibitors can protect etching metal parts. Study of the effect of substituent groups have been scanty in literature. Amino acids exhibit side substituent chain (aromatic or non-aromatic) in addition to $–NH_2$ and –COOH functional groups, hence may show unique behaviours in corrosive environment. We devoted a study to the investigation of the influence of non-polar, hydrophobic side chain of amino acid homologues namely glycine (Gly), alanine (Ala) and phenylalanine (Phe), on the inhibition of aluminium corrosion in 0.3 M HCl. It includes mass loss measurements, electrochemical measurements, quantal investigations and molecular dynamics. The mass loss measurements, isotherms, kinetic models, thermodynamics and reaction mechanism are detailed in our reference paper (Shehu et al., 2019).

Potentiodynamic Polarisation Profiles

Potentiodynamic polarisation techniques are widely used to investigate the type, behaviour, extent and rate of electrochemical corrosion. Linear polarization resistance (LPR) measurements were performed in 0.3 M HCl at 303 K using Model 668 AUTOLAB Potentiostat. From the polarization curves, Tafel slopes, corrosion

potential and corrosion current were obtained. The inhibitor efficiency IE (%) was calculated using Eq. 56.

$$IE(\%) = \left(\frac{CR_o - CR}{CR_o} \right) \text{x } 100 \qquad (56)$$

Where CR_o and CR are corrosion rates of the aluminium in aggressive environment with and without inhibitors, respectively. Table 26 shows the linear polarisation data obtained for aluminium corrosion in 0.3 M HCl with or without Gly, Ala or Phe. The shifts in corrosion potential (E_{corr}) were negative irrespective of the amino acid used. The highest corrosion rate (CR) and Ecorr values were obtained from the aluminium-HCl system without inhibitor. Generally, in both the mass loss and potentiodynamic polarisation studies, the inhibition efficiency (IE) values reached maximum with of 0.6 g/L amino acid. All of the amino acid inhibitors showed large negative shifts in E_{corr} (> 0.085V) confirming cathodic control (Noor, 2009). The lowest shift was obtained with 0.6 g/L phenylalanine which corresponds to the lowest inhibition efficiency (81 %) while the highest anti-corrosion efficiency (IE = 94 %) and the lowest cathodic Tafel slope (βc, 0.08826 $Vdec^{-1}$) were obtained with Ala.

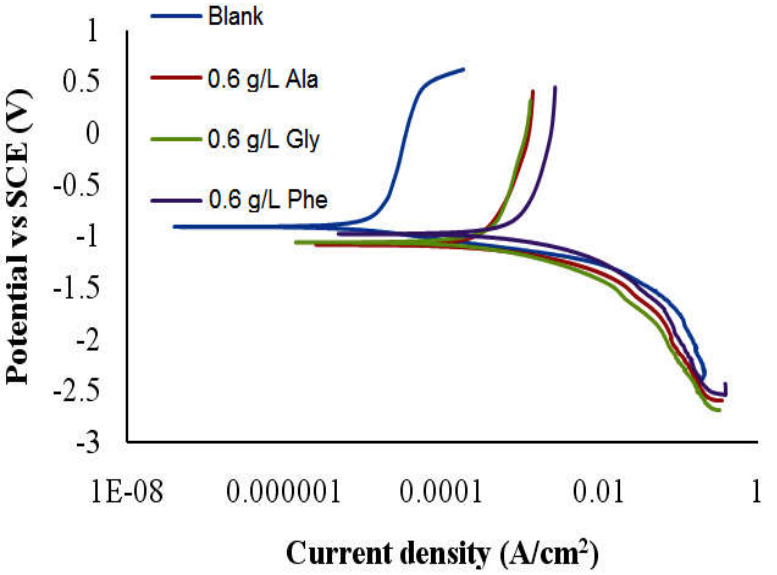

Fig. 58: *Tafel polarization curves for the corrosion of aluminium in 0.3M HCl solution containing 0.6 g/L Ala, Gly and Phe at 303 K*

The polarisation profiles of aluminium in 0.3 M hydrochloric acid with 0.6 g/L of Ala, Gly and Phe is shown in Fig. 58. The electropotentials range from -0.91 to -1.18 V and are more negative than those reported for flowing, aerated water, 0.5 to -0.8 V (Zhao et al., 2017). This is therefore revelatory of the severity of the corrosion in hydrochloric acid regimes of the study.

Table 26: *Linear polarization data for aluminium corrosion in 0.3 M HCl acid solutions in the presence and absence of inhibitors at 303K*

Al + $HCl_{(aq)}$	E_{corr} **(V)**	i_{corr} **(Acm^{-2})**	β_a **($Vdec^{-1}$)**	β_c **($Vdec^{-1}$)**	***CR*** **($mmyr^{-1}$)**	***IE*** **(%)**
Devoid of inhibitor	-0.91094	1.53×10^{-5}	0.18218	0.88364	5.8475	0
With 0.6g/L Gly	-1.06230	1.55×10^{-4}	0.27811	0.16131	0.5567	90
With 0.6g/L Ala	-1.08370	1.01×10^{-4}	0.14980	0.08826	0.3668	94
With 0.6g/L Phe	-0.97720	2.99×10^{-4}	0.26266	0.13419	1.0851	81

Surface Analysis of Etching

In order to study the changes in the aluminium with corrosion, scanning electron microscopy was performed. Micrographs obtained for different corrosion systems are shown in Fig. 59 (a) to (e). The development of incongruent pits on the regular aluminium surface (Fig. 59a) and overall structural deterioration can be seen in Fig. 59b due of contact with 0.3 M hydrochloric acid media for 4 h. This corrosion was inhibited by the addition of 0.6 g/L amino acids and pits were geometrically blocked, showing no pits or cracks especially in the presence of Gly. The order of this geometric blocking of the active surface sites and lessening of surficial roughness varies with amino acids as Ala (Fig. 59d) > Phe (Fig. 59e) > Gly (Fig. 59c) > Blank (Fig. 59b).

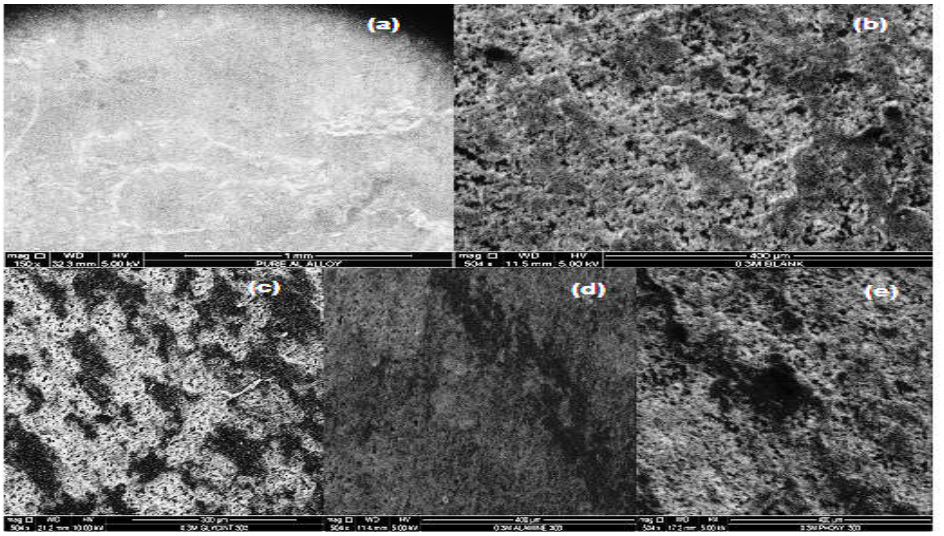

Fig. 59: *Scanning electron micrographs of (a) Pure aluminium (b) aluminium in 0.3M HCl (c) aluminium in 0.3M HCl + 0.6 g/L Gly at 303 K (d) aluminium in 0.3M HCl + 0.6 g/L Ala at 303 K (e) aluminium in 0.3M HCl + 0.6 g/L Phe at 303 K*

Quantal Examination of Molecular Effects

In order to study the effect of the molecular structure on inhibition efficiency, quantum chemical calculations was performed using DMol^3 module of Materials Studio software version 8.0 (BIOVIA, Accelrys) which is an implementation of density functional theory (DFT) in the local density approximation (LDA) regime. Calculations were done in the Perdew-Wang Correlation (PWC) form, at the double numerical quality plus d-functions (DND) atomic basis set level. It is well known that the higher the E_{HOMO} edge, the higher the ability of a molecule to donate electrons to lower-energy acceptor molecules (Fragoza-Mar et al., 2012). The reverse is the case for E_{LUMO}. The frontier molecular orbital diagrams of Gly, Ala and Phe exhibiting these energies are presented in Fig. 60.

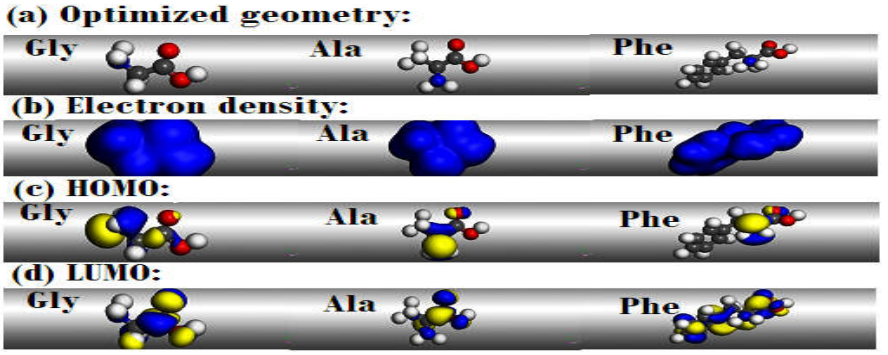

Fig. 60: *Frontier molecular orbital density and optimised structures of Gly, Ala and Phe from left to right respectively showing: (a) Structures (b) Total electron density (c) HOMO (d) LUMO. Colour scheme: White = H, blue = N, red = oxygen, grey = carbon*

The values of inhibition parameters are displayed in Table 27. It would be seen from the Table that the E_{HOMO} value of Ala was found to be the least (-5.559 eV), which makes it highly electron-donating, susceptible to electrostatic attraction in the Al^{3+} environment and an excellent corrosion inhibitor. The superiority of inhibition, strength of electron donation and a high tendency to interact with the aluminium can also be related to a high value of the fraction of electrons transferred (ΔN) (Dehdab et al., 2015), for which in this study Ala exhibits the highest ΔN value (0.5098).

Table 27: *Values of electronic parameters and eigenvalues of Gly, Ala and Phe*

Electronic/Structural property	Gly	Ala	Phe
HOMO (at orbital number)	20	24	44
LUMO (at orbital number)	21	25	45
E_{HOMO} (eV)	-5.871	-5.559	-5.642
E_{LUMO} (eV)	-1.292	-1.365	-1.453
ΔE (eV)	4.579	4.194	4.189
Molecular mass (g/mol)	75.067000	89.093800	165.191400
Ionization potential (IP) (eV)	5.871	1.365	1.453
Electron affinity (EA) (eV)	1.292	1.365	1.453
Absolute/Global hardness (η)	2.2895	2.0970	2.0945
Global softness (σ)	0.4368	0.4769	0.4774
Absolute electronegativity (χ)	3.5815	3.4620	3.5475
Total number of electrons	40.0	48.0	88.0
Fraction of electrons transferred (ΔN)	0.4408	0.5098	0.4900

In order to further investigate the local reactivity of the inhibitors due to different amino functional groups, the Fukui indices were calculated ab initio using DMol^3 Mulliken analysis of Materials Studio 8 (Table 28). The electrophilic and nucleophilic attack sites were represented by Fukui descriptors F^- and F^+, respectively. It can be seen from Table 6 that the electrophilic indices of Gly and Phe are oriented around the nitrogen atom N(5) and N(10) while that of Ala is centred around the oxygen atom O(5). This reveals that oxygen of is the zone by which the adsorption of Ala takes place (Khaled, 2010). The nitrogen will not be used for the adsorption perhaps because of electrostatic repulsion between amino acid-based NH_3^+ and with Al^{3+}.

Table 28: *Fukui indices of Gly, Ala and Phe*

Inhibitor molecule	**Electrophilic (F^-)**				**Nucleophilic (F^+)**			
	Mulliken		***Hirshfeld***		***Mulliken***		***Hirshfeld***	
	Atom	Value	Atom	Value	Atom	Value	Atom	Value
Gly	N(5)	0.353	N(5)	0.358	C(2)	0.248	O(4)	0.230
Ala	O(5)	0.342	O(5)	0.342	C(3)	0.231	O(5)	0.217
Phe	N(10)	0.317	N(10)	0.308	C(9)	0.109	O(11)	0.106

Molecular Dynamics of Adsorption Behaviour

Molecular dynamics was applied to investigate the adsorption behaviour of the inhibitors on aluminium surface. The construction of unit cells and optimisation were performed using Forcite plus forcefield in the Accelrys Material Studio 8.0 software. The Al was cleaved along the densely packed reflection (Al (110)) being the most stable reflection compared to the open Al (111) and Al (100) planes. Figure 61 shows the cross-sectional side views of the lowest energy adsorption configurations for monomolecular and multimolecular inhibitor amino acids on Al (110) plane. Upon comparison of the three monomolecular amino acid configurations in the adsorbed phase (Fig. 61a), it can be clearly seen that each of them can be adsorbed on the aluminium surface through the nitrogen atoms. However, the multi-molecular adsorption of Gly and Ala takes place through O atom while for Phe, huge clusters of C atoms appear to compete with the oxygen for the active sites (Fig. 61b).

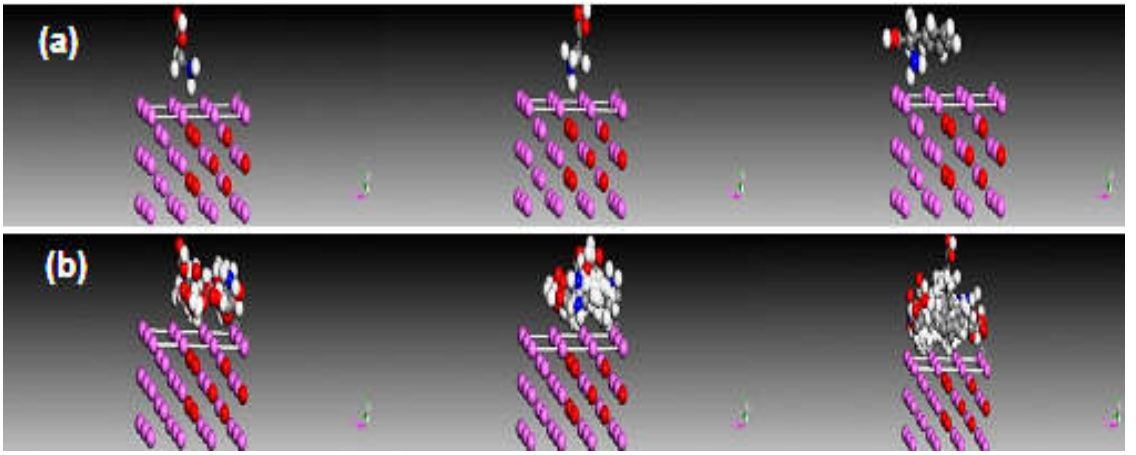

Fig. 61. The final side snapshots of adsorbed Gly Ala and Phe molecules, from left to right respectively, on aluminium (110) reflection. (a) Single molecules. (b) Many molecules. Colour scheme: White = H, blue = N, red = oxygen, grey = carbon. The interaction between the amino acids and the aluminium surface was estimated based on the theoretical adsorption energy, E_{ads}, which was calculated using Eq. (57).

$$E_{ads} = E_{total} - (E_{inhibitor} + E_{Al\ surface}) \quad (57)$$

Where $E_{inhibitor}$, $E_{Al\ surface}$ and E_{total} correspond to the total energies of the inhibitor molecule, Al (110) plane and the adsorbed molecule coupled with gas phase Al (110), respectively. In this study, the metal surface energy was zeroed. Parameters calculated such as kinetic energy, potential energy, the energy of the inhibitor molecule and energy of Al (110) surface and binding energy, are presented in Table 29.

Table 29: *Values of adsorption parameters for the interaction of Gly, Ala and Phe with the Al (110) surface using Forcite quench dynamics*

Property (kcal/mol)	Gly	Ala	Phe
Total kinetic energy	10.43282176	13.56266829	23.99549006
Total potential energy	11.77826517	-0.37687297	-14.28589205
Energy of molecule	25.40314257	18.22309314	22.66580814
Energy of Al(110) surface	0.00000000	0.00000000	0.00000000
Binding energy	-13.62487740	-18.59996611	-36.95170019

The high negative binding energies of the α-amino acids accounts for their good performance as inhibitors (Kr. Saha et al., 2015). Even though Phe has the highest binding energy (-36.95170019 kcal/mol) and expectedly more stability, lower corrosion rate was obtained with this compound compared due to the possibility of steric hindrance of the adsorption zones by the toluoyl side chain of the Phe (Soltani et al., 2012).

CONCLUSION

We now know enough to conclude that catalysis is a game-changer in our daily life. In this connection, we have presented selected contributions from our published works. Undoubtedly, in our search of catalysts we have made a lot of remarkable contributions in the novel synthesis of stable 1D, 2D and 3D dimensionalities and different morphologies of catalysts, and doped alternatives for various technological applications of societal and industrial significance. Quantum-based explanation for electron injection in this dye-sensitised nano-TiO_2 hybrids has been provided. We have made important contributions to the chemistry of photocatalytic reactions in the areas of kinetics and reaction mechanism of catalytic and non-catalytic processes. The possibility of pseudo zero-order decay models at saturated photocatalytic regimes has been successfully asserted. Catalyst for faster degradation of benzoquinone has been for the first time suggested. Evidences for ortho-para directing effects and mechanisms in photoreactions have been established. New active nanoporous activated carbon adsorbents from facile preparation routes have been disclosed. Consistence of thermodynamics of corrosion inhibition by alanine and phenylalanine with characteristics of liquid-solid reactions has been for the first time established. While it is now time I get packed up, it is no time to conclude our search. Expect more of our on-going works to continue to stream online.

ACKNOWLEDGEMENTS

It wasn't at all my dream to be at this stage, at this particular time. So, here we are, together, celebrating the law of destiny laid by the Creator of mankind, praise and thanks to Him. Let me thank the entire staff of Bayero University through the Vice Chancellor, Prof. Sagir Muhammad Abbas, for everything facilitated or provided during the course of my career. I pray for increased strength within the body. My late parents, His Royal Highness the Emir of Gaya Alhaji (Dr) Ibrahim Abdulkadir Gaya, and Hajiya Fatima Ibrahim, cannot be praised enough for their unrivalled love and care during the stages of my growth. Let me next express gratitude to my wife Ummi Nasiru Dori; siblings (Amina, Balaraba, Hadiza, Fatima, Hafsatu, Abubakar, HRH Alhaji Dr Aliyu Ibrahim Gaya, the new Emir of Gaya, and Wamban Gaya Mansur, Bashir Ai and the rest of them) and their spouses; my children (Nasiru, Ibrahim, Fatima, Aliyu, Faruk, Maryam, Abdulrahman and Halima) and other relatives for the beautiful the role they played in making my life a success.

I express my gratitude to the HOD of the Department of Pure and Industrial Chemistry, Dr Ibrahim Tajo Siraj, and our rich membership of staff including Prof. M.A. Kurawa (YUMSUK VC), Prof. M.B. Ibrahim, Prof. H.N. Aliyu, Prof. O.A. Adoum, late Prof. Abdulsalam Salisu, late Prof. W.L.O. Jimoh, Prof. Umar Sani, Prof Kabir Abdu, Dr A.A. Muhammad, Prof. Haruna Musa, Dr A.A. Yakasai, Dr M.M. Idris, Prof. S.Y. Mudi, Prof. J. Naaliya. I am thankful to other members of the College of Natural and Pharmaceutical Sciences such as Prof. S.M. Gumel (the Deputy Vice Chancellor Academics), Prof. Bashir Ali, Dr Abbas J. Badakaya, Dr Nafiu Hussain, Prof Yahaya I. Yola, Prof. A.O. Musa, Prof. Sani Ibrahim, Prof. Ibrahim Lawal, Prof. N.T. Dabo, Prof. T.H. Darma, Dr. Audu Yunusa, Dr Abdulkadir Gidado, Prof. Zainab Tukur, Prof. M.D. Mukhtar, Dr Tijjani Imam and Dr. Basheer Chedi.

I gratefully acknowledge the immeasurable contribution of my B.Sc., M.Sc. and Ph.D. project supervisors namely Prof. Naomi P. Ndahi of University of Maiduguri, Prof. A.A. Audu of Bayero University and Associate Prof. Dr. Abdul Halim Abdullah of Universiti Putra Malaysia, respectively. I appreciate all my students who have worked harmoniously together as a team and that has bred part of the stuff for this presentation: Abubakar Hamisu (a staff of KUST), Muktar Musa Ibrahim (ABU), Hamza Rabiu Sani (FUDMA), Yusuf Ibrahim (SLU), Saadatu U. Abdul-Aziz (BUK),

Ahmed Usman, Stella Amalachukwu, Sharifat Alimi, Abubakar Usman Katsina (BUK) and Buhari Shehu Ahmad.

I am indebted to former Bayero University Vice Chancellors including Prof. A.A. Rasheed, Prof. M.Y. Bello, Prof. M.A. Jega, and members of University Journals Coordinating Committee I worked with, Prof. Yusuf Adamu, Prof. Salisu Kazaure, Prof. B.S. Aliyu and Malam Sherif Ahmed. Special thanks to my former colleagues at the Directorate of Research, Innovation and Partnership especially Prof. Abdullahi Sule-Kano who's now the Deputy Vice Chancellor (Research), Prof. I.A. Rufa'i and Prof. R.S. Shatsari. Heaps of thanks accordingly to Prof. M.S. Shuaib, Prof. Mohammed Ajiya, Prof. Abdussamad Jibiya and Prof. Nura Magaji from the Faculty of Engineering, and Prof. Sani Alhassan, Dr Baba Maiyaki Musa, Prof Ibrahim Yakasai, Prof. Zubairu Iliyasu, the Deputy Vice Chancellor (Management Services) Prof. Mahmoud Babura, the Registrar, Malam Jamilu Salim and so many others I may not be able to list from the University.

Many thanks to Prof. B.Y. Jibril who hosted my post-doctoral fellowship at Sultan Qaboos University, Prof A. Uzairu, Prof Sani Sallau, Prof. M.K. Yakubu, Dr Diyauddeen Hassan, and Dr Sani Uba, all staff of Ahmadu Bello University Zaria. I am grateful to Prof. L.S. Taura, the Vice Chancellor of Sule Lamido University, President Muhammadu Buhari, GCFR, who is the Chairman of the National Agency for Science and Engineering Infrastructure (NASENI), Prof. M.S. Haruna the NASENI Executive Vice Chairman, Prof. Danshehu Bagudu, the Coordinating Director of Engineering Infrastructure at NASENI, and to Dr M.S. Dagari of Federal University, Gashua. Without having to mention names, I am grateful to all my friends and in-laws for their continued support and advice. Lastly, I wish to commend the Inaugural Lecture Committee of Prof. Esther Oyeyi and the Bayero University Press under Prof. Habu Mohammed, both of which I served as a member earlier, for their gratifying contribution to the presenters, the audience, readers and the University community at large.

REFERENCES

Abdollahi, Y., Abdullah, A. H., Gaya, U. I., Ahmadzadeh, S., Zakaria, A., Shameli, K., et al. (2012). Photocatalytic degradation of 1,4-benzoquinone in aqueous ZnO dispersions. *Journal of the Brazilian Chemical Society*, 23(2): 236-240.

Abdollahi, Y., Abdullah, Gaya U. I., Zainal Z., & Yusof. N. A. (2011), Enhanced photodegradation of o-cresol in aqueous Mn(1 %)-doped ZnO suspensions. *Environmental Technology*, *33*:1183–1189

Abubakar, A., & Gaya, U.I. (2019). Box-Behnken-optimized Cu(I) photo-Fenton-like degradation of Basic Violet 3, *Journal of Materials Environmental Sciences, **10**(1)*: 15-21.

Acharya, J., Sahub, J. N., Mohanty, C. R., & Meikap, B. C. (2009). Removal of lead(II) from wastewater by activated carbon developed from Tamarind wood by zinc chloride activation. *Chemical Engineering Journal*. *149*(1-3): 249–262.

Ahmad, A. L., Mat Yasin, N. H., Derek, C. J. C., & Lim, J. K. (2014). Kinetic studies and thermodynamics of oil extraction and transesterification of Chlorella sp. for biodiesel production. *Environmental Technology*, *35*(7): 881-7.

Ahmadian-Fard-Fini, S., Ghanbari, D., Amiri, O., & Salavati-Niasari, M. (2020). Electrospinning of electro-spinning of cellulose acetate nanofibers/Fe/carbon dot as photoluminescence sensor for mercury (II) and lead (II) ions. *Carbohydrate Polymers*, *229*(1): 115428.

Antonelli, D. M., Ying, J. Y. (1995). Synthesis of hexagonally packed mesoporous TiO_2 by a modified sol–gel method. *Angewandte Chemie, International Edition, England, 34*(18): 2014-2017.

Arfanis, M. K., Adamou, P., Moustakas, N. G., Triantis, T. M., Kontos, A. G., & Falaras, P. (2017). Photocatalytic degradation of salicylic acid and caffeine emerging contaminants using titania nanotubes. *Chemical Engineering Journal 310*(2): 525-536.

Asahi, R., Morikawa, T., Ohwaki, T., Aoki, K., & Taga, Y. (2001). Visible light photocatalysis in nitrogen-doped titanium oxides. *Science*, *293*: 269–271.

Asiltürk, M., Sayýlkan, F., & Arpaç, E. (2009). Effect of Fe^{3+} ion doping to TiO_2 on the photocatalytic degradation of Malachite Green dye under UV and Vis-irradiation, *Journal of Photochemistry and Photobiology, A: Chemistry*, *203*(1): 64–71.

Astria, D. F., Ilvania, C. V., Fraderico, A. L., Heiddy, M. A., & Vitor, H. M. (2011). Thermodynamic analysis of the kinetics reaction of the production of FAME and FAEE using Novazyme-435 as catalyst. *Fuel Processing Technology*, *92*(5): 1007-11.

ASTM (2002). Method D6751-02 "*Standard specification for biodiesel fuel (B100) blend stock for distillate fuels*". Pennsylvania: ASTM International.

Ay, F., Catalkaya, E. C., & Kargi, F. A statistical experiment design approach for advanced oxidation of Direct Red azo-dye by photo-Fenton treatment. *Journal of Hazardous Materials.* 162: 230–236.

Bagheri, A., Halakouie, H., Ghanbari, D., Mousayi, M., & Asiabani, N. (2019). Strontium hexa-ferrites and polyaniline nanocomposite: Studies of magnetization, coercivity, morphology and microwave absorption. *Journal of Nanostructures*, *9*(4): 630-638.

Barndõk, H., Peláez, M., Han, C., Platten III, W.E., Campo, P., Hermosilla, D., et al. (2013). Photocatalytioc degradation of contaminants of concern with composite NF-TiO2 films under visible and solar light. *Environmental Science and Pollution Research*. *20*(6): 3582-3591.

Benitez, F.J., Beltran-Heredia, J., Acero, J.L., & Rubio, F.J. (2000). Contribution of free radicals to chlorophenols decomposition by several advanced oxidation processes. *Chemosphere*, *41*(8): 1271–1277.

Berman, P., Nizri, S., & Wiesman, Z. (2011). Castor oil biodiesel and its blends as alternative fuel. *Biomass & Bioenergy*, *35*(7): 2861-6.

Bessekhouard, Y., Robert, D., & Weber, J.V. (2004). Bi_2S_3/TiO_2 and CdS/TiO_2 heterojunctions as an available configuration for photocatalytically degradation of organic pollutant. *Journal of Photochemistry and Photobiology, A: Chemistry, 163*(3): 569-580.

Bhaduri, S., & Mukesh, D. (2000). *Homogeneous catalysis: Mechanisms and industrial applications*. New York: Wiley Interscience.

Cano-Casanova, L., Amorós-Pérez, A., Ouzzine, M., Lillo-Ródenas, M. A., Román-Martínez, M. C. (2018). One step hydrothermal synthesis of TiO_2 with variable HCl concentration: Detailed characterization and photocatalytic activity in propene oxidation. *Applied catalysis, B Environmental*, 220: 645-653.

Capdevila-Cortada, M. (2019). Electrifying the Haber-Bosch, *Nat. Catal. 2*, 1055.

Carcel, R.A., Andronic, L., & Duta, A. (2012). Photocatalytic activity and stability of TiO_2 and WO_3 thin films. *Materials Characterization*, 40: 68-73.

Carp, O., Huisman, C. L., & Reller, A. (2004). Photoinduced reactivity of Titanium dioxide. *Progress in Solid State Chemistry*, *32*(1-2): 33-177.

Chiron, S., Minero, C., & Evione, D. (2007). Occurrence of 2,4-dichlorophenol and of 2,4-dichloro-6-nitrophenol in the Rhône River Delta (Southern France). *Environmental Science and Technology*, *41*(9): 3127-3133.

Chakrabarti, S., & Dutta, B. K. (2004). Photocatalytic degradation of model textile dyes in wastewater using ZnO as semiconductor catalyst. *Journal of Hazardous Materials B*, 112: 269–278.

Coates, J. (2000). Interpretation of Infrared Spectra. A Practical Approach. In R.A. Meyers Ed.: *Encyclopedia of Analytical Chemistry*. New York: Wiley & Sons Ltd, 2000.

Cui, S., Wei, P., & Li, L. (2019). Thermal decomposition behavior of poly (propylene carbonate) in poly (propylene carbonate)/poly (vinyl alcohol) blend. *Journal of Thermal Analysis and Calorimetry*, *135*: 2437-2446.

Czaplicka, M. (2006). Photo-degradation of chlorophenols in the aqueous solution. *Journal of Hazardous Materials B*, *134*(1-3): 45–59.

Das, S., & Khushalani, D. (2010). Nonhydrolytic route for synthesis of ZnO and its use as a recyclable photocatalyst. *Journal of Physical Chemistry C*, *114*(6): 2544–50.

Dehdab, M., Shahraki, M., & Habibi□ Khorassani, S. M. (2015). Theoretical study of inhibition efficiencies of some amino acids on corrosion of carbon steel in acidic media: green corrosion inhibitors. *Amino Acids*, *48*(1) 291-306.

Dandekar, A. Baker, R. T. K., & Vannice, M. A. (1998). Characterization of activated carbon, graphitized carbon fibers and synthetic diamond powder using TPD and DRIFTS. *Carbon*, *36*(12): 1821–1831.

Dette, C., Pérez-Osorio, M. A., Kley, C. S., Punke, P., Patrick, C. E., Jacobson, P., et al. (2014). TiO_2 anatase with a bandgap in the visible region. *Nano Letters, 14*(11): 6533-6538.

Doong, R., Chen, C.-H., Maithreepala, R. A. & Chang, S. M. (2001). The influence of pH and cadmium sulphide on the photocatalytic degradation of 2-chlorophenol in titanium dioxide suspensions. *Water Research*, *35*(12): 2873–2880.

Etacheri, V., Roshan R., & Kumar V. (2012). Mg-doped ZnO nanoparticles for efficient sunlight-driven photocatalysis. *ACS Applied Materials & Interfaces*, *4*(5): 2717-25.

Fan, H.-J., Huang, S.-T., Chung, W.-H., & Jan, J.-L. (2009). Degradation pathways of crystal violet by Fenton and Fenton-like systems: condition optimization

an intermediate separation and identification. *Journal of Hazardous Materials*, *171*(1-3): 1032–1044.

Fletcher, S. (2021, March 23). *Catalysis*. https://www.chem.ox.ac.uk/catalysis.aspx

Engel T, Reid P. (2006). *Physical chemistry*. San Fransisco: Pearson Education.

Evonic (2018). The Modern Chemist's Guide to Hydrogen Peroxide and Peracetic Acid, C&En e-books, American Chemical Society.

Fiorentino, A., Cucciniello, R., Di Cesare, A., Fonaneto, D., Prete, P., Rizzo, L., et al. (2018). Disinfection of urban wastewater by a new photo-Fenton like process using Cu-iminodisuccinic acid complex as catalyst at neutral pH. *Water Research*, 146: 206-215.

Fragoza-Mar, L., Olivares-Xometl, O., Domínguez-Aguilar, M. A., Flores, E. A., Arellanes-Lozada, P., & Jiménez-Cruz, F. (2012). Corrosion inhibitor activity of 1,3-diketone malonates for mild steel in aqueous hydrochloric acid solution. *Corrosion Science*, *61*: 171-184.

Gao, J., Liu, L., Liu, X., Zhou, H., Huang, S., & Wang, Z. (2008). Levels and spatial distribution of chlorophenols – 2,4-Dichlorophenol, 2,4,6-trichlorophenol, and pentachlorophenol in surface water of China. *Chemosphere*, *71*(6): 1181–1187

Gaya, U. I. (2011). Comparative analysis of ZnO-catalyzed photo-oxidation of *p*-chlorophenols. *European Journal of Chemistry*, *2*(2): 163-167.

Gaya, U. I. (2021). Recent approaches, catalysts and formulations for enhanced recovery of heavy crude oils. *Periodica Polytechnica Chemical Engineering* (Accepted manuscript).

Gaya, U. I., & Abdullah A. H. (2008). Heterogeneous photocatalytic degradation of organic contaminants over titanium dioxide: a review of fundamentals, progress and problems. *Journal of Photochemistry and Photobiology, C*, 9: 1-12.

Gaya, U. I., Abdullah, A. H., Zainal, Z., & Hussein, M. Z. (2009). Photocatalytic treatment of 4-chlorophenol in aqueous ZnO suspensions: Intermediates, influence of dosage and inorganic anions. *Journal of Hazardous Materials*, *168*: 57-63.

Gaya, U. I., Abdullah, A. H., Zainal, Z., & Hussein, M. Z. (2010a). Photocatalytic degradation of 2,4-dichlorophenol in irradiated aqueous ZnO suspension. *International Journal of Chemistry*, *2*(1): 180-193.

Gaya, U. I., Abdullah, A. H., Hussein, M. Z., Zainal, Z. (2010b). Photocatalytic removal of 2,4,6-trichlorophenol from water exploiting commercial ZnO powder. Desalination. 263: 172-182.

Gaya, U. I., Abubakar, U. K., A. U., & Buhari, S. A. (2013). Adsorption of

water-borne Pb^{2+} over chemically-treated leaves of *Tridax Procumbens*. *Nigerian Journal of Science and Environment*, *12*(1): 93-97.

Gaya, U. I., & Ikechukwu, S. A. (2016). Heavy metal contamination of selected spices obtained from Nigeria. *Journal of Applied Sciences and Environmental Management, 20*(3): 681-688.

Gaya, U. I.**,** Jibril, B. Y., Al-Wehaibi, Y. M., Al-Hajri, R. S., & Naser, J. T. (2012). Ring opening of decalin over zeolite-supported Ni-Co-Mo catalysts. *International Proceedings of Chemical, Biological, Environmental Engineering*, 49: 139-143.

Gaya, U. I., Otene, E., & Abdullahi, A. H. (2015). Adsorption of aqueous Cd(II) and Pb(II) on activated carbon nanopores prepared by chemical activation of doum palm shell. *SpringerPlus*, 4: 458.

Godlewska, E. Z., Przystas, W., & Sota, E. G. (2014). Decolorization of different dyes by two Pseudomonas strains under various growth conditions. *Water Air Soil Pollution*, *225*(2): 1-13.

Haas, A., Rabl, S., Ferrari, M., Calemma, V., & Weitkamp. J. (2012). Ring opening of decalin via hydrogenolysis on Ir/- and Pt/silica catalysts. *Applied Catalysis, A: Gen.*, *425– 426*: 97– 109.

Hagen, J. (2015). *Industrial catalysis: A practical approach* (3rd ed. 2015). Weinheim: Wiley-VCH.

Hamisu, A., Gaya, U.I., & Abdullah, A. H. (2020a) Effect of Alkali Strength on the Hydrothermal Growth of Photoactive TiO_2 Nanowires. *Journal of Nanostructures*, *10*(3): 639-651.

Hamisu, A., Gaya, U.I., & Abdullah, A. H. (2020b). A novel poly(vinyl alcohol) post-precipitation template synthesis and property tuning of photoactive mesoporous nano-TiO_2. *Physical Chemistry Research*, *8*(2): 281-295.

Hamisu, A., Gaya, U. I., & Abdullah, A. H. (2021). Bi-template assisted sol-gel synthesis of photocatalytically-active mesoporous anatase TiO_2 nanoparticles. *Applied Science and Engineering Progress* (Accepted article).

Hanaor, D. A. H., Sorrel, C. C. (2011). Review of the anatase to rutile phase transformation. *J. Materi*als Science *46*: 855-874.

Hassani, A., Karaca, C., Karaca, S., Khataee, A., Açışl, O., & Yılmaz, B. (2018). *Ultrasonics Sonochemistry,* 42: 390-402.

Hayashi, H., Torii, K. (2002). Hydrothermal synthesis of titania photocatalyst under subcritical and supercritical water conditions. *Journal of Materials Chemistry, 12*: 3671-3676.

Hoekman, S. K., Broch, A., Robbins, C., Ceniceros, E., & Natarajan, M. (2012).

Review of biodiesel composition, properties, and specifications. *Renewable and Sustainable Energy Reviews*, *16*(1): 143– 69.

Hoffmann, M.R., Martin, S. T., Choi, W., & Bahnemann, D. W. (1995) Environmental applications of semiconductor photocatalysis. *Chemical Reviews*, *95*(1): 69–96.

Ibrahim, M. M., & Gaya, U. I. (2019). Synthesis of Eosin Y-Sensitized Ag-TiO_2 nano-hybrid for optimized photocatalytic degradation of aqueous caffeine. *Journal of the Chilean Chemical Society*, 64(1), 4275-4284.

Iijima, S. (1991). Helical microtubules of graphitic carbon. *Letters to Nature*, *354*: 56-58.

Jaimy, K.B., Ghosh, S., Sankar, S., Warrier, K., An aqueous sol–gel synthesis of chromium (III) doped mesoporous titanium dioxide for visible light photocatalysis. *Materials Research Bulletin. 46*(6): 914-921.

Jayaweera, P. V. V., Perera, A. G. U., & Tennakone, K. (2008). Why Gratzel's cell works so well. *Inorganica Chimica Acta*, *361*(3): 707–711.

Kamel, M. M., Mashaly, H. M., & Abdelghaffar, F. (2013). Photocatalyst decolorization of reactive orange 5 dye using MgO nano powder and H_2O_2 solution. *World Applied Sciences Journal*, *26*(8): 1053-1060.

Kao, L.-H., Hsu, T.-C., & Lu, H.-Y. (2007). Sol-gel synthesis and morphological control of nanocrystalline TiO_2 via urea treatment. *Journal of Colloid and Interface Science*, *316*(1): 160–167.

Kesić, Ž, Lukić, I, Zdujić, L, Liu, H, & Skala, D. (2015). Mechanochemical synthesis of $CaO{\cdot}ZnO.K_2CO_3$ catalyst:Characterization and activity for methanolysis of sunflower oil. *Chemical Industry and Chemical Engineering Quarterly*, *21*(1): 1−12.

Khaled, K. F. (2010). Corrosion control of copper in nitric acid solutions using some amino acids–A combined experimental and theoretical study. *Corrosion Science*, *52*(10): 3225-3234.

Kim, H.H., Ogata, A., & Futamura, S. (2006). Application of plasma-catalyst hybrid for the control of NOx and volatile organic compounds. In: Bevy, L.P. (Ed.), *Trends in catalysis research*, United Kingdom: Nova Science Publishers Inc.

Knothe, G. (2008). "Designer" Biodiesel: Optimizing fatty ester composition to improve fuel properties. *Energy Fuels*, *22*(2): 1358–64.

Korea Herald (2018, August 13). *[Hydrogen Korea] Tale of Hyundai's hydrogen dream.* Retrieved from http://www.koreaherald.com/view.php?ud=20180813000471

Kosmulski, M. (2006) pH-dependent surface charging and points of zero charge III. Update. *Journal of Colloid and Interface Science*, *298*(1): 730–741.

Lair, A., Ferronato, C., Chovelon, J-M., & Herrmann, J-M. (2008). Naphthalene degradation in water by heterogeneous photocatalysis: An investigation of the influence of 17 inorganic anions. *Journal of Photochemistry and Photobiology, A: Chemistry, 193*(2-3): 193–203.

Lam, M. K., Lee, K. T., & Mohamed, A. R. (2010). Homogeneous, heterogeneous and enzymatic catalysis for transesterification of high free fatty acid oil (waste cooking oil) to biodiesel: A review. *Biotechnology Advances*. *28*: 500-518.

Li, X., Cubbage, J. W., Tetzlaff, T. A., & Jenks, W. S. (1999). Photocatalytic degradation of 4-chlorophenol. 1. The hydroquinone pathway. *Journal of Organic Chemistry*, *64*(23): 8509-8524.

Liu, J., Li, Y., Ke, J., Wang, S., Wang, L., Xiao, H. (2018). Black NiO-TiO_2 nanorods for solar photocatalysis: Recognition of electronic structure and reaction mechanism. *Applied Catalysis, B Environmental*, *224*: 705-714.

Liu, L., Zhang, Y., Dong, S., Zhang, B., Meng, S., Xu, J., et al. (2018). Template controlled synthesis of mesoporous TiO_2 particles for efficient photoanodes in dye sensitized solar cells. *Journal of The Electrochemical Society*, *165*(2): F1-F6.

Liu, W-J., Zeng, F-X., Jiang, H., Zhang, X-S., & Yu, H.-Q. (2011). Techno-economic evaluation of the integrated biosorption–pyrolysis technology for lead (Pb) recovery from aqueous solution. *Bioresource Technology*. *102*(10): 6260-6265.

Lyu, L., Zhang, L., & Hu, C. (2015). Enhanced Fenton-like degradation of pharmaceuticals over framework copper species in copper-doped mesoporous silica microspheres. *Chemical Engineering Journal*, 274: 298–306.

Mao-Xiang, J., Xue-Qin, J., Wang-Xing, L., Dong-Hong, L., & Zhou, W. (2009). Preparation and photocatalytic activity of mesoporous TiO_2 microspheres. *Micro and Nanosystems*, *1*(1): 12-16.

Marques, R. R. N., Sampaio, M. J., Carrapi, P. M., Silva, C. G., Morales, T. S., Drazic, G., et al. (2013). Photocatalytic degradation of caffeine: Developing solutions for emerging pollutants. *Catalysis Today*, *209*: 108-115.

Marto, J., Marcos, P.S, Trindade, T., Labrincha, J.A. (2009). Photocatalytic decolouration of orange ii by ZnO active layers screen-printed on ceramic tiles. *Journal of Hazardous Materials*, *163*(1), 36-42.

Mehra T. (2018). Process optimization biodiesel production from cedar wood oil (*Cerdrus deodara*) using response surface methodology. SAE Technical paper 2018-01-0665.

Mo, S.-D., & Ching, W. Y. (1995). Electronic and optical properties of three phases of titanium dioxide: Rutile, anatase, and brookite. *Physical Review B: Condensed Matter and Materials Physics*, *51*(19): 13023-13032.

Nabiyouni, G., Ghanbari, D. (2018). Simple preparation of magnetic, antibacterial and photo-catalyst $NiFe_2O_4$@TiO_2/Pt nanocomposites. *Journal of Nanostructures*, *8*(4):408-416.

Nautiyal, P., Subramanian, K. A., & Dastidar, M. G. (2014). Kinetic and thermodynamic studies on biodiesel production from *Spirulina platensis* algae biomass using single stage extraction-transesterifcation process. *Fuel*, *135*: 228-34.

Nawi, M. A., & Sheilatina, S. S. (2012). Photocatalytic decolourisation of Reactive Red 4 dye by an immobilised TiO_2/chitosan layer by layer system. *Journal of Colloid and Interface Science*, *372*(1): 80–87.

Nguyen, D.; Wang, W.; Long, H.; Ru, H., Facile and controllable preparation of mesoporous TiO_2 using poly (ethylene glycol) as structure-directing agent and peroxotitanic acid as precursor. *Frontiers of Materials Science. 10*: 405-412.

Noor, E. A. (2009). Evaluation of the inhibitive action of some quartenary n-heterocyclic compounds on the corrosion of Al-Cu in hydrochloric acid. *Materials Chemistry and Physics*, *114*(2-3): 533-541.

Palma-Goyes, R. E., Guzmán-Duque, F. L., Peñuela, G., González, I., Nava, J. L., & Torres-Palma, R. A. (2010). Electrochemical degradation of crystal violet with BBD electrodes: effect of electrochemical parameters and identification of organic by-products. *Chemosphere*, *81*(1): 26–32.

Pavia, D. L., Lampman, G. M., Kriz, G. S., & Vivyan, J. R. (2009). *Introduction to spectroscopy*. United Kingdom: Brooks/Cole.

Perepichka, D. F., & Bryce, M.R. (2005). Molecules with exceptionally small HOMO-LUMO gaps. *Angewandte Chemie, International Edition, 44*(34), 5370-5373.

Pohanish, R. P., & Greene, S. A. (1996). *Hazardous material handbook*. New York: Van Nostrand Reinhold/ International Thompson Publishing.

Rashid, U., Anwar, F., Moser, B.R., & Knothe, G. (2008). Moringa oleifera oil: A possible source of biodiesel. *Bioresource Technology. 99*(17): 8175–9.

Rayalu, S. S., Jose, D., Joshi, M. V., Mangrulkar, P. A., Shrestha, K., & Klabunde, K. (2013). Photocatalytic water splitting on Au/TiO_2 nanocomposites synthesized through various routes: Enhancement in photocatalytic activity due to SPR effect. *Applied Catalysis, B Environmental*, *142– 143*: 684– 693.

Razani, A., Abdullah, A. H., Fitrianto, A., Yusof, N. A., & Gaya, U. I. (2017). Sol-gel synthesis of Fe_2O_3-doped TiO_2 for optimized photocatalytic degradation of 2,4-dichlorophenoxyacetic acid. *Oriental Journal of Chemistry*, *33*(4): 1959-1968.

Rosal, R., Rodríguez, A., Perdigón-Melón, J. A., Petre, A., García-Calvo, E., Gómez, M.J., et al. (2009). Degradation of caffeine and identification of the transformation products generated by ozonation. *Chemosphere 74*(6): 825-831.

Rothenberg, G. (2008). *Catalysis: Concepts and green applications*. Weinheim: WILEY-VCH Verlag GmbH & Co. KGaA.

Saha, S. Kr., Gosh, P., Hens, A., & Murmu, N. C. (2015). Density functional theory and molecular dynamics simulation study on corrosion inhibition performance of mild steel by mercapto-quinoline Schiff base corrosion inhibitor. *Physica E: Low Dimensional Systems and Nanostructures*, *66*: 332-341.

Salman, S.A., Bakr, N.A., Abduallah, S.S. (2019). Study of Thermal Decomposition and FTIR for PVA-AlCl Composite Films. *Journal of Engineering and Applied Sciences*, *14*(3): 717-724.

Sehili, T., Boule, P., & Lemaire, J. (1991). Photocatalysed transfornation of chloroaromatic derivatives on zinc oxide IV: 2,4-dichlorophenol, *Chemosphere,* 1991. *22*(11): 1053-1062.

Sehili, T., Boule, P., & Lemaire, J. (1989). Photocatalysed transformation of chloroaromatic derivatives on zinc oxide III: Chlorophenols. *Journal of Photochemistry and Photobiology, A: Chemistry, 50*(1): 117 – 127.

Serra-Clusellas, A., De Angelis, L., Lin, C.-H., Vo, P., Bayati, M., Sumner, L., et al. (2018). Abatement of 2,4-D by H_2O_2 solar photolysis and solar photo-Fenton-like process with minute Fe(III) concentrations. *Water Res.*, *144*: 572-580.

Shao, J., Sheng, W., Wang, M., Li, S., Chen, J., Zhang, Y., et al. (2017). In situ synthesis of carbon-doped TiO_2 single-crystal nanorods with a remarkably photocatalytic efficiency. *Applied Catalysis, B Environmental*, *209*: 311-314.

Shehu, N. U., & Gaya, U. I. (2019). Muhammad, A.A. Influence of Side Chain on the Inhibition of Aluminium Corrosion in HCl by α-Amino Acids. *Applied Science and Engineering Progress*, *12*(3): 186-197.

Sobczyński, A. , Duczmal, L., & Dobosz, A. (1999). Photocatalysis by illuminated titania: oxidation of hydroquinone and p-benzoquinone. *Monatshefte für Chemie*, *130*: 377. Sani, H.R., & Gaya, U.I. (2019). Methanolysis of Gmelina seed oil to biodiesel with KNO_3 activated MgO-ZnO composite catalyst. *Journal of the Turkish Chemical Society, Section A: Chemistry, 6*(3): 335-348.

Soltani, N., Tavakkoli, N., Khayatkashani, M., & Jalali. M. R. (2012). Green approach to corrosion inhibition of 304 stainless steel in hydrochloric acid solution by the extract of Salvia officinalis leaves. *Corrosion Science*, 62: 122-135.

Theurich, J., Lindner, M., & Bahnemann, D. W. (1996). Photocatalytic degradation of 4-chlorophenol in aerated aqueous titanium dioxide suspensions: A kinetic and mechanistic study. *Langmuir*, *12*(26): 6368-6376.

Trikalitis, P. N., Rangan, K. K., Bakas, T, & Kanatzidis, M. G. (2001). Varied pore organization in mesostructured semiconductor based on the $[SnSe_4]^{4-}$ anion. *Nature*. *410*: 671-674.

Umar, S. A., & Gaya, U. I. (2019). Optimised Photocatalytic Degradation of Crystal Violet Over 1wt% MgO-ZnO Composite Catalyst. *Journal of Science and Technology*, *11*(1): 25-33.

Wang, P., Guan, Z., Li, Q., & Yang, J. (2017). Efficient visible-light-driven photocatalytic hydrogen production from water by using Eosin Y-sensitized novel g-C_3N_4/Pt/GO composites. *Journal of Materials Science*, *53*, 774-786.

Wang, Q., Fan, H., Wu, S., Zhang, Z., Zhang, P., & Han, B. (2012). Water as an additive to enhance the ring opening of naphthalene. *Green Chemistry*, *14*(4) 1152-1158.

Xiao, J., Peng, T., Li, R., Peng, Z., & Yan, C. (2006). Preparation, phase transformation and photocatalytic activities of cerium-doped mesoporous titania nanoparticles. *Journal of Solid State Chemistry. 179*(4): 1161-1170.

Yalçın, Y.; Kılıç, M.; Çınar, Z. (2010). Fe^{+3}-doped TiO_2: A combined experimental and computational approach to the evaluation of visible light activity. *Applied Catalysis, B Environmental*, 2010, *99*(3-4): 469-477.

Yandrasits, M., & Hamrock, S. (2012). Polymers for a sustainable environment and green energy. In Krzysztof Matyjaszewski and M. Möller (Ed.) *Polymer Science: A Comprehensive Reference*, Amsterdam: Elsevier BV.

Yang, J., Du, J., Li, X., Liu, Y., Jiang, C., Qi, W., et al. (2019). Highly hydrophilic TiO_2 nanotubes network by alkaline hydrothermal method for photocatalysis degradation of methyl orange. *Nanomaterials*, *9*(4): 526.

Yu, J., Zhang, L., Cheng, B., Su, Y. (2007). Hydrothermal preparation and photocatalytic activity of hierarchically sponge-like macro-/mesoporous titania. *Journal of Physical Chemistry, C*, *111*(28): 10582-10589.

Yu, J., & Yu, X. (2008). Hydrothermal synthesis and photocatalytic activity of zinc oxide hollow spheres. *Environmental Science and Technology*, *42*(13): 4902-4907.

Yusuf, A., & Gaya, U. (2018). Mechanochemical synthesis and characterization of N-doped TiO_2 for photocatalytic degradation of caffeine. *Nanochemisty Research*, *3*(1): 29-35, 2018.

Zahoor, M., Arshad, A., Khan, Y., Iqbal, M., Bajwa, S. Z., Soomro, R. A., et al. (2018). Enhanced photocatalytic performance of CeO_2–TiO_2 nanocomposite for degradation of crystal violet dye and industrial waste effluent. *Applied Nanoscience*, 8: 1091-1099.

Zhang, H., Chen, G., & Bahnemann, D. W. (2009). Photoelectrocatalytic materials for environmental applications. *Journal of Materials Chemistry*, *19*(29): 5089–5121.

Zhang, Y., Han, C., Zhang, G., Dionysiou, D. D., & Nadagouda, M. N. (2015). PEG-assisted synthesis of crystal TiO_2 nanowires with high specific surface area for enhanced photocatalytic degradation of atrazine. *Chemical Engineering Journal*, *268*: 170-179.

Zhang, L., Kanki, T., Sano, N., & Toyoda, A. (2006). Pathway and kinetics on photocatalytic destruction of aqueous phenol. *Environmental Monitoring and Assessment, 115*(1-3): 395–403.

Zhang, Y. & Q. Li (2013). Synthesis and characterisation of Fe-doped TiO_2 films by electrophoretic method and its photocatalytic activity towards methyl orange. *Solid State Sciences*, *16*: 16-20.

Zhao, Q., Tang, T., Dang, P., Zhang, Z., & Wang. F. (2017). The corrosion inhibition effect of triazinedithiol inhibitors for aluminium alloy in a 1M HCl solution. *Metals*, *7*(2): 1-11.

Zheng, Y., Zheng, L., Zhan, Y., Lin, X., Zheng, Q., & Wei, K. (2007). Ag/ZnO Heterostructure nanocrystals: synthesis, characterization, and photocatalysis. *Inorganic Chemistry*, *46*(17): 6980-6986.

Zulfiqar, M., Chowdhury, S., & Omar, A. (2018). Hydrothermal synthesis of multiwalled TiO_2 nanotubes and its photocatalytic activities for Orange II removal. Separation Science and Technology, *53*(9): 1412-1422.

LIST OF PROFESSORIAL INAUGURAL LECTURE TO DATE

S/N	NAME	DEPT	DATE	TOPIC
1st	Emmanuel Ajayi Olofin	Geography	4th March, 1992	The Gains and Pains of Putting a Water Lock on the Face of the Drylands of Nigeria
2nd	Garba Dahuwa Azare	Education	24th June, 2000	BASIC CONCERNS: Revitalizing Nigeria's Primary Education in the New Millennium
3rd	Dajuma Abubakar Maiwada	Education	29th July, 2000	Improving Teaching and Learning in University Education with Particular Reference to Bayero University, Kano
4th	Majekodunmi Oladeji Fatope	Chemistry	7th July, 2001	NATURAL PRODUCTS SCIENCE: Looking Back and Looking Forward
5th	Muazu Alhaji Zaria Sani	Nigerian Languages	13th October, 2001	A focus on Some Segmental and Suprasegmental Features in Hausa Phonology
6th	Isa Hashim	Political Sciences	20th March, 2004	Planning and Budget Implementation in the Health Sector
7th	Abdulla Uba Adamu	Education	24th April, 2004	SUNSET AT DAWN, DARKNESS AT NOON: Reconstructing the Mechanisms of Literacy in indigenous Communities
8th	Auwalu Hamisu Yadudu	Private and Commercial Law	5th June, 2004	LAW AS INTERPRETATION: An Exploratory inquiry from Islamic Law Jurisprudence

9th	Mohammed Sanni Abdulkadir	History	31st July, 2004	STRUCTURING, STRUGGLING AND SURVIVING ECONOMIC DEPRESSION IN NORTHERN NIGERIA: The 1930s As Preview of the present
10th	Muhammad Sani Sule	Bio-chemistry	23rd March, 2013	Enzymology and Radiation Biology in the Understanding of Biochemistry
11th	Essiet Unanaowo Essiet	Agriculture	22nd May, 2013	AGRICULTURE SUSTAINABILITY IN THE DRYLAND OF NIGERIA: Realities and Prospects
12th	Aliyu Kamal	English Studies	5th March, 2014	The Islamic Novel Style and Structure
13th	Abdu Ahmed Manga	Agriculture	9th April, 2014	Horticulture as a Panacea for Food Insecurity and Unemployment
14th	Sa'idu Muhammad Gusau	Nigerian Languages	26th May, 2014	Wakar Baka Bahaushiya (The Hausa Oral Songs)
15th	Abdallah Uba Adamu	Mass Comm-unication	9th July, 2014	IMPERIALISM FROM BELOW: Media Contra-Flows and Emergence of Metro-Sexual Hausa Visual Culture
16th	Ghaji Abubakar Badawi	Library and Information Sciences	29th July, 2015	THE ROLE OF PUBLIC LIBRARIES AS CENTERS OF INFORMATION TO DISADVANTAGED GROUPS: A 2004 - 2014 Study of the Information Needs of Gada Prostitutes in Dawakin Kudu Local Government Area of Kano State, Nigeria.

17th	Mohammed Kabir	Community Medicine	16th September, 2015	Public Health Concern for Chronic Non-Communicable Diseases Surpasses Anxiety Over Most Infections
18th	T.I. Oyeyi	Biological Sciences	30th March 2017	Linking Schistosomiasis and Water Resources Development in Kano State Nigeria: Public Health Impact and Mitigation
19th	Abdulrazaq G. Habib	Medicine	27th April, 2017	Medicine, Science and Society – The Global Health Imperative
20th	S. Y. Mudi	Chemistry	6th July, 2017	Natural Products: Plants as Potential Sources of Drugs
21st	Sani Ibrahim	Biological Sciences	27th July, 2017	BETWEEN LIFE AND DEATH: Water Quality and Resource Evaluation - The Place of Hydrobiologists
22nd	J. Afolabi Falola	Geography	26th October, 2017	The Poor We Have With Us Always
23rd	Umar G. Danbatta	Electrical Engineering	2nd November, 2017	GETTING OUT OF THE WOODS: Diversifying Nigeria's Economy Through the Telecommunications Sector
24th	Adelani W. Tijani	Nursing	23rd November, 2017	Wholesome Alimentation: Path to Radiant Health
25th	Juwayriya Badamasiuy	Private and Commercial Law	21st December, 2017	Uncovering Patriarchy in the Law: Feminist Movement for Re-Interpretation of Islamic Law in Focus.

26th	Isa Mukhtar	Nigerian Language	25th January, 2018	STYLISTIC THEORIES AND THE LINGUISTICS OF HAUSA PROSE TEXTS: the (SFL) approach.
27th	Ganiyu Sokunbi	Physiotherapy	29th March, 2018	TODAY IT HURTS, TOMORROW IT WORKS: Complimentary and Alternative Therapy for Failed Back Syndrome
28th	Aminu K. Kurfi	Business Admin. and Entrepreneurship	19th April, 2018	Micro-finance as an Elixir for Poverty Alleviation and Wealth Creation in Nigeria
29th	Muhammad S. Khamisu	Arabic	17th May, 2018	Substitution in Arabic Languages Rules and Types
30th	Habu Nuhu Aliyu	Pure and Industrial Chemistry	21st June, 2018	SCHIFF BASES AND THEIR TRANSITION METAL COMPLEXES: The Drug for the Next Generation
31st	Hashim M. Alhassan	Civil Engineering	19th July, 2018	EASING THE BURDEN OF TRAVEL: Can Roadway Capacity Modeling Help?
32nd	Habu Mohammed	Political Science	13th September, 2018	TUG OF WAR OR ECHO IN THE DARK? Civil Society Organizations (CSOs) and the Fight Against Corruption in the Era of Change Mantra in Nigeria
33rd	Bello Idrith Tijjani	Physics	20th September, 2018	NAVIGATING THE DATA LABYRINTH: Application of Some Advanced Statistical Analysis in Atmospheric Physics
34th	Mohammed Ajiya	Electrical Engineering	18th October, 2018	SEAMLESS GLOBAL CONNECTIVITY AT THE SPEED OF LIGHT: Converting Intrinsic Phenomena in Optical Fibers to Capacity Increase.
35th	Abdulrahman Abdul Audu	Pure and Industrial Chemistry	25th October, 2018	MY ACADEMIC VOYAGE IN WATER INTO THE WORLD OF HEAVY METALS
36th	Ibrahim Rakson	Animal Science	21st February,	FORAGE AND FODDER PRODUCTION IN NIGERIA: Its

	Muhammad		2019	Sensitivity in Sustainable Ranching.
37th	Muhammad Bashir Ibrahim	Department of Pure and Industrial Chemistry	14th March, 2019	WATER POLLUTION AND THE QUEST FOR ITS REMEDIATION: The Natural Resource Option
38th	Oyerinde O. Oyesegun	Department of Physical and Health Education,	4th April, 2019	MAN DOES NOT DIE BUT KILLS HIMSELF: The Dilemma of the Health Educator and the Moderating Influence of Health Education
39th	Danladi Ibrahim Musa	Department of Physical and Health Education	25th April, 2019	WAGING WAR ON THE DEADLY QUARTET AND ITS CO-MORBIDITIES: A Physical Activity Panacea
40th	Kabiru Isa Dandago	Department of Accounting	2nd May, 2019	THE ACCOUNTING IN HUMANITY KNOWS NO BOUNDS
41st	Mustapha Hassan Bichi	Department of Civil Engineering	20th June, 2019	MAN, ENVIRONMENT AND WATER - The *Moringa oleifera (Zogale)* Intervention
42nd	Mustapha Muktar	*Department of Economics*	27th June, 2019	PEOPLE, PLANET AND PROFIT: Peaceful Bed Fellows at the Best of Times But Strange Roommates at Present - The Economist's Approach to a Peaceful and Sustainable Co-Existence
43rd	Mohammed Atiku Kano	*Department of Biochemistry*	25th July, 2019	Serum Lipids and Lipoproteins - A Curse or a Blessing?
44th	Rabi'u Mohammed	*Department of Physical and Health Education*	8th July, 2019	EXERCISE AND SPORTS FOR THE ATYPICAL PERSONS: A Multidimensional Analysis

45th	Yahaya, D.B.	Department of Mechanical Engineering	12th December 2019	GETTING OUT OF THE DARKNESS: The Solar Energy Solution
46th	Shehu Alhaji Musa	*Department of Agricultural Economics & Extension*	22nd April 2021	CROSSING THE CHASMS OF AGRICULTURAL DEVELOPMENT IN NIGERIA: Consumer Preference Studies: Market Integration Syntheses and Value Chain Diagnoses to the Rescue
47th	Shehu U.R. Aliyu	*Department of Economics*	24th June, 2021	What Have We Learnt From Modelling Stock Returns In Nigeria: Higgledy-Piggledy?
48th	Kamilu Sani Fage	*Department of Political Science*	8th July, 2021	FROM DIVIDEND'S OPTIMISM TO DASHED HOPES: The Imperatives of Leadership Re-Engineering in Nigeria
49th	Babatunde Olamide BAMGBOSE	*Department of Oral Diagnostic Sciences*	9th Sept., 2021	MATRIX OF THE KNOWLEDGE OF LIGHT AND KNIFE: The Journey of a Maxillofacial Surgeon into Imaging